

Modelling of the near-surface wind speed: Boundary Layer and Climate aspects

Von der Fakultät für Mathematik und Naturwissenschaften der Carl von Ossietzky Universität Oldenburg zur Erlangung des Grades und
Titels eines

Doktors der Naturwissenschaften (Dr.rer.nat.)

angenommene Dissertation

von Herrn Kay Sušelj
geboren am 30.12.1977
in Ljubljana (Slowenien)

Gutachter: Prof. Dr. Joachim Peinke

Zweite Gutachterin: Prof. Dr. Ulrike Feudel

Tag der Disputation: 16.7.2009

Acknowledgements

Writing this thesis has been fascinating and extremely rewarding. Starting as a vague idea to investigate the near surface wind climate over the North Sea, it evolved into its present form. I would like to thank a number of people who have contributed to the final result in many different ways:

Firstly my supervisor and colleague at ForWind Abha Sood who helped me to get started and planned additional activities such as workshops, summer schools and conferences, which helped me to extend my knowledge of atmospheric science. She has also greatly helped me in doing the research and writing the thesis by making critical suggestions and posing challenging questions.

I am also grateful to all colleagues at ForWind for nice working atmosphere and all the work and discussions we had together during the working time as well as in free time. Special thanks to Detlev Heinemann, the leader of our research group.

I was lucky to have my PhD position sponsored by European Union Marie-Curie Programme ModObs - *Atmospheric modelling for wind energy, climate and environment applications: exploring added value from new observation technique* (MRTN-CT-2005-019369). It was a great opportunity to participate in the project. It gave me a lot of chances to widen my knowledge by supporting me to participate on the summer schools as well as it gave me opportunities to present my work at the conferences. I was also very fortunate to had chance to experience German culture.

I would also like to thank to the whole ModObs team, the students and supervisors for interesting meetings and exchanges of knowledge and experiences. Special thanks go to Anna Maria Sempreviva, the coordinator of the project.

I am also thankful to my thesis supervisor, Prof. Dr. Joachim Peinke for supporting me with the writing of the thesis and to the reviewers for investing their time to read the thesis and judge the quality of the work.

Abstract

The knowledge of the near surface wind speed is important for numerous applications including wind energy. This thesis investigates the following aspects: i) the variability of the past near surface wind climate over the North-Western Europe and specifically over the North Sea and its relation to large scale circulation patterns; ii) possible future change of the near-surface wind climate over Europe and North Atlantic; and iii) improvement of Weather Research and Forecasting (WRF) model to simulate wind conditions in the lower part of the atmospheric boundary layer.

The variability of wind speeds from different atmospheric reanalysis datasets in the past 50 years over the North-Western Europe and North Sea is studied. Wind speed patterns explaining majority of its variance were found and related to the variability of the large scale circulation patterns defined from Sea Level Pressure. Majority of wind speed variability can be described by three wind speed patterns or related circulation patterns. The wind speed and circulation patterns show coherent variability over the last decades. However, the extreme wind speeds are less well related to the circulation patterns.

With a similar method as described above, the wind speed patterns and circulation patterns explaining the significant part of the wind speed trend have been found. The possible change of the circulation patterns from the results of the simulations of 16 IPCC models under A2 greenhouse gas scenario has been investigated. From the change of time series of the circulation patterns the climate change of the wind speed in the future climate was derived. We observed significant increase of the winter wind speed over the Northern Atlantic.

One year long hindcast of the wind conditions using WRF model reveals a bias of modelled wind shear compared to the measurements at tower measurements at North Sea (FINO) and Baltic Sea (Östergarnsholm). Mellor-Jamada-Janjić (MYJ) parameterisation of the turbulence which was used as a surface and boundary layer parameterisation in WRF was identified as the most probable reason for the bias. A correction of the MYJ scheme is proposed by changing the master length scale, which serves as a closure assumption of the scheme. Among others, Prandtl mixing length scale which was used as a surface layer length scale was corrected by surface stability. Finally, it was shown that WRF with improved MYJ scheme is well suited to represent the wind shear in the lower part of the marine atmospheric boundary layer.

Zusammenfassung

Die Kenntnis der oberflächennahen Windgeschwindigkeit ist unverzichtbar für eine Vielzahl von Anwendungen, einschließlich der Windenergie. Für die vorliegende Arbeit wurden folgende Aspekte untersucht: i) die Variabilität des Windes in der Vergangenheit über Nordwest-Europa und im Speziellen über der Nordsee sowie die Beziehung der Variabilität zu großskaligen Zirkulationsmustern, ii) mögliche Änderungen des oberflächennahen Windklimas im gesamten europäischen und nordatlantischen Raum in der Zukunft, iii) die Optimierung des Weather Research and Forecasting Models (WRF) insbesondere im Hinblick auf die Simulation des Windes in der marinen unteren atmosphärischen Grenzschicht.

Beim Vergleich der Variabilität der Windgeschwindigkeiten in unterschiedlichen Reanalyse-Datensätzen für einen Zeitraum von 50 Jahren wurden Strukturen gefunden, die in Bezug gesetzt wurden zur Variabilität der raumzeitlichen Muster des Luftdruckes auf Höhe des Meeresspiegels, die ebenfalls bei den Untersuchungen für diese Arbeit entdeckt wurden. Dadurch lässt sich ein signifikanter Teil der Windgeschwindigkeitsvarianz erklären, weil sich die Wind- und die Luftdruckmuster der letzten Jahrzehnte durch eine kohärente Variabilität auszeichnen. Die Kohärenz zwischen den darüber hinaus untersuchten Extremwerten von Windgeschwindigkeit und Luftdruck ist etwas weniger deutlich ausgeprägt.

Ebenso erklären lassen sich mit den Untersuchungsergebnissen die größten Anteile der aus den Reanalysedaten hervor gehenden regionalen Trends der Windgeschwindigkeiten. Die im ersten Teil dieser Dissertation erarbeiteten Methoden wurden dann auf Ergebnisse von Ensemble-Vorhersagen angewendet, die mit 16 Klimamodellen (GCM) erstellt wurden. Die in den meisten Globalmodellen auf Basis des A2-Szenarios des IPCC übereinstimmend simulierten Luftdruck-Entwicklungen weisen zusammen mit der hier entwickelten Mustererkennung auf eine zu erwartende signifikante Zunahme der mittleren Windgeschwindigkeiten insbesondere im Winter hin.

Vergleiche eines mit WRF für das Jahr 2005 generierten Datensatzes mit Messungen von der Nord- und der Ostsee zeigten, dass die Parametrisierung der Turbulenz im WRF-Modell im Falle einer stabilen Atmosphäre eine Unterschätzung und im Falle einer instabilen Atmosphäre eine Überschätzung der Windscherung verursacht und somit unbefriedigend ist. Dieses Problem wurde angegangen durch eine erweiterte Definition der Mischungslänge, deren begrifflicher Ursprung auf Ludwig Prandtl zurückgeht und die die bestimmende Längenskala für turbulente Diffusions- und Dissipationsprozesse darstellt. Es konnte gezeigt werden, dass die neue Parametrisierung das vertikale Windprofil deutlich realitätsnäher modelliert.

1	Introduction and Motivation	9
2	Overview of the Methods	13
2.1	Introduction	13
2.2	Near surface wind climate	13
2.3	Boundary Layer Parameterisation in Atmospheric Models	21
3	Near Surface Wind Climate over North Sea	37
3.1	Introduction	37
3.2	Data Description	40
3.3	Analysis Methods and Results	42
3.4	Discussions and Conclusions	58
4	Climate change of WS over Europe and North Atlantic	65
4.1	Introduction	65
4.2	Data and methods	67
4.3	Trend of wind speed in the past climate	71
4.4	WS in the past and future climate from ECHAM5/MPI-OM model	75
4.5	Future change of the North Atlantic and European wind speed	77
4.6	Discussion and conclusions	84
5	Improving MYJ parameterization in WRF model	89
5.1	Introduction	89
5.2	Boundary and surface layer parameterization	91
5.3	Measurement Data	96
5.4	Idealized single column studies	99
5.5	Real Simulations	104
5.6	Discussion and conclusions	120
5.A	MYJ equations in WRF model	122
6	Summary and General Conclusions	129

1

Introduction and Motivation

Member states of the European Union (EU) are currently the global leaders in the development and application of renewable energy. Renewable sources of energy: wind power, solar power (thermal and photovoltaic), hydro-electric power, tidal power, geothermal energy and biomass are an essential alternative to fossil fuels. Promoting the use of renewable energy is important both for meeting the targets to combat the global climate change as well as to reduce dependency on energy imports (mainly oil and gas).

In March 2007, the European leaders signed an ambitious binding target to increase the share of the renewable energies from 5.5% in 2005 to 10% in 2010 and 20% in 2020. In 2008, the EU Commission put forward a proposal for a new directive on renewable energies (EU Directive, 2008), where the measures to fulfill the aforementioned target are defined. According to the proposal, each state will be required to increase the renewable energy production depending on its environmental and socio-economical conditions. For example, according to the proposal, Germany is expected to increase its share of renewable energies from 5.8% in 2005 to 18% in year 2020 and Slovenia from 16% (in 2005) to 25% (in 2020).

The wind energy represents an important source of the renewable energy in Northern Europe and specifically in Germany. In the last decade, the utilisation of the wind energy in Germany has been increasing almost exponentially. In summer 2008, nearly 20.000 wind turbines were installed with the total capacity of over 23.000 MW which produced around 6.7% of the total energy consumption in Germany (Ender, 2008b). Most of the wind energy capacity is installed in North German states, where the wind potential is the highest. While the onshore sites are limited and are expected to be exhausted in the next decades, the expansion of wind energy utilisation offshore (to the North Sea and Baltic Sea) is foreseen. According to projections (Ender, 2008a), the installed capacity of wind energy in North Germany is expected to reach 60.000 MW by 2030 which would result in more than 25% of the German energy consumption. The majority of the increase of the installed capacity in the next decades is expected to be due to repowering of the onshore sites (i.e. replacing the smaller wind turbines with the bigger ones) and especially from the utilisation of the offshore wind energy.

While the utilisation of the offshore wind energy is only at its start and the offshore environmental conditions are in many aspects different from the one onshore, there is a necessity for the research of the offshore environmental (especially wind) conditions. This has been realized by the research community as well as founding organisations. One of the example is the EU Project financed under Marie-Curie programme *ModObs: Atmospheric Modelling for Wind Energy, Climate and Environment Applications: Exploring Added Value from New Observation Technique*, from which also the author of this work has been supported.

The properties of the atmospheric boundary layer offshore are significantly different from

the one onshore. The differences are mainly due to generally lower surface friction, more important influence of humidity and to a large degree the absence of the diurnal cycle of the boundary layer in the offshore conditions. The wind potential and even more the wind shear which causes loads on wind turbines crucially depends on the structure of the boundary layer. Therefore, the knowledge of the boundary layer structure is important for planning as well as operating the wind turbines. For proper and cost-efficient planning of the location for the wind parks as well as the specific wind turbine used, the long term (inter-decadal) wind speed and its variability needs to be known. Answering above mentioned questions (i.e. the knowledge of the boundary layer structure and the long term wind variability) is harder for the offshore sites, since only scarce and in time limited measurements over the sea exists. Therefore, in many cases one has to rely on the results of the numerical atmospheric models.

In this work, we tackle some questions regarding atmospheric conditions related to wind energy. The near surface wind in past climate from different data sources over the north-western Europe and north-eastern Atlantic are investigated in Ch. 3. The variability of the mean and extreme wind speed on the yearly to inter-decadal time scale has been correlated to the variability of the atmospheric forcing described by the empirically found Sea Level Pressure (SLP) patterns. The possible climate change of the near surface wind speed in the future climate under the Intergovernmental Panel on Climate Change (IPCC) Special Report on Emissions Scenarios (SRES) A2 scenario and simulated by an ensemble of Global Circulation Models (GCMs) is investigated in Ch. 4. The climate change of the near surface wind was derived from the change of the strength of SLP patterns similar to the one found in Ch. 3.

We showed that the near-surface wind conditions, especially the vertical wind shear from the atmospheric models are importantly dependent on the details of the model, especially the parameterisation of the turbulence in the atmospheric boundary layer. The simulations of the near surface wind conditions from one of the most up to date parameterisations (i.e. Mellor-Yamada-Janjić) as part of the Weather Research and Forecasting Model (WRF) have been compared with the measurements over the marine boundary layer from two measuring towers one in North Sea and one in the Baltic Sea in Ch. 5. Since we found the significant bias of the wind conditions dependent on the surface stability, we proposed the correction of the boundary layer parameterisation. It was shown that the wind conditions, especially wind shear are better simulated with the improved boundary layer parameterisation compared to the original one (Ch. 5).

The work presented in Ch. 3-5 has been prepared as a manuscripts for publications in the atmospheric journals. Additional discussion of the methodology and rationale for each of the topic is given in Ch. 2. In Ch. 6, the results are summarized and the overall conclusions are given.

Bibliography

- Ender, C., 2008a: International development of wind energy use - status 31.12.2007. *DEWI Magazine*, **33**, 43–53.
- Ender, C., 2008b: Wind energy use in Germany - status 30.6.2008. *DEWI Magazine*, **33**, 24–36.
- EU Directive, 2008, 2008: Proposal for a directive of the European parliament and of the Council on the promotion of the use of energy from renewable sources. [Http://ec.europa.eu/energy/climate_actions/doc/2008_res_directive_en.pdf](http://ec.europa.eu/energy/climate_actions/doc/2008_res_directive_en.pdf), http://ec.europa.eu/energy/climate_actions/doc/2008_res_directive_en.pdf.

2

Overview of the Methods

2.1 Introduction

The work presented in Ch. 3-Ch. 5 has been prepared for the publication in scientific journals. Therefore, the space for describing and discussing the methodology was limited. In this chapter, we discuss the background for the work and describe in more details the methods used. We start with discussing different wind datasets, specifically from reanalysis, their strengths and possible pitfalls and continue with the overview of the climate models, their usefulness and limitations in simulating the climate of the Earth. Two methods which we used for extracting the significant patterns from the multivariate data are described. On the end, the need and different approaches for the parameterisation of the boundary layer in the atmospheric models are discussed and an overview of the derivation of the Mellor-Yamada-Janjić scheme and its modifications as used in Ch. 5 are presented.

2.2 Near surface wind climate

The atmosphere is variable on the whole spectrum of time scales ranging from seconds to century and even longer. The reason for multiple scale variability is highly nonlinear behaviour of the atmosphere, where the nonlinearity is responsible for coupling between different scales as well as the variety of the external forcing (such as coupling to the ocean and land as well as the solar radiation) on numerous scales. Multiple scale variability of the atmosphere has an immediate consequence on the wind variability and thus on the wind resources for wind energy. To illustrate above discussion, let us consider the variability of the North Atlantic Oscillation Index (NAOI)¹ which is known to have a significant influence on the wind speed over the North Europe and North Atlantic in the cold part of the year. The positive NAOI is related to the above average strength of the westerly winds and the negative NAOI to the below normally strong westerly or even easterly winds over the North Atlantic and North Europe (Trigo et al., 2002). It has been observed, that the NAOI has a significant power up to the centurial and possibly even longer time scales (Hurrell and van Loon, 1997). Therefore, the decades of the above normally positive (negative) NAOI have been observed. The last episode of the above average high NAOI has extended from the mid 1960s till the end of 1990s which have been preceded by the two decades of below normally low NAOI and succeeded by the decreasing of the NAOI from late 1990s (Hurrell et al., 2003). The variability of the wind speed over the North Atlantic has been to an significant extend coherent with the variability of NAOI.

¹NAOI is usually defined as a sea level pressure difference between Azores high and Iceland low.

The knowledge of the variability of the wind speed on different time scales is crucial for wind energy for the following reasons. The variability of the wind speed on the shortest time scale (seconds to minutes) can cause damage of a wind turbine due to uneven loads on wind turbine blades. The variability of wind speed on the time scale from minutes to few days results in a variability of the produced wind power which might cause problems integrating wind power to the electricity network and providing a permanent supply of electricity. The diurnal to annual cycle of the wind speed has to be considered when planning the wind energy supply. The change of the wind speed on decadal to centurial time scales affects the production of the wind energy through the life time of wind turbines and the infrastructure and is thus important for the economically feasible planning of wind power plants. In Ch. 3 we studied the past climate of WS from monthly to decadal variability mainly over the North Sea and In Ch. 4, we investigated the possible changes of the WS resources in the next century over the North Atlantic and Europe.

2.2.1 Near Surface wind in past climate

Estimation of the past wind climate on decadal time scales over the North Atlantic (or North Sea) is complicated by the fact that homogeneous (time consistent) long time measurements over the sea do not exist. The exceptions are only the coastal areas and some of the islands. For example, measurements from FINO tower covering a few recent years (from 2004 onward) were the only source of the wind data in the North Sea available to us. Therefore to study the wind climate in past decades over the North Atlantic, one has to depend on numerical data products such as reanalysis data.

To investigate the past variability of the atmosphere over few decades as much as possible free from the artificial influence, such as spurious discontinuities and trends which can be due to the development of the observational systems (e.g. Alexandersson et al., 2000), some of the larger atmospheric centres, such as the European Centre for Medium-Range Weather Forecasts (ECMWF) and National Center for Environmental Prediction/National Center for Atmospheric Research (NCEP/NCAR) decided to reanalyse state of the atmosphere for the period of intensive atmospheric measurements (from around 1950 onward). To do this, majority of the available measurements were assimilated into the atmospheric model to produce gridded and physically consistent atmospheric fields. Since the same model is used to reanalyse the total period, the results of the reanalysis do not suffer from the inhomogeneities related to the change of the modelling system and are believed to be one of the best long term atmospheric datasets. However, the constant development of the observational system and measuring techniques of the atmosphere, as well as the change of the observational locations might seriously bias the long term trends of the reanalysis fields. With a start of the satellite era in the 1970s enormous amount of new satellite measured atmospheric data have been assimilated in the reanalysis models. The start of the assimilation of the satellite measurements might cause most serious discontinuities and spurious trends in the reanalysis data (Kalnay et al., 1996; Kistler et al., 2001). Extreme values can be especially highly influenced, since they are by definition rare and usually spatially limited. However, not all atmospheric variables are equally influenced. It has been shown that the Sea Level Pressure (SLP), due to its smooth variation in space is less prone to the possible artificial inhomogeneities (e.g. Kistler et al., 2001). On the other hand Wind Speed at 10 m height (WS) which is the main interest of this study is not a prognostic variable, but diagnosed from the wind at the first model level using the Monin-Obukhov theory. Therefore, the quality of the WS from the

reanalysis data is lower than the SLP (e.g. Kalnay et al., 1996) and can be highly influenced by the details of the model. The assimilation of the satellite measurements is expected to have a high impact on quality of the reanalysed WS.

In Ch. 3, we investigate the WS climate and its variability in around last 50 years over the North Sea and compare the WS from different reanalysis datasets in order to uncover possible problems and discontinuities in data. However, WS from different datasets can have similar problems since all reanalysis are based on virtually the same measurement data. Therefore, the patterns of the WS explaining a significant part of its variance have been isolated and related to the empirically found SLP patterns. The relationship between SLP and WS has been interpreted as a SLP forcing on WS. The WS patterns were defined based on the Empirical Orthogonal Functions (EOFs), which are described into more detail in Sec. 2.2.3. The co-variability of WS and SLP patterns through the reanalysis period has been investigated and the differences have been interpreted as a suspect for the inhomogeneity problems of the WSs. In the last part of the Ch. 3, a special attention is dedicated to the high WSs and its relationship with the SLP patterns.

2.2.2 Future change of the near surface wind climate

The possible change of the mean and extreme WSs in the future climates is crucial for efficient planning of the wind farms. Although the life time of wind turbines is around two decades and probably little affected by the climate change, the infrastructure for the (offshore) wind parks must be build (such as the transmission lines) which importantly contribute to the costs of the wind parks and whose planned life time extends up to a century and can be affected by the change of the wind climate. An example of the infrastructure is planned isolated transmission lines to be build in the North Sea (Drews et al., 2008).

The climate of the earth can be simulated by climate models of different complexities, depending on an application and the computational resources. The most simple are the *Energy Balance Models* based on vertically integrated energy balance equations and further averaging can also be done in the horizontal direction. Slightly more complex are the *Radiative-Convective Models*, where the vertical dimension is partly resolved while the vertical radiative transfer and convection are parameterised. On the other hand the most advanced models are *Global Circulation Models (GCMs)* which simulate the dynamics of the atmosphere, oceans, land surface and ice cores with a physically based approach and couple the aforementioned components together through the heat, momentum and moisture fluxes (Treut et al., 2007). There exist also the whole hierarchy of the models in their complexity between the simple radiative-convective models and GCMs. The more detailed description of the hierarchy of the climate models can be found in Schwierz et al. (2006) and the references therein. The Atmospheric part of the GCMs (AGCMs) is similar to the weather prediction models and simulates the dynamics of the atmosphere and parametrises the subgrid fluxes and physical processes (radiation, moist physics and possibly atmospheric chemistry). The AGCMs differ from the weather prediction models by interactive coupling to the lower boundary condition (i.e. ocean, land and ice surfaces) and by more comprehensive parametrisation of physical and subgrid processes. The coupling to the lower boundary conditions is important, since on the time scales of the weeks and longer the atmosphere significantly interacts with the land and the ocean surface. Parametrisations of physical and subgrid processes must be carefully done so that the model does not exhibit an unrealistic long term drift of the climate.

To simulate the climate change, the expected anthropogenic forcing in terms of the green-

house gas concentrations, land use change and other driving forces must be specified and prescribed to the model as a change of the atmospheric albedo and/or input to the atmospheric chemistry part of the model and change of the surface (land) properties. Since the anthropogenic forcing depends mainly on the demographic development, socio-economic development and technological change, the Intergovernmental Panel on Climate Change (IPCC) in its Special Report on Emission Scenario (SRES) proposed 40 scenarios describing the human development and resultant emission scenarios (Nakicenovic, 2000). As discussed in the next paragraph, one of the high uncertainties in simulating the future climate is the uncertainty of the future anthropogenic forcing.

There are three well known sources of uncertainties of the GCM results (e.g. Schwierz et al., 2006): i) uncertainty related to selection of the emission scenarios and thus the external forcing of the model; ii) uncertainty related to the unknown or imprecise initial conditions whose influence on the development of the climate system is not known a-priori; iii) the climate models are imperfect in their description of processes. The uncertainty of the emission scenarios mainly reflects the uncertainty of the future human development and climate protection practices. It is impossible to predict which of the IPCC SRES scenarios is more probable or closer to the actual future development of society. Since the climate system has highly non-linear dynamics and its evolution is irregular, the dependence of the solution on the initial conditions is not known, therefore the differences in initial conditions can lead to significantly different results. The uncertainty related to the imperfectness of the model is related both to the processes that are not physically well described in the model as well as to the ones that cannot be resolved and must be parametrised. Some of the uncertainties can be estimated by ensembles of the model results, as for example the multi-model ensemble (Palmer et al., 2005), where different models and initial conditions account for the part of the type ii and iii uncertainties.

In Ch. 4, we investigate the climate change of the WS over the Northern Atlantic and Europe. The result of the multi-model ensemble climate simulations prepared for the Fourth IPCC Assessment Report (AR4) is compared. Since the near surface wind speed (WS) is not available from most of the GCMs, we estimate its change statistically from the change of the SLP patterns. The prominent WS patterns are related to the SLP patterns and from the change of the strength of the SLP patterns the change of the WS is deduced. The estimation of climate change is limited since it assumes that the climate change is only due to the change of the strength of SLP patterns found in the past climate. However, it has been shown that the expected climate change is mainly projected on the modes of the natural variability (Corti et al., 1999), therefore above mentioned limitation is not expected to be very severe.

2.2.3 Main statistical methods used

In Ch. 3 and Ch. 4 we used the Empirical Orthogonal Function (EOF) and Trend Empirical Orthogonal Function (TEOF) analysis to extract the principal modes (spatial patterns and time series) from the gridded² WS data. The main goal of both methods is to simplify the gridded data to a few spatial patterns and corresponding time evolution while retaining the significant part of the data signal. As explained later, the EOF and TEOF analysis differ by criteria defining the significant part of the data signal.

Typically, the gridded atmospheric data are highly correlated in time³. The EOF and

²Gridded data is defined as data obtained at different locations and at different times.

³The amount of correlation between different grid points depends on the spatial scale of the principal process

TEOF analyses describe the relationship between different grid-points in gridded data as well as to uncover the minimal and optimal sets of the data needed to describe the majority of its variability. Both methods rotate the original data from the physical space (with the dimension of the number of spatial points and the base vectors defined as a delta functions at each grid point) to the synthetic space whose base vectors will be the new spatial patterns found empirically. In EOF analysis the orthogonal rotation is defined in a way that in the subspace spanned by the first base vector most of the variance of the data is captured. The second base vector is found to be orthogonal to the first one while in the subspace spanned by it most of the variance is described, etc. The TEOF method find the patterns maximising the trend⁴ of the data rather than a variance. The result of the EOF or TEOF rotation are thus spatial patterns which represent the base vectors in a new space and time series (coordinates) representing the time evolution of the spatial patterns.

EOF method has been widely used in the atmospheric research and is well documented (e.g. Preisendorfer, 1988; von Storch and Zwiers, 2003; Hannachi et al., 2007) while TEOF analysis has been recently developed and described by Hannachi (2007). Below, we give an overview of EOF and TEOF analysis. The application of the methods done by the author of the thesis are described in Ch. 3-Ch. 4.

Empirical Orthogonal Function (EOF)

Let the gridded data s measured at n locations and t times be written in the matrix \mathbf{S} with the dimension $n \times t$. The columns of matrix \mathbf{S} represent the values of s at fixed time and rows the values of s at fixed location. The values in matrix \mathbf{S} must be normalised so that each row has zero mean, i.e. the matrix \mathbf{S} consist of anomalies form the time-mean values. We denote the l -th column of the matrix \mathbf{S} by \mathbf{s}_l and define the covariance matrix \mathbf{C}_{SS} of matrix \mathbf{S} as:

$$\mathbf{C}_{SS} = \mathbf{S}\mathbf{S}^T \quad (2.1)$$

The rotation of the n -dimensional original space where the base vectors are delta functions at each grid points to the space where the first first base vector \mathbf{q}_1 (which we call Empirical Orthogonal Function, EOF) is defined in such a way that the variance of the data in a subspace defined by subtracting the original data space from the subspace spanned by \mathbf{q}_1 is minimal is preformed:

$$\frac{1}{t} \sum_{l=1}^t \|\mathbf{s}_l - \mathbf{q}_1(\mathbf{q}_1^T \mathbf{s}_l)\|^2 = \min \quad (2.2)$$

where the length of any column vector \mathbf{a} is defined as: $\|\mathbf{a}\| = \sqrt{\mathbf{a}^T \mathbf{a}}$ and the base vector in new space has a unit length:

$$\|\mathbf{q}_1\| = 1 \quad (2.3)$$

The Eq. 2.2 can be written as:

responsible for the variability of the field and a spatial resolution of the field.

⁴Exact definition of data trend is given later.

$$\frac{1}{t} \sum_{l=1}^t (\mathbf{s}_l^T - \mathbf{q}_1^T (\mathbf{q}_1^T \mathbf{s}_l)) (\mathbf{s}_l - \mathbf{q}_1 (\mathbf{q}_1^T \mathbf{s}_l)) = \frac{1}{t} \sum_{l=1}^t (\mathbf{s}_l^T \mathbf{s}_l - (\mathbf{q}_1^T \mathbf{s}_l)(\mathbf{q}_1^T \mathbf{s}_l)) \quad (2.4)$$

The term $\sum_{l=1}^t \mathbf{s}_l^T \mathbf{s}_l$ equals to the sum over the time and components of the same component of vector \mathbf{s}_l and thus equals to the trace (sum of the diagonal elements) of the matrix \mathbf{C}_{SS} . The term $\sum_{l=1}^t (\mathbf{q}_1^T \mathbf{s}_l)(\mathbf{q}_1^T \mathbf{s}_l)$ can be written as $\mathbf{q}_1^T \mathbf{C}_{SS} \mathbf{q}_1$ using $\mathbf{q}_1^T \mathbf{s}_l = \mathbf{s}_l^T \mathbf{q}_1$ and considering that multiplication of matrices is associative. Eq. 2.2 can be thus simplified to yield:

$$\frac{1}{t} (\text{tr}(\mathbf{C}_{SS}) - \mathbf{q}_1^T \mathbf{C}_{SS} \mathbf{q}_1) = \min \quad (2.5)$$

In Eq. 2.5, tr denotes trace of matrix. The first term on the left hand side of Eq. 2.5 represents the average variance of data. Finding minimum of Eq. 2.5 with respect to \mathbf{q}_1 is equivalent of finding maximum of:

$$\mathbf{q}_1^T \mathbf{C}_{SS} \mathbf{q}_1 = \max \quad (2.6)$$

The solution of Eq. 2.6 under the constraint in Eq. 2.3 can be found using the method of the Lagrange multipliers:

$$\frac{\partial}{\partial \mathbf{q}_1} (\mathbf{q}_1^T \mathbf{C}_{SS} \mathbf{q}_1 + \lambda(1 - \mathbf{q}_1^T \mathbf{q}_1)) = 0 \quad (2.7)$$

where λ is Lagrange multiplier and the operator $\partial/\partial \mathbf{q}_1$ denotes the partial derivative with respect to every component of vector \mathbf{q}_1 which can be written in a vector form as:

$$\frac{\partial}{\partial \mathbf{q}_1} = \begin{bmatrix} \frac{\partial}{\partial q_{11}} \\ \frac{\partial}{\partial q_{12}} \\ \dots \\ \frac{\partial}{\partial q_{1N}} \end{bmatrix} \quad (2.8)$$

where the second index of vector \mathbf{q} in Eq. 2.8 denotes the component of vector. The derivation of Eq. 2.7 yields:

$$\mathbf{C}_{SS} \mathbf{q}_1 = \lambda \mathbf{q}_1 \quad (2.9)$$

The solution of minimisation problem in Eq. 2.2 under the constraint in Eq. 2.3 is thus one of the eigenvectors of matrix \mathbf{C}_{SS} . In order that Eq. 2.6 reaches maximum, the eigenvector which correspond to the highest eigenvalue is the first EOF spatial pattern.

Having found the first spatial pattern the whole procedure is repeated minimising equation:

$$\frac{1}{T} \sum_{l=1}^T \|\mathbf{s}_l - \mathbf{q}_1 (\mathbf{q}_1^T \mathbf{s}_l) - \mathbf{q}_2 (\mathbf{q}_2^T \mathbf{s}_l)\|^2 = \min \quad (2.10)$$

with constrain

$$\|\mathbf{q}_2\| = 1 \quad (2.11)$$

With similar derivation as for the first EOF spatial pattern the result yields that the second spatial pattern is the eigenvector of matrix \mathbf{C}_{SS} which corresponds to its second highest eigenvalue. Similarly, the third pattern is the eigenvector of \mathbf{C}_{SS} corresponding to the third highest eigenvalue, etc. Therefore, the problem of finding EOF spatial patterns is simplified to finding eigenvectors of matrix \mathbf{C}_{SS} .

Since matrix \mathbf{C}_{SS} is Hermitian (real and symmetric), eigenvalues of \mathbf{C}_{SS} are non-negative and eigenvectors corresponding to distinct eigenvalues are orthogonal (e.g. Weisstein, 2009). If two or more eigenvalues are the same, which is extremely unusual in real geophysical applications, the subspace spanned by eigenvectors that corresponds to identical eigenvalues can be decomposed in such a way that spatial patterns are orthogonal.

The time series representing the time evolution of the pattern \mathbf{q}_i can be written in a row matrix (\mathbf{a}_i^T) which we name Principal Components (PC):

$$\mathbf{a}_i^T = \mathbf{q}_i^T \mathbf{S} \quad (2.12)$$

It can be shown that the PCs are uncorrelated:

$$\mathbf{a}_i^T \mathbf{a}_j = \mathbf{q}_i^T \mathbf{S} \mathbf{S}^T \mathbf{q}_j = \mathbf{q}_i^T \mathbf{C}_{SS} \mathbf{q}_j = \mathbf{q}_i^T \lambda_j \mathbf{q}_j = \lambda_j \delta_{ij} \quad (2.13)$$

where we have used that the EOFs are eigenvectors of the covariance matrix. With all n modes, all the variance of the data can be explained:

$$\frac{1}{t} \sum_{l=1}^t \left\| \mathbf{s}_l - \sum_{k=1}^n \mathbf{q}_k (\mathbf{q}_k^T \mathbf{s}_l) \right\|^2 = 0 \quad (2.14)$$

which can be rewritten as:

$$\frac{1}{t} \sum_{l=1}^t \left(\mathbf{s}_l^T \mathbf{s}_l + \frac{1}{t} \sum_{k=1}^n (\mathbf{q}_k^T \mathbf{s}_l) (\mathbf{q}_k^T \mathbf{s}_l) \right) = 0 \quad (2.15)$$

$$\text{var}(s) = \sum_{k=1}^n \mathbf{q}_k^T \mathbf{C}_{SS} \mathbf{q}_k = \sum_{k=1}^n \lambda_k \quad (2.16)$$

The variance of data is thus broken into n components, where the eigenvalues of matrix \mathbf{C}_{SS} are proportional to the explained variance by the corresponding mode. The original data can be rewritten as a sum of the product of the PCs (which represent the coordinates in a new space) and the base vectors (EOFs):

$$\mathbf{S} = \sum_{i=1}^n \mathbf{q}_i \mathbf{a}_i^T \quad (2.17)$$

where it is anticipated that only the first few k modes ($k \ll n$) are sufficient to explain the majority of the variance of the data while the remaining $k + 1 \dots n$ modes explain only the marginal part of the variance and can be neglected.

On the end of the analysis, we choose to normalise the patterns in a way that the a_i -s have the unit variance (by dividing the a_i by its variance and multiplying the corresponding

spatial pattern by the same number) while not influencing the product in Eq. 2.17. We prefer this normalisation, since the spatial patterns now represent the typical variability of the field with the relative phase angle. Therefore we assign the unit of the field to the spatial pattern.

EOF is a linear method, i.e. it maximises the linear relationship between the data points (covariance) but overlooking any nonlinear relationship between the data points. Attempts to generalise the EOF to include the nonlinear relationship have been done (e.g. Monahan, 2000). However, in this study we used only the linear EOF.

Trend Empirical Orthogonal Function (TEOF)

Quite often in the climate research it is interesting to study trend structures of a gridded data, where trend is understood as a smooth (monotonous) function with a systematic variation of time series. For example, the study of the trend in the climate data is important to uncover the anthropogenic influence on the climate system. Considering the complexity of the climate system, it is expected that the trend characteristics will vary from one location to another, therefore the trend structure could be composed of more than one single pattern. EOF is the method used to uncover the relationship between different space points in a gridded data, but it is not specifically designed for searching of the trend, since the EOF modes are subject to the maximal explained variance of the data. Recently Trend Empirical Orthogonal Function (TEOF) method was developed by Hannachi (2007), which isolates the trend patterns of the gridded data from the remaining no-trend part of the data.

To resolve the issue of trend, the data in matrix \mathbf{S} is transformed to matrix \mathbf{Q} , so that the data in matrix \mathbf{Q} measures the monotonicity of original data. To achieve this, each row of the matrix \mathbf{S} is sorted from the smallest to the highest value. The newly sorted data can be seen as some permutation of the original data. The permutation that was needed to sort the i -th row of the matrix \mathbf{S} is applied to the row vector $\{1, 2, 3, \dots, t\}$ and its result is written in the i -th row of matrix \mathbf{Q} . Therefore, rows of the matrix \mathbf{Q} consist of the position of the original data in a sorted dataset and thus measure the monotonicity of the i -th row of matrix \mathbf{S} . By looking at the maximum correlation of the data in matrix \mathbf{Q} one attempts to find times when different time series are increasing or decreasing together. To do this, the EOF analysis of the matrix \mathbf{Q} is performed. Therefore, the EOF patterns and PC time series of the matrix \mathbf{Q} are exactly what we are looking for since they represent the patterns and the time series of the data which explain the highest part of the data trend.

Now, the results (EOF modes of matrix \mathbf{Q}) must be transformed back to the original space. To do this, first the time series is calculated:

$$\mathbf{w}_i^T = \mathbf{v}_i^T \mathbf{S} \quad (2.18)$$

where \mathbf{v}_i^T is the i -th PC of matrix \mathbf{Q} . The i -th TEOF spatial pattern ($\tilde{\mathbf{q}}_i$) of data is scaled map of the correlation coefficients between the time series \mathbf{w}_i^T and \mathbf{S} :

$$\tilde{\mathbf{q}}_i = \frac{\mathbf{S} \mathbf{w}_i^T}{\|\mathbf{S} \mathbf{w}_i^T\|} \quad (2.19)$$

The i -th TPC is obtained as:

$$\tilde{\mathbf{a}}_i^T = \tilde{\mathbf{q}}_i^T \mathbf{S} \quad (2.20)$$

Hannachi (2007) argues that TEOF modes have the following advantages over the EOF

modes: i) The TEOF is based on the correlation of ranks, therefore it is not restricted to search for a linear relationship in data; ii) It was shown by selected cases, that the method is well able to separate the trend patterns from the no-trend patterns, which can be observed by the gap between the explained variance of the trend and no-trend patterns (λ). In case of the EOF patterns, the separation of the noise from signal is usually not as clear as in case of TEOF patterns.

2.3 Boundary Layer Parameterisation in Atmospheric Models

Turbulence in the atmospheric Planetary Boundary Layer (PBL)⁵ has an important impact on the whole atmosphere. Atmospheric mesoscale models whose main goal is to accurately simulate mesoscale processes⁶ cannot explicitly resolve the turbulence due to their low spatial and temporal resolution, but have to account for its influence on the mesoscale flow. Turbulence directly influences the mesoscale flow only in some parts of the atmosphere such as in the PBL, areas of intensive convection and strong wind shears (jet streams). From the perspective of the mesoscale flow, turbulence causes an increased (esp. vertical) mixing and can contribute to the paramount part of the flux of momentum, heat, moisture and other atmospheric constituents.

From wind-energy point of view, the proper description of the PBL turbulence in the mesoscale models is crucial, since the turbulent vertical mixing of momentum determines the vertical wind shear in the boundary layer. Wind shear is important for wind energy for the following reasons: i) It influences the wind speed at the specific height by ‘modulating’ the geostrophic wind speed from above boundary layer; ii) The wind shear causes the loads on the wind turbines. Loads due to the wind shear are especially serious for the larger wind turbine rotors. In this section, we describe the need for PBL turbulence parameterisation in atmospheric mesoscale models and give an overview of Mellor-Yamada-Janjić boundary and surface layer parameterisation scheme which is used to simulate wind conditions and improved as described in Ch. 5.

2.3.1 Need for PBL parameterisation in atmospheric models

The dynamics of the atmosphere is governed by partial differential equations, describing the conservation laws for motion (Navier-Stokes, therefore NS equation), energy, mass of dry air (continuity equation), water and other constituents (Pielke, 2002). The general analytic solution of the governing equations does not exist, therefore the equations are numerically solved, usually on a predefined grid (Eulerian perspective of fluid dynamics). In Cartesian coordinates $(x, y, z) = (x_1, x_2, x_3)$, the NS equation and the equation for conservation of heat in the Earth rotating frame of the reference can be written as:

$$\frac{\partial u_i}{\partial t} = -u_j \frac{\partial u_i}{\partial x_j} - \frac{1}{\rho} \frac{\partial p}{\partial x_i} - 2\varepsilon_{ijk} u_j \Omega_k - g\delta_{i3} + \nu \frac{\partial^2 u_i}{\partial x_j \partial x_j} \quad (2.21)$$

$$\frac{\partial \theta}{\partial t} = -u_i \frac{\partial \theta}{\partial x_i} + S_\theta + \alpha \frac{\partial^2 \theta}{\partial x_j \partial x_j} \quad (2.22)$$

⁵Planetary boundary layer is defined as part of the atmosphere that is directly influenced by the presence of the earth’s surface and responds to surface forcing with a time scale of an hour or less (Stuhl, 1988).

⁶Mesoscale processes are the processes on the order of few to few hundred kilometers and time of hours.

CHAPTER 2. OVERVIEW OF THE METHODS

In the above equations, u_i represents the wind speed component, ρ air density, p pressure, Ω_i components of the Earth angular velocity projected on the local Cartesian system, g gravitational constant ($g = 9.81 \text{ m s}^{-1}$), θ potential temperature⁷, S_θ represents the diabatic heat source (from radiation and the phase change of water), ν and α are kinematic viscosity and thermal diffusivity respectively and ε_{ijk} is Levi-Civita tensor. In the upper equations and further in this chapter, Einstein summation notation is used. Eq. 2.22 can be used as a governing equation for the conservation of mass of moisture and other water species (e.g. liquid water, ice, etc.) as well as any other atmospheric constituents (e.g. aerosol, CO_2 , tropospheric ozone, etc) which can be modelled by the mesoscale model. In this case, the variable θ must be replaced by the mass of the species under interest and the production/sink sources (S_θ) as well as the diffusion coefficient (α) must be specified accordingly.

One of the interesting terms in the Eqs. 2.21 and 2.22 are the nonlinear terms (first terms on the right hand side of equations) which represent the advection of the momentum and heat. This terms couple processes on different scales (e.g. Pielke, 2002). Therefore all relevant scales (from the smallest turbulent to planetary scale) must be resolved by the model to properly describe the dynamics of the atmosphere. If the mesoscale models covers the whole atmosphere, the model is able to resolve the larger scales. More usual practice is that mesoscale models are used as a limited area models and the contribution of the larges scales is taken into account through the boundary conditions. To resolve the smallest scales, the spatial resolution⁸ of the model would have to be around 1 cm (Pielke, 2002). This can be achieved for example by Direct Numerical Simulation (DNS) models, where the resolution of the model is fine enough to capture scales of motion up to the smallest relevant (dissipation) scale (Davidson, 2006). However, tremendous amount of the computing time is required to simulate large domains with a DNS model. For mesoscale modes where the model typically covers the areas of $\sim 10^5 \text{ km}^3$ - 10^9 km^3 , the DNS approach is not feasible due to tremendous computing power required. The achievable spatial resolution of mesoscale models with the current computer power is on the order of 1 km-10 km, while the influence of the small, unresolved scales on the resolved scale flows must be described statistically (i.e. parametrised).

In the PBL which is the interest of this study, the main assumption of the mesoscale models is that all scales larger than the atmospheric turbulence are resolved, and that there is a sufficient gap between the turbulent and larger scale motion. Therefore, the parametrisation of the unresolved scale in the PBL in mesoscale models is the parametrisation of the turbulence. The goal of the parametrisation is not to describe the turbulence in detail, but to statistically describe its influence on the larger (resolved) scale flow. From the perspective of the mesoscale flow, the main role of the turbulence in the PBL is to vertically mix the boundary layer and to dissipate the energy of the flow through the turbulent scales to the heat.

The above discussion can be written in the mathematical terms as follows. Any variable φ can be written as a sum of its mean value integrated over the model grid cell and over the model time step ($\overline{\varphi}$) and the anomaly (variation) from the mean value inside the grid cell and integration time (φ'), which represent unresolved part of the variable. The process of decom-

⁷Potential temperature is defined as: $\theta = T \left(\frac{p_{00}}{p} \right)^{R/c_p}$ where T is absolute temperature, $p_{00} = 1000 \text{ hPa}$ reference pressure, c_p specific heat of dry air at constant pressure and R gas constant for dry air. θ is preferred over T , since it is constant for adiabatic processes.

⁸Resolved scale is proportional to the spatial resolution of the model. For the discussion here, we assume that the smallest resolved scale is equal to the resolution of the model.

2.3. BOUNDARY LAYER PARAMETERISATION IN ATMOSPHERIC MODELS

posing the variables to the mean and the anomaly part is called Reynolds decomposition:

$$\varphi = \bar{\varphi} + \varphi' \quad (2.23)$$

where $\bar{\varphi}$ is defined as:

$$\bar{\varphi} = \frac{1}{\Delta t \Delta x \Delta y \Delta z} \int_t^{t+\Delta t} \int_x^{x+\Delta x} \int_y^{y+\Delta y} \int_z^{z+\Delta z} \varphi \, dz \, dy \, dx \, dt \quad (2.24)$$

In Eq. 2.24, Δx , Δy , Δz and Δt represents the spatial and temporal resolution of the model. From assumption that the model can resolve all scales higher than turbulent, it follows that φ' represent the turbulent part of the variable φ . With the Reynolds decomposition, the NS and heat conservation for the mean values can be written as:

$$\frac{\partial \bar{u}_i}{\partial t} = -\bar{u}_j \frac{\partial \bar{u}_i}{\partial x_j} - \frac{\partial \overline{u'_i u'_j}}{\partial x_j} - \frac{1}{\bar{\rho}} \frac{\partial \bar{p}}{\partial x_i} - 2\varepsilon_{ijk} \bar{u}_j \Omega_k - g\delta_{i3} + \nu \frac{\partial^2 \bar{u}_i}{\partial x_j \partial x_j} \quad (2.25)$$

$$\frac{\partial \bar{\theta}}{\partial t} = -\bar{u}_i \frac{\partial \bar{\theta}}{\partial x_i} - \frac{\partial \overline{u'_i \theta'}}{\partial x_j} + S_\theta + \alpha \frac{\partial^2 \bar{\theta}}{\partial x_j \partial x_j} \quad (2.26)$$

Where the assumptions that the small scale flow is non-divergent ($\partial u'_i / \partial x_i = 0$) and the Boussinesq approximation for density variations (i.e. ρ' is small, except when multiplied by gravitational constant g) (e.g. Pielke, 2002) were used.

In the equations for the mean quantities (Eqs. 2.25 and 2.26), the new terms appear, namely the gradients of the velocity anomaly covariances ($\overline{u'_i u'_j}$) and gradients of the velocity and the potential temperature anomaly covariances ($\overline{u'_i \theta'}$). The covariances represent the kinematic momentum and heat flux⁹. The components of the turbulent momentum flux can be written in a so called Reynolds stress tensor¹⁰ which is symmetric 2-dimensional tensor. Although in the upper equations, the fluxes are meant to represent the time-space average values, the parameterisations tries to estimate the ensemble mean values (i.e. the most probable values) neglecting the possible variability between the space averaged values and ensemble mean values.

2.3.2 Approaches for boundary layer parameterisation

Virtually all of the boundary layer parameterisations neglect the horizontal fluxes and the vertical flux of the vertical velocity, while the parameterised fluxes are described through vertical profiles in terms of the mixing coefficients (K_M and K_H) as:

$$\overline{u'_i w'} = K_M \frac{\partial u_i}{\partial z} \quad i = 1, 2 \quad (2.27)$$

$$\overline{\theta' w'} = K_H \frac{\partial \theta}{\partial z} \quad (2.28)$$

Therefore, the parameterisations schemes have to specify mixing coefficients. Currently the following three types of the models for the boundary layer mixing coefficients are widely

⁹The fluxes are normalized by density.

¹⁰Reynolds tensor is called stress tensor, since the turbulent momentum flux has been historically treated similarly as kinetic viscosity.

used in the numerical atmospheric models:

- Mixing coefficients are a function of local turbulent measure such as a gradient Richardson number
- Nondimensional profiles of the mixing coefficients are prescribed
- Mixing coefficients are function of Turbulent Kinetic Energy (TKE)

The simplest turbulent models used in the state of the art numerical models are the ones in which the mixing coefficients are function of the local gradient Richardson number (e.g. Louis, 1979). Gradient Richardson number is used as a measure of the relative importance of the buoyant and shear production for the TKE. The basic idea of these type of models is that the turbulence characteristics (and mixing coefficients) are crucially dependent on whether the turbulence is produced by shear or by buoyancy. This type of models have been used in many global models, such as in NCEP/NCAR Reanalysis (Kalnay et al., 1996), since they are computationally cheap. Their main disadvantages arise from the fact they are local (i.e. mixing depends on the local properties of turbulence) which is very unrealistic especially in the convective boundary layer where typically the turbulent eddies are driven from the surface and adjusted by the property of the boundary layer. Thus, the turbulence and the turbulent mixing depends on the whole vertical structure of the boundary layer. On top of this, due to the local characteristics, these schemes are prone to be numerically unstable (Teixeira and Cheinet, 2004, and references therein).

Slightly complex PBL models have prescribed shape of the mixing coefficient profiles. An example is the model described by Troen and Mahrt (1986). The main advantage of this types of models is that they are not dependent on the local nature of the turbulent property of the atmosphere (i.e., Richardson number). In Troen and Mahrt (1986) parameterisation, the top of the boundary layer is diagnosed from the turbulent properties at the surface. The parabolic profile of K_M and K_H is prescribed with zero limiting values at the ground and at the top of the boundary layer. Due to the failure of the model to properly represent the entrainment at the top of the boundary layer, additional mixing term is added to the mixing coefficient of K_H , which represent the effects of the large eddies at the top of the boundary layer and is not the function of the vertical gradient of the potential temperature. The two major drawback of these type of parameterisations are: i) the mixing is crucially depend on the diagnosed boundary layer height which is usually hard to define well in the numerical model and; ii) the imposed correction for the K_H at the top of the boundary layer is somehow artificial (Teixeira and Cheinet, 2004).

More physically models are based on the Turbulent Kinetic Energy (TKE), where the prognostic equation for the TKE is solved and the mixing coefficients are the function of the TKE. Mellor-Yamada-Janjić scheme, which was used in this work is the TKE based scheme and is described in detail below. The main advantage of these type of models is that they are able to represent the sources and sinks of TKE and the non-local mixing in a more physical way than the previously described models. The main disadvantage is that the number of closure assumptions have to be defined, including the macroscopic turbulence length scale and higher computational expense which is mainly due to the need to solve the prognostic equation for TKE.

Recently, some new parameterisation techniques for simulating the boundary layer have been described. One example is the so called *Asymmetrical Convective Model* by Pleim (2007). In this model, the turbulent mixing is the sum of two processes: i) the local mixing whose strength generally decay with the height and; ii) nonlocal transient mixing which mixes the atmosphere through the whole vertical column. The transient mixing represent the nonlocal

2.3. BOUNDARY LAYER PARAMETERISATION IN ATMOSPHERIC MODELS

mixing mainly in the convective boundary layer. This model has been implemented in the last version of WRF mesoscale model (Skamarock et al., 2008). Siebesma et al. (2007) and Soares et al. (2007) proposed the *Eddy-Diffusivity/Mass-Flux* parameterisation, where the turbulent mixing is calculated as a sum of the i) exchange coefficients (K_M and K_H) based on the prognostic equation for TKE as in the TKE based boundary layer schemes and; ii) an additional mass flux parameterisation which is traditionally used to parameterise moist convection and whose goal is to describe updrafts, downdrafts and resultant subsidence due to the convective clouds. In this way the parameterisation of the boundary layer and convection is done by one model. They argue that with the inclusion of the traditional boundary and moist convection parameterisation in one parameterisation they are able to better reproduce the upper part of the boundary layer, especially in the stratocumulus topped boundary layers, which is often the case in the marine boundary layer.

2.3.3 Surface layer parameterisation

In the surface layer, which in the atmospheric models is defined to extend from the surface to the first model level, the vertical profiles are expected to be far from linear, therefore the linear discretization of the boundary layer model which is performed higher in the atmosphere would lead to high inaccuracies. Therefore, the first model level is related to land/ocean surface layer through the Monin-Obukhov scaling theory (e.g. Stuhl, 1988). Monin-Obukhov scaling theory proposes that the nondimensional wind shear in the surface layer is a function of the nondimensional stability only:

$$\frac{kz}{u_*} \frac{\partial u}{\partial z} = \phi_M \left(\frac{z}{L} \right) \quad (2.29)$$

where in the Eq. 2.29 $u_* = (\overline{u'w'} + \overline{v'w'})^{1/4}$ denotes the friction velocity and represent the velocity scale, $L = u_*^3 \theta / (kg \overline{w'\theta'})$ is Obukhov length, z/L represent the nondimensional stability and ϕ_M is the empirical function of the nondimensional stability. Assuming that the heat and momentum fluxes are almost constant within the surface layer Eq. 2.29 can be integrated in a vertical from a roughness length (z_0) which represent the height where the wind speed is zero and depends on the roughness of underlying surface to the first model level (z_1). The integration of Eq. 2.29 yield:

$$u(z_1) = \frac{u_*}{k} \left[\ln \frac{z}{z_0} + \psi_M \left(\frac{z}{L} \right) \right] \quad (2.30)$$

where the integrated stability function ψ is defined as:

$$\psi_M(\xi) = \int_0^\xi \frac{\phi_M(\xi) - 1}{\xi} d\xi \quad (2.31)$$

In Eq. 2.31, the lower limit for the integration is taken to be 0 instead of z_0 and ξ is an integration constant.

With similar scaling arguments, the vertical profiles of potential temperature, moisture and other constituents can be derived. For example, the potential temperature at the first model level can be related to its surface value (θ_S) as:

$$\theta(z_1) - \theta_S = \frac{\theta_*}{k} \left[\ln \frac{z}{z_{0H}} + \psi_H \left(\frac{z}{L} \right) \right] \quad (2.32)$$

where the integrated stability function for the temperature is calculated as:

$$\psi_H(\xi) = \int_0^\xi \frac{\phi_H(\xi) - 1}{\xi} d\xi \quad (2.33)$$

In the upper equations, the nondimensional heat profile (ϕ_H) and the roughness coefficient (z_{0H}) are different that the one for momentum. The temperature scale in the surface layer is defined as $\theta_* = \overline{\theta'w'}/u_*$.

2.3.4 Ideas for stochastic boundary layer parameterisation

As far as we are aware all of the parameterisations in the state of the art atmospheric models, including boundary layer are deterministic. In the deterministic parameterisation the ensemble mean (i.e. the most probable value) of subgrid scale processes are parameterised and their tendency is included in the prognostic equations for the resolved scale flow. With this, the variability of the tendency of parameterised processes from one to the other grid box/time step is neglected. With the other words, the parameterisation predicts only the mean values of tendency of subgrid scale processes and ignores higher order moments.

On the other hand, it has been shown that ignoring the stochastic nature of subgrid scale processes can importantly influence the results of the atmospheric models. For example, Palmer (2001) showed that the behaviour of the simple Lorenz nonlinear dynamical system¹¹ can be very sensitive on the truncation order and whether the truncated processes are parameterised in a stochastic or deterministic way. His experiments showed that neglecting the stochastic nature of the parameterised processes can lead to totally different behaviour of the system. Also in the context of the global atmospheric models it has been realized that some of the problems of the models can be due to the deterministic parameterisation of the subgrid scale processes. The examples include i) generally too strong westerly winds over the temperate latitudes which can be due to the deterministic parameterisation of the gravity wave drag; ii) the inability of the global models to realistically simulate the areas of convection which has an immediate influence on the radiation budget (Buizza et al., 1999).

Only recently, the option to include the stochastic parameterisations in an atmospheric models have been studied. Buizza et al. (1999) investigated the influence of the stochastic vs. deterministic parameterisation in global atmospheric model on the above mentioned too strong westerly winds over the temperate latitudes. He constructed ad-hoc stochastic parameterisation of subgrid processes by multiplication of the subgrid scale tendencies by the random number from the uniform distribution within interval [0.5 1.5]. He showed on selected case studies that changing the deterministic to stochastic parameterisations can lead to high differences in the results and possibly leads to the decrease of the too strong westerlies over the temperate latitudes. Teixeira and Reynolds (2008) proposed the stochastic parameterisation that would be more physical than the one of Buizza et al. (1999). Instead of using ad-hoc assumption for the variability of the subgrid scale fluxes, they propose the simple model to estimate the variance of the subgrid scale fluxes and then prescribe the subgrid scale fluxes to be normally distributed with the calculated variance. The applicability of the model by Teixeira and Reynolds (2008) is yet to be investigated.

It is not exactly clear what would be the all of the consequences of changing the de-

¹¹Lorenz system is the system of nonlinear partial differential equations and can be seen as an extremely simplified equivalent to the equations describing the dynamics of the atmosphere.

2.3. BOUNDARY LAYER PARAMETERISATION IN ATMOSPHERIC MODELS

terministic PBL parameterisation in atmospheric models to stochastic. We are not aware of any work that investigates this topic. With the stochastic parameterisation, it would be possible to better simulate the intermittent behaviour of the turbulence especially in the stable boundary layer and which the current mesoscale models are not able to predict. In the GABLS¹² inter-comparison study (Cuxart et al., 2006) of numerous numerical models, it was shown that in the stable boundary layer virtually all of the models over-predict the vertical mixing which leads to too deep boundary layers and unrealistic vertical profiles. The too strong vertical mixing in the stable layer seems to be needed by the boundary layer models to assure the numerical stability of the models. With the stochastic parameterisation, the net too high vertical mixing could be avoided thus leading to better prediction of boundary layer heights and vertical wind profiles. Inclusion of the realistic stochastic parameterisation of PBL could also help to simulate the higher order statistics of the wind properties, such as the wind gusts which are important for many applications including wind energy. In this work we do not address the question of the stochastic parameterisation, but leave it as an interesting possibility for future work.

2.3.5 Mellor-Yamada-Janjić models

Prognostic equations for turbulent momentum and heat flux can be written, by manipulation of Eqs. 2.21 and 2.22 with the Reynolds decomposition (e.g. Stuhl, 1988) as:

$$\begin{aligned} \frac{\partial \overline{u'_i u'_j}}{\partial t} = & -\overline{u_k} \frac{\partial \overline{u'_i u'_j}}{\partial x_k} - \overline{u'_i u'_k} \frac{\partial \overline{u_j}}{\partial x_k} - \overline{u'_j u'_k} \frac{\partial \overline{u_i}}{\partial x_k} - \frac{\partial \overline{u'_i u'_j u'_k}}{\partial x_k} \\ & + \frac{g}{\theta} (\delta_{j3} \overline{u'_i \theta'} + \delta_{i3} \overline{u'_j \theta'}) + \frac{p'}{\rho} \left(\frac{\partial u'_i}{\partial x_j} + \frac{\partial u'_j}{\partial x_i} \right) - 2\nu \frac{\partial \overline{u'_i \partial u'_j}}{\partial x_k \partial x_k} \end{aligned} \quad (2.34)$$

$$\begin{aligned} \frac{\partial \overline{u'_i \theta'}}{\partial t} = & -\overline{u_k} \frac{\partial \overline{\theta' u'_i}}{\partial x_k} - \frac{\partial \overline{\theta' u'_k u'_i}}{\partial x_k} + \alpha \frac{\partial}{\partial x_k} \left(u'_i \frac{\partial \theta'}{\partial x_k} \right) + \nu \frac{\partial}{\partial x_k} \left(\theta' \frac{\partial u'_i}{\partial x_k} \right) \\ & - \frac{\partial}{\partial x_j} (\overline{p' \theta'}) - \varepsilon_{ijk} \Omega_j \overline{u'_k \theta'} - \theta' u'_k \frac{\partial \overline{u_i}}{\partial x_k} + \delta_{i3} \frac{\overline{\theta'^2}}{\theta} g + p' \frac{\partial \theta'}{\partial x_j} \end{aligned} \quad (2.35)$$

In Eq. 2.35, the covariance of the potential temperature anomaly appear for which the equation could be derived from Eq. 2.22 using Reynolds decomposition:

$$\frac{\partial \overline{\theta'^2}}{\partial t} = -\overline{u_k} \frac{\partial \overline{\theta'^2}}{\partial x_k} + \alpha \frac{\partial^2 \overline{\theta'^2}}{\partial x_k \partial x_k} - 2\alpha \frac{\partial \overline{\theta'}}{\partial x_k} \frac{\partial \overline{\theta'}}{\partial x_k} - 2\overline{u'_k \theta'} \frac{\partial \overline{\theta}}{\partial x_k} \quad (2.36)$$

In the prognostic equations for the turbulent fluxes (Eqs. 2.34-2.36), the higher order covariances of anomalies appear ($\overline{u'_i u'_j u'_k}$, $\overline{u'_i u'_j \theta}$), as well as other unknown terms. The prognostic equations for the unknown terms in Eqs. 2.34-2.36 can be written, but then in those equations even more unknown terms appear. The process of writing the prognostic equations for the unknown terms produces more and more unknown terms and does not lead to the closed set of the equations. This result indicate that the atmospheric flow cannot be

¹²GABLS stand for Global energy and Water Cycle Experiment (GEWEX) Atmospheric Boundary Layer Study

exactly described by resolving just the larger scales of the fluid and statistically (as average) describe the unresolved part of the flow (Davidson, 2006). At some point, the closure assumptions for the unknown terms must be made (e.g. defining unknown quantities in terms of the known) to form the closed set of equations. In this work, we used the Mellor-Yamada models (Mellor and Yamada, 1974, 1982) where second order closure (closure assumptions for the unknown terms in the Eqs. 2.34-2.36) are defined.

Closure assumptions for Mellor-Yamada models

In the Mellor-Yamada models, the closure assumptions for the unknown terms in Eqs. 2.34 - 2.36 are defined (Mellor, 1973). Here, we give the overview of the closure assumptions. For further discussions, the Turbulent Kinetic Energy (TKE) representing the energy containing part of the Reynolds stress tensor is defined as:

$$q^2 = \frac{1}{2} \overline{u'_i u'_i} \quad (2.37)$$

The role of the covariance between the pressure and the strain of velocity anomalies¹³ in Eq. 2.34 is to distribute the TKE between different space components while not contributing to the change of the total TKE. This term is modelled as proposed by Rotta (1951):

$$\overline{p' \left(\frac{\partial u'_i}{\partial x_j} + \frac{\partial u'_j}{\partial x_i} \right)} = -\frac{q}{3l_1} \left(\overline{u'_i u'_j} - \frac{\delta_{ij}}{3} q^2 \right) + Cq^2 \left(\frac{\partial U_i}{\partial x_j} + \frac{\partial U_j}{\partial x_i} \right) \quad (2.38)$$

Actually, in Eq. 2.38, only the two higher order terms of the Rotta (1951) model are considered: i) The so called slow or return-to-isotropy term (first term on the right hand side of Eq. 2.38) whose role is to redistribute the TKE from the space components containing more than average energy to the ones containing less and is the function of the measure of the anisotropy $\left(\overline{u'_i u'_j} - q^2 \delta_{ij} / 3 \right)$. It could be shown that without the return-to-isotropy term, the turbulence described by Eq. 2.34 would become more and more anisotropic which contradicts observations (Davidson, 2006). ii) The rapid term as a function of the strain of the large scale velocities (last term on the right hand side of Eq. 2.38) which simulate the long distance effects of the pressure anomalies. The model for the pressure redistribution term is one of the most controversial closure assumptions and has been questioned by many authors (e.g. Cheng et al., 2002).

In similar fashion, the covariance between the pressure anomalies and gradient of temperature anomalies is written, but without the terms proportional to the strain of the large scale velocity:

$$\overline{p' \frac{\partial \theta'}{\partial x_j}} = -\frac{q}{3l_2} \overline{u'_j \theta'} \quad (2.39)$$

In Eqs. 2.38 and 2.39, l_1 and l_2 are the typical length scales over which the pressure anomalies are able to redistribute the turbulence, and C is a constant. Both length scales as well as constant C must be obtained from measurements.

The dissipation of TKE to heat (last term in Eq. 2.34) is modelled using Kolmogorov cascade theory. The turbulent energy is dissipated to the heat only at the smallest scales

¹³Strain of the velocity anomalies is $\frac{\partial u'_i}{\partial x_j} + \frac{\partial u'_j}{\partial x_i}$

2.3. BOUNDARY LAYER PARAMETERISATION IN ATMOSPHERIC MODELS

while the dissipation equals to the energy transfer from the largest scales through the energy cascade. The energy transfer through the energy cascade is proportional to the $dU^2/dt \sim -U^2/(L/U)$, where U is the typical velocity scale and L the length scale of the large eddies. We take TKE as the velocity scale and assume that the turbulence is isotropic on small scales (the energy dissipation is isotropic) and arrive to the equation for the energy dissipation:

$$2\nu \frac{\overline{\partial u'_i \partial u'_j}}{\partial x_k \partial x_k} = 2 \frac{\delta_{ij}}{3} \frac{q^3}{\Lambda_1} \quad (2.40)$$

With similar arguments as for defining the Eq. 2.40, the dissipation of the heat flux is written as:

$$2\alpha \frac{\overline{\partial \theta' \partial \theta'}}{\partial x_k \partial x_k} = 2 \frac{q}{\Lambda_2} \overline{\theta'^2} \quad (2.41)$$

In Eqs. 2.40-2.41, Λ_1 and Λ_2 are the typical dissipation length scale and must be obtained from measurements.

The third order variances of anomalies are parametrised as a downgradient diffusion of the second order terms, where the efficiency of the diffused flux is proportional to the square root of the TKE and the diffusional length scale (λ_1 , λ_2 and λ_3). Taking into account the symmetries the following equations are derived:

$$\overline{u'_i u'_j u'_k} = -q \lambda_1 \left(\frac{\overline{\partial u'_i u'_j}}{\partial x_k} + \frac{\overline{\partial u'_j u'_k}}{\partial x_i} + \frac{\overline{\partial u'_k u'_i}}{\partial x_j} \right) \quad (2.42)$$

$$\overline{u'_i u'_j \theta'} = -q \lambda_2 \left(\frac{\overline{\partial \theta' u'_i}}{\partial x_j} + \frac{\overline{\partial \theta' u'_j}}{\partial x_i} \right) \quad (2.43)$$

$$\overline{u'_i \theta'^2} = -q \lambda_3 \frac{\overline{\partial \theta'^2}}{\partial x_i} \quad (2.44)$$

An important assumption of the model is that all length scales are proportional to each other everywhere in the boundary layer. Therefore, the master length scale l can be defined which controls all of the aforementioned length scales:

$$\begin{bmatrix} l_1 \\ l_2 \\ \lambda_1 \\ \lambda_2 \\ \lambda_3 \\ \Lambda_1 \\ \Lambda_2 \end{bmatrix} = \begin{bmatrix} A_1 \\ A_2 \\ S_q \\ S_{u\theta} \\ S_\theta \\ B_1 \\ B_2 \end{bmatrix} l \quad (2.45)$$

Constants written in the vector on right hand side of Eq. 2.45 are purely empirical and must be obtained from measurements. The assumption of the single length scale controlling all length scales has been questioned by many authors (e.g. Lenderik and Holtslag, 2004), where they proposed to distinguish between the length scale defining the dissipation (Λ_1 and Λ_2) and diffusion (λ_1 , λ_2 and λ_3). In the work presented here it is assumed, that only one master length scale controls all length scales.

Mellor-Yamada-Janjić boundary layer model in WRF

In Mellor-Yamada model, six new independent prognostic equations for the momentum flux (Eq. 2.34), three for the heat flux (Eq. 2.35) and one for the covariance of the potential temperature anomalies (Eq. 2.36) must be solved in the mesoscale model in addition to the original set of equations for the mean flow. The ten new prognostic equations would significantly increase the computational burden of the mesoscale model. Therefore, for practical reasons those equations must be further simplified. Mellor and Yamada (1974, 1982) realized that momentum flux equations can be written as a sum of the isotropic part (representing the energy containing part) and the anisotropic. They defined the measure of anisotropy a_{ij} as:

$$\overline{u'_i u'_j} = \left(\frac{\delta_{ij}}{3} + a_{ij} \right) q^2 \quad (2.46)$$

Similarly anisotropy measure (b_i) can also be defined for the heat flux:

$$\overline{u'_i \theta} = b_i q \sqrt{\theta'^2} \quad (2.47)$$

Mellor and Yamada (1974, 1982) simplified Eqs. 2.34-2.36 with above defined closure assumptions by neglecting the terms proportional to the high orders of a_{ij} and b_i . They derived different level of models, with respect to the level of the anisotropy they retain. In this work, we used the so called level 2.5 model, where the model consist of the prognostic equation for TKE and two algebraic equations relating the nondimensional wind and potential temperature gradients with the nondimensional mixing coefficients. The simplifications of the original equations to the level 2.5 is in detail described by Mellor and Yamada (1974, 1982) and the equations of the model are written in appendix of Ch. 5. The level 2.5 model is very popular, since it is computationally cheap while it relatively well simulates the boundary layer.

Janjić (2002) applied the Mellor-Yamada parametrisation to the WRF mesoscale models. He solved the well known problem of numerical instability of the Mellor-Yamada model in the growing turbulence which arise due to neglecting the high order anisotropy terms Helfand and Labraga (1988) by imposing upper limit to the master length scale. Therefore, the parametrisation scheme in WRF is called Mellor-Yamada-Janjić scheme.

Mellor-Yamada-Janjić surface layer model in WRF

In the surface layer, which is defined from the ground to the first model level, and represents the lower boundary condition for the boundary layer, the Mellor-Yamada level 2.5 model cannot be used. The equations of the level 2.5 model are further simplified to the so called level 2, by assuming the local balance between the production and the dissipation of the TKE. The equations of the model are given in appendix of Ch. 5.

Surface layer parametrisation in WRF model is defined based on the Monin-Obukhov (MO) scaling theory (Eqs. 2.30 and 2.32). Łobocki (1993) showed that Mellor-Yamada level 2 model is consistent with the (MO) theory, if the stability corrections are defined properly. In Ch. 5, we derived the stability corrections for the MO profiles to be consistent with the Mellor-Yamada-Janjić level 2 model.

Master length definitions

The main problem of Mellor-Yamada models remains the specification of the master length scale. Mellor and Yamada (1982) realized that the definition of the proper master length scale is a crucial part for of the boundary layer model to properly predict its behaviour. Unfortunately, the solid physical definition of the master length scale does not exist and there is no physical equation for it. In the original version of the Mellor-Yamada models, they propose two limiting values for the master length scale.

Close to the surface, the height above the ground is the relevant macroscopic length scale since it limits the size of the turbulent eddies. Following the work of Prandtl (1925), the surface length scale is defined as:

$$l_1 = kz \tag{2.48}$$

Where k is von Karman constant ($k \approx 0.4$) and z height above the ground.

Far away above the ground, the limiting value based on the bulk property of the turbulence in the boundary layer is calculated as a ratio between the first and zero momentum of square root of TKE:

$$l_2 = \alpha \frac{\int_0^\infty z q dz}{\int_0^\infty q dz} \tag{2.49}$$

The total length scale is defined in a way that the shortest of the length scales have the most influence on it as:

$$\frac{1}{l} = \frac{1}{l_1} + \frac{1}{l_2} \tag{2.50}$$

In Ch. 5, we adjusted the definition of the master length scale where we discuss and describe the changes.

Bibliography

- Alexandersson, H., H. Tuomenvirta, and T. Schmith, 2000: Trends of storms in NW Europe derived from an updated pressure data set. *Climate R.*, **14**, 71–73.
- Buizza, R., M. Miller, and T. N. Palmer, 1999: Stochastic representation of model uncertainties in the ECMWF ensemble prediction system. *Q. J. R. Meteorol. Soc.*, **125**, 2887–2908.
- Cheng, Y., V. M. Canuto, and A. M. Howard, 2002: An improved model for the turbulent PBL. *J. Atmos. Sci.*, **59** (9).
- Corti, S., F. Molteni, and T. N. Palmer, 1999: Signatures of recent climate change in the frequencies of natural atmospheric variability. *Nature*, **398** (799-802).
- Cuxart, J., et al., 2006: Single-column model intercomparison for a stably stratified atmospheric boundary layer. *Boundary-Layer Meteorol.*, **118** (2), 273–303.
- Davidson, P. A., 2006: *Turbulence: An introduction for scientists and engineers*. Oxford University Press.
- Drews, A., et al., 2008: Network of offshore wind farms connected by gas insulated transmission lines? *Proceedings of EWEC conference*.
- Hannachi, A., 2007: Pattern hunting in climate: A new method for finding trends in gridded climate data. *Int. J. Climatol.*, **27**, 1–15.
- Hannachi, A., I. T. Jolliffe, and B. Stephenson, 2007: Empirical orthogonal function and related techniques in atmospheric science: A review. *Int. J. Climatol.*, **27**, 1119–1152.
- Helfand, H. and J. Labraga, 1988: Design of a nonsingular level 2.5 second-order closure model for the prediction of atmospheric turbulence. *J. Atmos. Sci.*, **45** (2), 1131–1132.
- Hurrell, J. W., Y. Kushnir, G. Ottersen, and M. Visbeck, 2003: An overview of the North Atlantic Oscillation. *The North Atlantic Oscillation: Climatic Significance and Environmental Impacts*, American Geophysical Union, Geophysical Monographs, Vol. 134.
- Hurrell, J. W. and H. van Loon, 1997: Decadal variations in climate associated with the North Atlantic oscillation. *Climate Change*, **36**, 301–326.
- Janjić, Z. I., 2002: Nonsingular implementation of the Mellor-Yamada level 2.5 scheme in the NCEP meso model. Tech. Rep. 436, NCEP Office Note.
- Kalnay, E., et al., 1996: The NCEP/NCAR 40-year Reanalysis Project. *Bull. Am. Meteorol. Soc.*, **77** (3), 437–471.
- Kistler, R., et al., 2001: The NCEP-NCAR 50-year reanalysis: Monthly means CD-Rom and documentation. *Bull. Am. Meteorol. Soc.*, **82** (2), 247–268.
- Lenderik, G. and A. A. M. Holtslag, 2004: An updated length-scale formulation for turbulent mixing in clear and cloudy boundary layers. *Q. J. R. Meteorol. Soc.*, **130**, 3405–3427.
- Lobocki, L., 1993: A procedure for the derivation of surface-layer bulk relationships from simplified second-order closure models. *J. Appl. Meteorol.*, **32** (1).

BIBLIOGRAPHY

- Louis, J., 1979: A parametric model of vertical eddy fluxes in the atmosphere. *Boundary-Layer Meteorol.*, **17** (17), 187–202.
- Mellor, G. L., 1973: Analytic prediction of the properties of stratified planetary surface layers. *J. Atmos. Sci.*, **30**, 1061–1069.
- Mellor, G. L. and T. Yamada, 1974: A hierarchy of turbulence closure models for planetary boundary layers. *J. Atmos. Sci.*, **31**, 1791–1806.
- Mellor, G. L. and T. Yamada, 1982: Development of a turbulence closure model for geophysical fluid problems. *Rev. Geophys. Space Phys.*, **20**, 851–875.
- Monahan, A. H., 2000: Nonlinear principal component analysis by neural networks: Theory and application to the Lorenz system. *J. Climate*, **13**, 821835.
- Nakicenovic, N., (Ed.) , 2000: *Special Report on Emissions Scenarios (SRES)*. Cambridge University Press.
- Palmer, T., G. Shutts, R. Hagedorn, F. J. Doblas-Reyes, T. Jung, and M. Leutbecher, 2005: Representing model uncertainty in weather and climate predictions. *Annu. Rev. Earth Planet. Sci.*, **33** (163-193).
- Palmer, T. N., 2001: A nonlinear perspective on model error: A proposal for non-local stochastic-dynamic parametrization in weather and climate prediction model. *Q. J. R. Meteorol. Soc.*, **127**, 279–304.
- Pielke, R. A., 2002: *Mesoscale Meteorological Modelling*, International Geophysics Series, Vol. 78. Academic Press.
- Pleim, J. E., 2007: A combined local and non-local closure model for the atmospheric boundary layer. part 1: Model description and testing. *J. Appl Meteorol. Climatol.*, **46**, 1383–1395.
- Prandtl, L., 1925: Bericht über Untersuchungen zur ausgebildeten Turbulenz. *ZAMM-Z. Angew. Math. Me.*, **5**, 136–139.
- Preisendorfer, R. W., 1988: *Principal Component Analysis in Meteorology and Oceanography*. Developments in Atmospheric Science no. 17, Elsevier, Amsterdam.
- Rotta, J., 1951: Statistische theorie nichthomogener turbulenz. *Z. Phys.*, **129**, 547–572.
- Schwierz, C., C. Appenzeller, H. C. Davies, M. Linger, W. Müller, T. F. Stocker, and M. Yoshimori, 2006: Challenges posed by and approaches to study of seasonal-to-decadal climate variability. *Climate Change*, **79**, 31–63.
- Siebesma, A. P., P. M. M. Soares, and J. Teixeira, 2007: A combined eddy-diffusivity mass-flux approach for the convective boundary layer. *J. Atmos. Sci.*, **64**, 1230–1248.
- Skamarock, W. C., et al., 2008: A description of the advanced research WRF version 3. Tech. rep., NCAR technical note.
- Soares, P., P. M. A. Miranda, J. Teixeira, and A. P. Siebesma, 2007: An eddy-diffusivity/mass-flux boundary layer parametrization based on the TKE equation: a dry convection case study. *Fisica de la Tierra*, **19**, 147–161.

- Stuhl, R. B., 1988: *An Introduction to Boundary Layer Meteorology*. Kluwer Academic Publishers.
- Teixeira, J. and S. Cheinet, 2004: A simple mixing length formulation for the eddy-diffusivity parametrization of dry convection. *Boundary-Layer Meteorol.*, **110**, 435–453.
- Teixeira, J. and C. Reynolds, 2008: Stochastic nature of physical parametrizations in ensemble prediction: A stochastic convection approach. *Mon. Weather Rev.*, **136**, 483–496.
- Treut, H., R. Somerville, U. Cubasch, Y. Ding, C. Mauritzen, A. Mokssit, T. Peterson, and M. Prather, 2007: *The Physical Science Basis. Contribution of Working Group I to the Fourth Assessment Report of the Intergovernmental Panel on Climate Change*, chap. Historical Review of Climate Change Science. Cambridge University Press.
- Trigo, R. M., T. J. Osborn, and J. M. Corte-Real, 2002: The North Atlantic Oscillation influence on Europe: Climate impacts and associated physical mechanisms. *Climate R.*, **20**, 9–17.
- Troen, I. B. and L. Mahrt, 1986: A simple model of the atmospheric boundary layer; Sensitivity to surface evaporation. *Boundary-Layer Meteorol.*, **37**, 129–148.
- von Storch, H. and F. W. Zwiers, 2003: *Statistical Analysis in Climate Research*. Cambridge University Press.
- Weisstein, E. W., 2009: Mathworld-a wolfram web resource, <http://mathworld.wolfram.com/>.

3

North Sea Near Surface Wind Climate and its Relation to the Large Scale Circulation Patterns[†]

Abstract

The North Sea 10 m wind speed (WS10) climate is compared and related to circulation patterns based on the Sea Level Pressure (SLP) extracted from three reanalysis and one high resolution model datasets. The mean magnitude and the trends of WS10 depend considerably on the selected reanalysis. The variability of WS10 among the three reanalysis datasets is highly correlated in the recent period (1980-2000), but less so in the past period (1960-1980). The WS10 over the North Sea is well represented by the relatively low reanalysis resolution when compared to the high resolution WS10 model data partially owing to the high spatial correlation of WS10. Exceptions are observed only at the coastal areas. The dominant mode of WS10 explains coherent variability of WS10 over the North Sea and is related to a SLP pattern similar to the North Atlantic Oscillation (NAO). The increase of the magnitude of the dominant WS10 pattern is related to the increase of the magnitude of the NAO like SLP pattern from 1960s to mid 1990s. The second dominant WS10 pattern - a dipole in WS10 to the north and south of Great Britain - is related to the differences in SLP between Scandinavia and Iceland. The relation between the second WS10 and SLP patterns is more prominent in the recent period. The extreme WS10 in the German Bight is related to the low SLP over Scandinavia. The extreme WS10 is strongly increasing from the early 1980s to the beginning of 1990s, which is not observed in the corresponding SLP time series over Scandinavia.

3.1 Introduction

The climatology of marine surface wind field is of considerable commercial interest, e.g. for harnessing wind energy at favourable offshore sites, for the shipping and for the offshore oil and gas industry. In view of a strong increase in the industrial exploitation of the North Sea, this study addresses some questions related to the climatology of the daily mean wind speed at 10 m height (WS10), namely i) whether there are important differences in the mean and extreme WS10 in different low resolution reanalysis datasets, especially related to their long term trends; ii) how well is WS10 represented in the low resolution global reanalysis dataset (horizontal resolution of roughly 100 km × 100 km) compared to the high resolution simulations (horizontal resolution of 3 km × 3 km), or alternatively are there important processes

[†]The work presented in this chapter is accepted for publication in Theoretical and Applied Climatology as: Kay Sušelj, Abha Sood, Detlev Heinemann: North Sea near surface wind climate and its relation to the large scale circulation patterns.

that remain unresolved at low resolution and are resolved in higher resolution simulations and whether there is a subsequent long term impact; iii) can the relationship between the monthly mean WS10 and the large scale circulation patterns over the European-Atlantic region and their inter-annual variability in the last few decades be quantified; and iv) can the extreme WS10 over the German Bight be related to extreme circulation patterns and do the long term trends of extreme WS10 and circulation patterns agree?

The WS10 from different reanalysis datasets can be used to study the near surface wind climatology and its relation to the circulation patterns. The reanalysis data have previously been widely used for climate studies since the data quality is mostly consistent over a number of decades, which is achieved by using the same model throughout the reanalysis period (Kalnay et al., 1996). However, with the development of the observation system, the quality of reanalysis data has improved over the last two decades. The most pronounced change affecting WS10 is probably the assimilation of the satellite measured near surface wind speeds which started in the late 1970s (Kistler et al., 2001). This can lead to discontinuities in the WS10 time series and artificial trends. It was confirmed that some basic parameters, such as the SLP from different reanalysis generally agree well over Europe (e.g. Greatbatch and Rong, 2006), which increases confidence in using the reanalysis data. The WS10 from reanalysis may be sensitive to the model details, such as the selected surface and boundary layer parametrizations (Kalnay et al., 1996). As far as we are aware, there has been no systematic comparison of the WS10 from different reanalysis over northern Europe.

Most studies concerned with the wind climatology over northern Europe use low resolution wind speed or a proxy dataset (e.g. derived from the horizontal pressure gradients). For example, Pryor and Barthelmie (2003), Pryor et al. (2006) and Yan et al. (2006) use reanalysis data to infer the climatology of near surface mean and extreme winds over northern Europe, their inter-decadal variability and linear trends. Weisse et al. (2005) investigated the changes of cyclone intensity and frequency over the North Atlantic and the North Sea from the downscaled NCEP reanalysis data of around 50 km horizontal grid size. Studying extreme winds, some authors prefer to use proxy data, such as the mean sea level pressure (SLP) or geostrophic wind speed inferred from the SLP gradients, arguing that the SLP data is less prone to systematic errors which may lead to artificial trends (e.g. Schmidt and von Storch, 1993; Alexandersson et al., 2000; Matulla et al., 2007). The proxy data derived from SLP is usually able to capture the large scale forcing on the wind field, but not the local effects. The ability of the low resolution wind speed datasets or the proxy data to represent realistic surface wind conditions over the North Sea remains unclear. The largest differences between low and high resolution wind speed are expected close to the coastline or orographic features, where the wind speed may deviate due to strong gradients in forcing and formation of local circulation patterns or in case of strong horizontal gradients (e.g. fronts).

The influence of the North Atlantic Oscillation (NAO), which is described by the anomaly of pressure gradient between north-western (usually Iceland) and south-western North Atlantic (usually Azores), on the wind speed over northern Europe is well documented (e.g. Marshall et al., 2001; Hurrell and van Loon, 1997; Trigo et al., 2002). The NAO index (NAOI) is well correlated with the wind speed over northern Europe, especially in the winter season where the large scale circulation has a more dominant influence on the weather. In the summer season, the surface heating produces disturbances weakening the large scale circulation. An increase of the NAOI from the 1960s to the mid 1990s was observed. It is known that the increase in NAOI leads to higher wind speeds over northern Europe (e.g. Hurrell and van Loon, 1997). Here we investigate, whether a regional spatial pattern of SLP exists, which has a more

dominant influence on the WS10 variability over northern Europe than the NAO. It is also not clear if there are other patterns, which are able to describe an additional fraction of WS10 variability. For example, Barnston and Livezey (1987) have observed that the second dominant mode of the North Atlantic pressure variability is the East Atlantic (EA) pattern, which can explain a considerable part of the wind speed variability in northern Europe. Kaas et al. (1996) found that a pressure structure similar to the NAO, is related to the wind speed in northern Europe, although the northern centre of their pattern is more elongated and shifted eastwards. Rogers (1997) identified a pattern similar to the one from Kaas et al. (1996) and observed that it was related to the position of the storm tracks. Another alternative is to relate the surface wind speeds to other large scale fields such as the surface temperature. The study by Deser and Blackmon (1993) suggests that the Sea Surface Temperature (SST) is well correlated with the wind speed. However they found that the relationship is local and suggest that the surface wind influences the SST by mixing the upper ocean waters.

High resolution simulations can resolve a number of physical processes such as the land-sea breeze in the coastal areas which is additional information not obtained by statistical downscaling of low resolution reanalysis data. The climate signature of these processes may be vital for some applications such as for wind energy resource studies. The long term fluctuations and trends extracted from the reanalysis can be combined with the detailed regional information from high resolution simulations. This information is vital for risk management, resource assessment and long term planning to compensate for the inherent fluctuations of the climate system in the development of renewable energy resources and by other stakeholders. Here we use three year data from a mesoscale model (WRF) simulation with 3 km resolution to determine the significance of key regional physical processes.

As opposed to the well studied variability of the mean wind speed over northern Europe, the variability of extreme winds over the past few decades is less known. On one hand, with an increase in the NAOI and the mean wind speed from the 1960s to the mid 1990s, the extreme wind speeds are expected to rise. On the other hand, there are studies that show a trend in shifting of the North Atlantic storm track northwards in the past decades, which causes a trend of decreasing storms in the southern part of northern Europe (e.g. Schneidereit et al., 2005; Wang et al., 2006). The extreme winds can be characterized by different criteria, such as the occurrence of wind speeds exceeding a threshold (e.g. Weisse et al., 2005) or wind speeds at certain high percentiles, such as for example the 90 percentile (e.g. Pryor and Barthelmie, 2003; Matulla et al., 2007). With the first approach, the number of storm events exceeding a predefined threshold level is investigated, while with the second approach, the intensity of storms is studied. Different and sometimes contradictory results regarding the trends of the extreme winds or storms have been presented. Based on the SLP measurements, Schmidt and von Storch (1993) found no increase and very little inter-annual variability of the high wind speed percentiles over the last century in the German Bight. From the SLP analysis, Matulla et al. (2007) concluded that the extreme wind speeds in the north-eastern Atlantic region were high in the late 19th and the beginning of the 20th century, lower in the middle of the 20th century and then at the end of the 20th century reach a similar level as at the beginning of the 20th century. Their analysis is focused on the wind speed north and east of the North Sea. Pryor and Barthelmie (2003) observed an increase in the high wind speed in the last few decades over the Baltic Sea and parts of the North Sea derived from the NCEP (NCR) reanalysis. An increase in the extreme wind speeds over the Baltic is related to an increase in the frequency of the western types of Grosswetterlagen in the last quarter compared to the middle of the 20th century. The extreme weather conditions

are usually not well linked to the large scale circulation patterns such as the NAO, since the NAO explains well the variability on monthly to inter-decadal time scales, while the extreme values by definition occur only for short periods. Therefore, some authors link the extreme values to different circulation patterns (Yiou and Nogaj, 2004; Panja and Selten, 2007).

The paper is structured as follows. The data are described in Section 3.2. In Section 3.3, the WS10s over the North Sea from different reanalysis datasets are compared to each other and to the high resolution WS10. The relation of the mean WS10 to the circulation patterns and their time evolution and the relation of the extreme WS10 to the extreme circulation patterns are then derived. Finally the discussions and conclusions are presented in Section 3.4.

3.2 Data Description

The present study uses the daily sea level pressure (SLP), 2 m temperature (T2M), wind speed at 10 m height (WS10) and wind speed at 700 hPa level (WS700hPa) from three reanalysis datasets - NCEP/NCAR (therefore, **NCR**) (Kalnay et al., 1996; Kistler et al., 2001), NCEP-DOE (**NCR2**) (Kanamitsu et al., 2002) which is an updated version of the NCR reanalysis and ECMWF ERA40 (**ERA40**) (Uppala et al., 2005). The NCR and NCR2 reanalyses are based on the same model with a global T62 horizontal grid and 28 vertical sigma levels. In NCR2, errors found in NCR were corrected; additional data were assimilated as well as some of the physical parametrizations were changed. For the present analysis, the most relevant modification is the change of a simple boundary layer parametrization based on the local Richardson number in NCR to a non-local diffusion scheme in NCR2 (Kanamitsu et al., 2002). The ERA40 model is defined on the global T159 grid with 60 hybrid vertical levels.

In addition, the higher resolution (3 km grid size) but shorter (3 years) WS10 data was obtained by integrating the Weather Research and Forecasting (WRF) (Skamarock et al., 2005) model (Sood et al., 2007). The duration of the short time series of high resolution data is not adequate to derive climate variability characteristics of WS10. Rather, it was used to investigate how well daily WS10 over the North Sea is represented in the low resolution reanalysis dataset, and to detect additional high resolution information. WRF was initialized at 18 UTC every second day with a spin up time of 6 hours and a forecast horizon of 53 hours. A continuous 4-times daily time series is constructed by combining the 6 hourly data from 6th – 53rd forecast hours. The initial and boundary conditions are prescribed from the NCEP Final Analysis (FNL). Three (two-way) nested domains are defined in WRF, where the third domain with a horizontal resolution of 3 km spans the innermost region (lat. 52.5N–55.25N, lon. 4.75E–9.5E). The WRF model includes parametrizations of all essential physical processes. The surface and the boundary layer parametrizations were based on the Mellor-Yamada-Janji model (Janjić, 2002). Here only WS10 from the third WRF domain (WRF3) was analysed.

To relate the dominant WS10 patterns to the main modes of atmospheric variability, the North Atlantic Oscillation Index (NAOI) and the East Atlantic Index (EAI) from the Climate Prediction Centre (CPC) were used. These indices were constructed based on the Rotated Principal Components analysis of the northern hemispheric 500 hPa geopotential height. In addition, the corrected and pre-processed measurements of SLP from the stations at Göteborg (Sweden) and Oksoy (Norway), which were a part of the European project EMULATE (European and northern Atlantic daily to multi-decadal climate variability) (Ansell et al., 2006), were used to relate the extreme WS10 to the circulation indices.

3.2. DATA DESCRIPTION

Dataset	Resolution (lat. × lon.)	Time period	Parameters
NCR	2.5° × 2.5° ^a 1.85° × 1.9° ^b	Jan.1948 - Dec.2007	WS10 WS700hPa SLP T2M
NCR2	2.5° × 2.5° ^a 1.85° × 1.9° ^b	Jan.1979 - Dec.2007	WS10 WS700hPa SLP T2M
ERA40	2.5° × 2.5°	Sept.1957 - Aug.2002	WS10 WS700hPa SLP T2M
WRF3	3km×3km	Jan.2004 - Dec.2006	WS10
NAOI, EAI ^c	-	Jan.1950 - Dec.2006	-
SLP measurements ^d	-	Jan. 1948 - Dec. 2002	SLP

^a Resolution for SLP and T2M

^b Resolution for WS10

^c Data derived from geopotential height at 500 hPa

^d From stations Göteborg and Oksoy

Table 3.1: Dataset used for this study (for abbreviation look in text), the horizontal resolution, time period and parameters.

All datasets used in this study are shown in Tab. 3.1, where the time period, the horizontal resolution and the parameters used (where applicable) are listed.

The focus of the WS10 analysis is mainly over the North Sea region (**NS**) (lat. 50N–60N, lon. 3W–20E), though for relating the WS10 patterns to the large scale patterns, a larger North Sea region (**INS**) is defined (lat. 45N–65N, lon. 15W–30E). For the case where only WS10 patterns were investigated, the North European (**NE**) region is additionally used (lat. 40N–70N, lon. 20W–30E). The SLP and T2M data, used as predictors of WS10 are defined on the Atlantic-European (**AE**) domain (lat. 30N–90N, lon. 80W–40E). The extreme WS10 were studied over the German Bight (lat. 52.5N–55.5N, lon. 4.7E–9.5E).

The analysis is based on the daily mean values defined as an average of the four times daily data (00 UTC, 06 UTC, 12 UTC and 18 UTC). In case of WS10, the magnitude of WS10 was calculated from the wind speed components (U10 and V10) from 6-hourly data and averaged over the day.

A part of the analysis is performed on the anomalies from the annual cycle. The anomalies were computed for each grid point of the data field separately. First, the monthly average value is computed as an average value at each grid point within a calendar month. The mean annual cycle was constructed by assuming that the monthly average corresponds to the 15th day of the calendar month, while the daily values of mean annual cycle are calculated as a linear interpolation of the values at the 15th day. The anomalies, i.e. deviations from the mean annual cycle, are obtained as a difference between the original field and the mean annual cycle. Part of the analysis is performed for the winter (December–February) and the summer (June–August) seasons separately. Two periods of 21 years were defined, the past pre-satellite period (1960–1980) and the recent period (1980–2000) where the satellite data (in particular, the marine surface wind) is assimilated in the reanalysis.

3.3 Analysis Methods and Results

The surface wind conditions over North Sea derived from the datasets described in Section 3.2 are investigated for a range of temporal and spatial scales to detect resolution dependent characteristics and to test the robustness of consequent assertions. The modes of wind speed variability over the North Sea are examined and related to the large scale circulation patterns to identify and analyse relevant indicators of regional climate trend. The time evolution of the extreme wind speed and its relation to the circulation patterns is studied.

3.3.1 Description of surface wind speed in different data-sets

To estimate the reliability of reanalysed daily wind speed in terms of mean values and trends, the surface wind speed (WS10) and the wind speed at 700 hPa level (WS700hPa) from different reanalyses are compared. Since all reanalyses are based on virtually the same measurement data, the wind speed especially close to the surface (WS10) may have similar problems such as the artificial trends and discontinuities due to advances in the observation system (such as the assimilation of near-surface satellite measurements). In order to assess the representation of WS10 by the low resolution data, it was interpolated and compared to the high resolution data.

In the recent period, the pattern of the mean WS10 across the NS domain is mainly influenced by the land-sea interface, with the highest WS10 values over seas reaching a maximum between around 8 m s^{-1} and 10 m s^{-1} (depending on a reanalysis model) and the lowest values over land between around 3 m s^{-1} to 6 m s^{-1} in the south-eastern part of the NS domain (Fig. 3.1, upper panel). The mean WS10 from NCR and ERA40 agree well over the studied area, while the mean WS10 from NCR2 is around 2 m s^{-1} higher. The difference between the mean WS10 from NCR and NCR2 is strikingly high even though both the reanalysis are based on the same model core and assimilation setup. The possible reasons for the differences are different atmospheric boundary and surface layer parameterization or the description of the land surface used in NCR and NCR2 models. Comparing the mean WS700hPa from the reanalysis models, which is used as a measure of the wind speed at the top of the boundary layer or in the free atmosphere and represents the upper kinematic forcing on the boundary layer, between all models (lower panel of Fig. 3.1) reveals small difference (less than 0.5 m s^{-1}) which indicates that the differences in mean WS10 between the models are primarily due to different representations of the boundary or land surface processes in the reanalysis models.

The variability of WS10, characterized by the standard deviation of daily mean WS10 time series of roughly half its mean value, varies very little across the domain (not shown). Significant fraction of the WS10 variability is due to the mean annual cycle, which is considered by examining the probability density distribution of the wind speed $P(\text{WS10})$ and the wind direction $P(\theta)$ averaged over the NS domain for the recent period (Fig. 3.2). The data plotted in Fig. 3.2 is binned on monthly resolution to present the intra-annual variability. The magnitude of spatially averaged WS10 is sensitive to the domain definition and the reanalysis data used, while the time evolution of the mean annual cycle of WS10 and the wind direction are relatively insensitive. The strongest winds are observed in the winter months (November – February), when the storm activity over the northern Europe is peaking. During this period, the wind direction is mostly from west to south-west ($200^\circ - 270^\circ$). In the spring season (March – June), the mean wind speeds decrease with the weakening of the storm activity over northern Europe. The wind directions remain predominantly from west

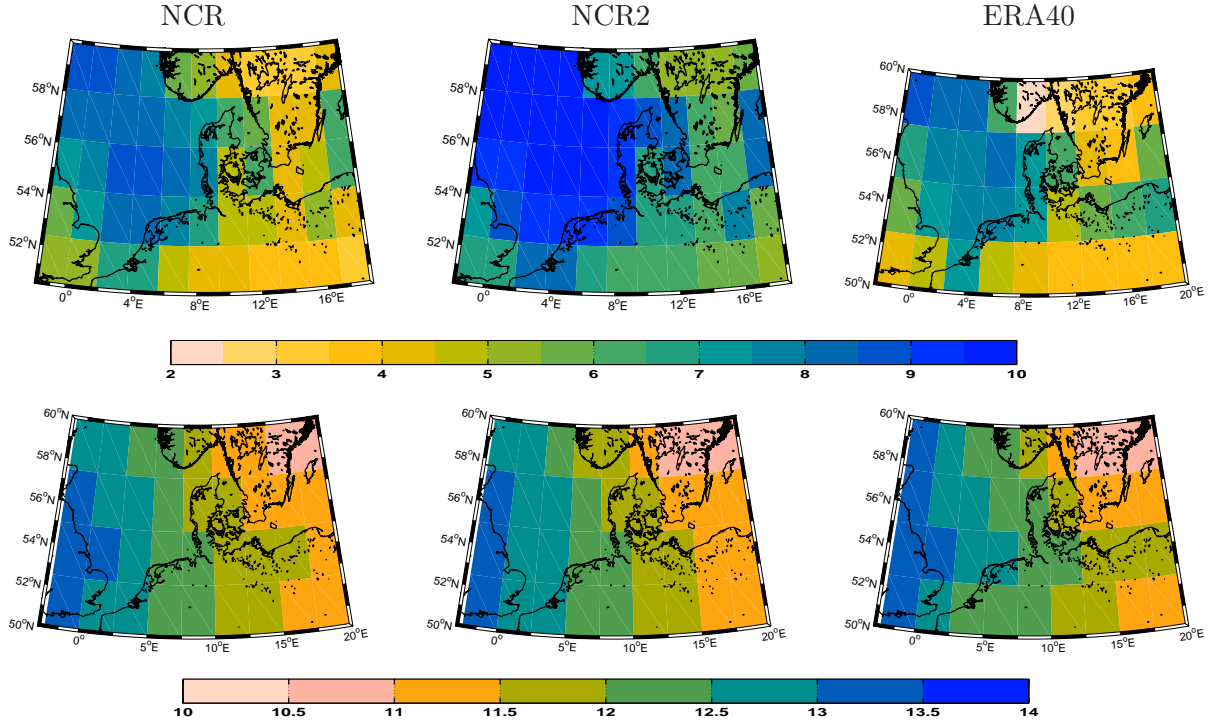


Figure 3.1: Mean WS10 [m s^{-1}] (upper panel) and WS700hPa [m s^{-1}] (lower panel) in the recent period (1980-2000) over NS domain from NCR, NCR2 and ERA40 reanalysis.

to south-west, but other directions are also observed. The weakening of the storm activity allows for more frequent outbreaks in this region especially from the north and north-east. Approaching summer, the wind speeds decrease further reaching the minimum in late summer and then increasing again from August onwards.

The temporal variability of WS10 between the datasets agrees well. The linear correlation coefficient between the time series of daily WS10 from NCR and ERA40 (bi-linearly interpolated on the NCR grid points) is high, reaching the values between 0.9 to 0.95 everywhere within the NS domain, except in the southern part of Scandinavia where the values are as low as 0.8 (not shown). The reason for the lower correlation coefficient above Scandinavia may be the different model resolutions which also lead to different representations of terrain. Since the NCR and NCR2 models are based on the same underlying orography, the correlation coefficient between WS10 from those two reanalysis is above 0.95 over the NS domain.

Even though WS10s from different reanalyses are well correlated, the linear trends differ substantially. In Fig. 3.3, the linear trends in the annual averaged WS10 data calculated for each grid-point separately and significant at the 5% level are plotted. To estimate the statistical significance of the WS10 trends, Student t -test was used with an adjusted number of degrees of freedom to account for serial autocorrelation in the data. The effective sample size is calculated as:

$$n_e = n_t \frac{1 - r_1}{1 + r_1} \quad (3.1)$$

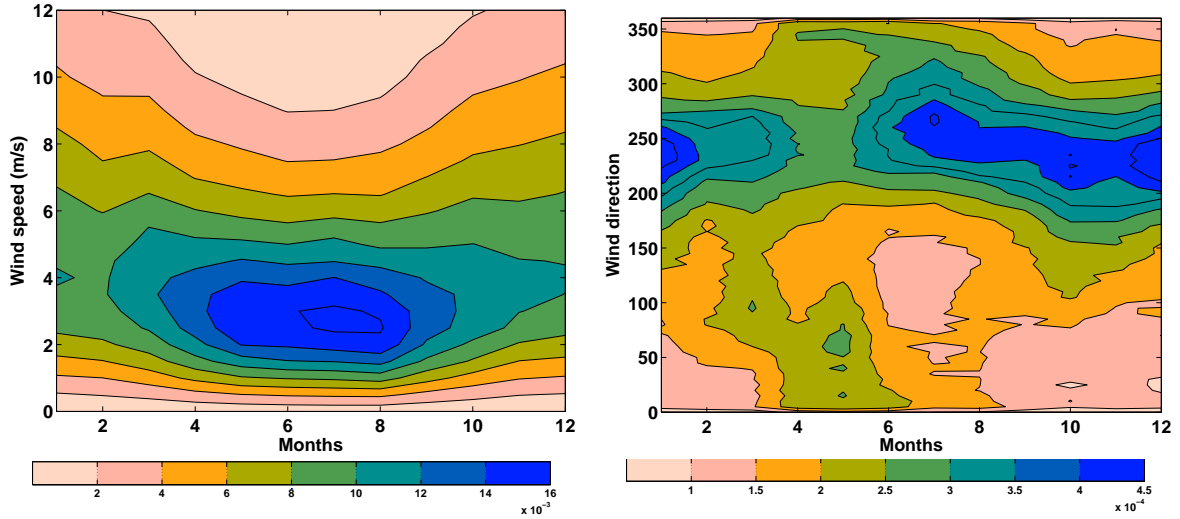


Figure 3.2: Probability density distributions of WS10 $[(\text{m s}^{-1})^{-1}]$ (left) and wind direction $[\text{deg}^{-1}]$ (right) for the annual cycle from the NCR averaged over NS domain in the recent period (1980-2000).

where n_t is the number of sample members, n_e the effective sample size and r_1 the lag one correlation of the regression residuals. The effective data size was used to correct the estimation of variance of residuals above the regression line and the number of degrees of freedom in the Student t -test. Further details can be found in Santer et al. (2000). In the past period, ERA40 data show a high positive trend of WS10 over the North Sea, while the trend in NCR is lower and seems to be centred in the north-western part of the domain and over the coastal areas (Fig. 3.3, upper panel). In the recent period, the trend from the three reanalysis models are positive everywhere, but quite different (Fig. 3.3, lower panel). The WS10 trend from NCR data is the lowest and concentrated over the south-western part of the domain. In the ERA40 data, the trend is mainly over northern Germany whereas in the NCR2 data it is over the south-western part of the domain including the North Sea. The linear trends in the WS700hPa well agree among all reanalysis models and are positive and significant over the northern part of the domain. As with the mean daily WS10, the different trends in WS10 reanalysis data appear mainly as a result of different representations of surface and boundary layer processes in the reanalysis models. The WS10 trends in the different datasets differ substantially while the correlation coefficients of WS10 are high. This seems contradictory, but understood since the linear trends explain only a small proportion of the WS10 variance.

The question addressed next is whether it is possible to represent the daily mean WS10 over the North Sea by the low resolution datasets, such as the reanalysis data. This depends on the spatial scales of the governing physical processes responsible for the daily regional WS10 variability compared to the resolution of the reanalysis data. It is well known that WS10 over the North Sea is partly influenced by the North Atlantic storm activity with typical horizontal scales of a few hundred kilometres. It is not clear if there are other local circulation patterns that distinctly influence the daily WS10. To estimate the typical length

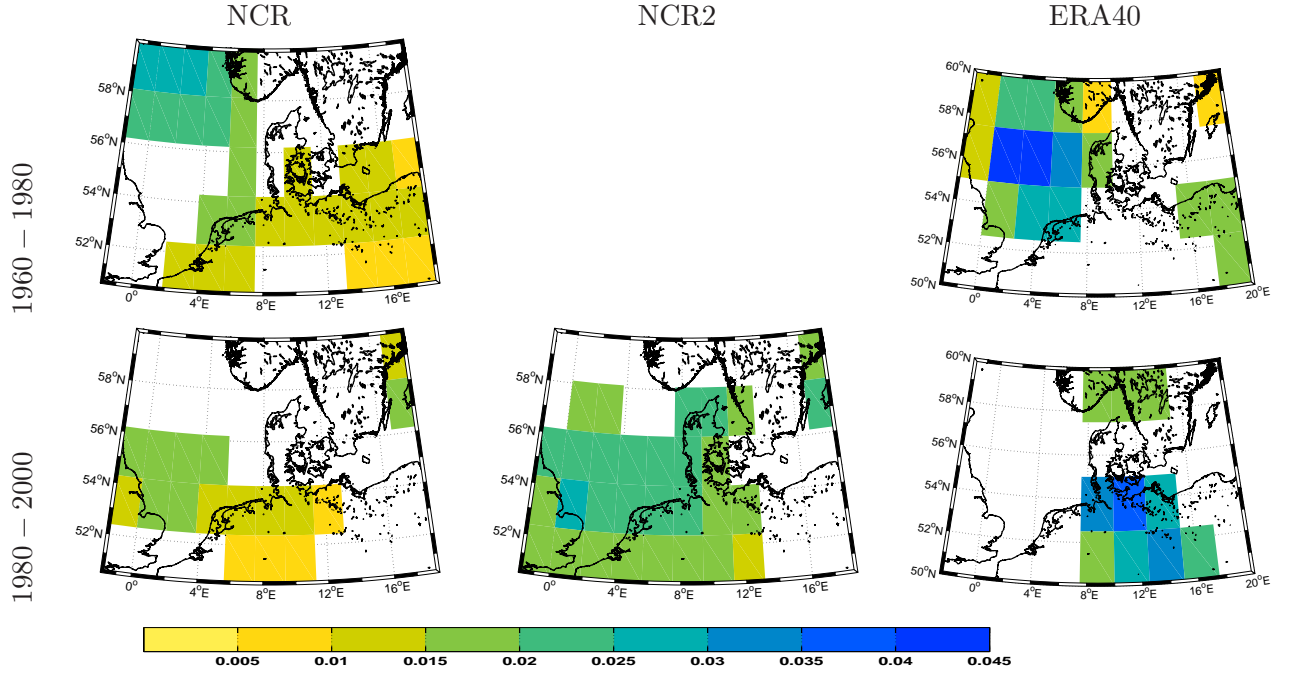


Figure 3.3: Linear trends in the annual averaged WS10 [$\text{m s}^{-1} \text{yr}^{-1}$] for the past (upper panel) and recent (lower panel) period. From left to right: NCR, NCR2 and ERA40. Only the trends significant on the 5% level (estimated by Student t-test) are plotted.

scale of WS10, the isotropic first order auto-regressive AR(1) model is fitted to the WS10 data. In the AR(1) model, the correlation coefficient between time series at locations r_i and r_j , separated by the distance $d(r_i, r_j)$ exponentially decrease (e.g. von Storch and Zwiers, 1999) and is not directionally dependent:

$$\text{corr}(r_i, r_j) = e^{-d(r_i, r_j)/d_0} \quad (3.2)$$

where the d_0 is the decorrelation length and is interpreted as the characteristic length at which points in space are no longer correlated. In the WRF3 data, the decorrelation length of the daily WS10 anomaly from the annual cycle is around 800 km over most of the domain and the North Sea, with smaller values over the southern and northern part of the domain as well as along the coastal regions (Fig. 3.4). The absolute value of the decorrelation length is not too reliable, since the horizontal domain of WRF3 is smaller than the decorrelation length. However, the result indicates that the daily WS10 variability over the North Sea can be well represented by the reanalysis models, since the decorrelation length of the daily WS10 is larger than the resolution of the reanalysis models. Exceptions are probably the regions along the North Sea coast especially in the Weser-Ems area, where the decorrelation length is lower probably due to the local circulation patterns. The spatial pattern may result from the local land-sea orientation with respect to the prevailing south-west to west winds. A smaller decorrelation length at the northern and southern parts of the domain may be related to a real signal and not an artefact of the boundary conditions while calculating the decorrelation

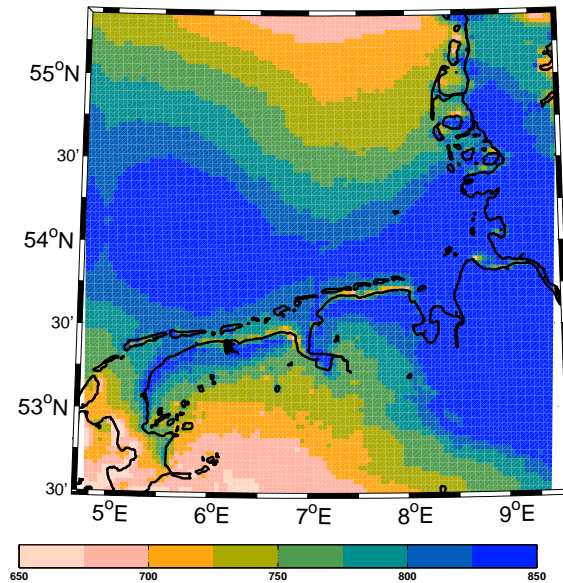


Figure 3.4: Decorrelation length (d_0) [km] for the WS10 anomaly from the annual cycle estimated from the WRF3 data.

length. The second Empirical Orthogonal Function of WS10 describes that the WS10 over these areas is negatively correlated (Section 3.3.2).

To quantify the relationship between WS10 from the low resolution reanalysis data (NCR) and the high resolution WRF3, WS10 from NCR was interpolated on the WRF3 grid and compared on the 3 years common time frame. To interpolate the WS10 data, two different techniques were used: i) bilinear interpolation of WS10 from NCR ignoring any information of the land-sea interface (we refer to this interpolation as BILIN); ii) separate bilinear interpolation for the WRF3 land and sea areas. At the interface, where the bilinear interpolation is not possible, the WS10 from the nearest point was taken (we refer to interpolation as BILIN-COAST). These simple interpolations do not take any specific knowledge of the atmospheric dynamics into account. As expected, the 3-years mean WS10 interpolated with BILIN-COAST show excessively high gradient of WS10 along the coasts, while the WS10 interpolated with BILIN method shows a too weak gradient at the coast compared to WS10 from WRF3 (Fig. 3.5). Therefore, it appears that at the coastal regions, high resolution WS10 adds additional information to the low resolution data related to the local circulation patterns. In the upper panel of Fig. 3.6, it is seen more clearly that in case of the BILIN interpolation, due to the too weak gradient of WS10 at the coast, WS10 is overestimated at the land points close to the coast and underestimated over the sea points at the coastal region, while with WS10 interpolated with the BILIN-COAST method with a sharp land-sea discontinuity, just the opposite is true. The correlation coefficient of WS10 from WRF3 and interpolated from NCR is high over the whole domain, with the lowest values at the coast of the Weser-Ems area and Holland. The lower correlation is probably due to the prevailing south-western wind which mixes the continental and oceanic air masses at the land-sea interface weakening the local circulation patterns at the windward side but retain some part towards the leeward side, which may leave an imprint on the long term daily WS10 variability.

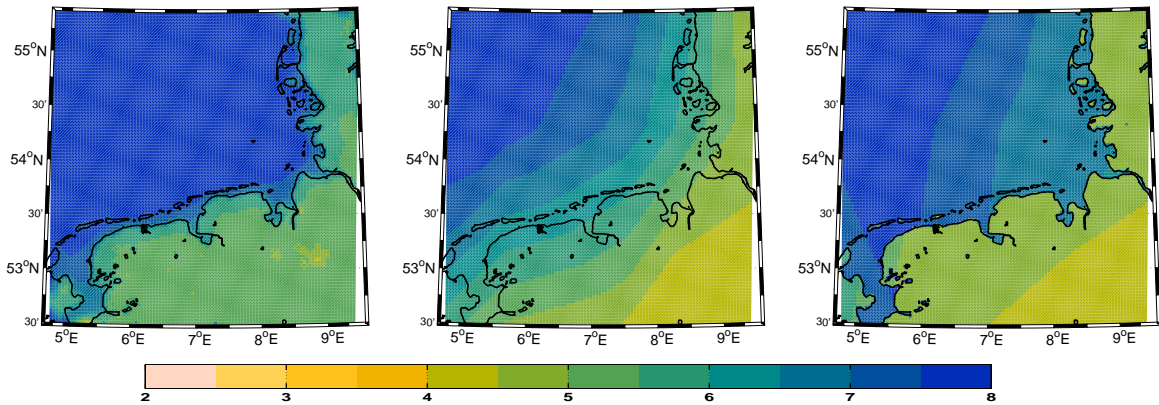


Figure 3.5: The three years averaged WS10 [m s^{-1}] from WRF (left), NCEP interpolated with BILIN (middle) and with BILIN-COAST (right) interpolation on the WRF3 grid.

3.3.2 Modes of Wind Speed Variability and their relation to the Large Scale Patterns

Since WS10 over the North Sea is spatially highly correlated, it is sufficient to characterize it by a few well chosen modes as for example with the Empirical Orthogonal Functions (EOFs). EOF analysis (e.g. Preisendorfer, 1988; von Storch and Zwiers, 1999) finds a linear combinations of modes comprising of the spatial patterns (Empirical Orthogonal Functions, EOFs) and their time evolutions (Principal Components, PCs), so that the modes explain the highest part of the variance of data under the orthogonality constrain of the EOFs. The resultant EOFs represent the spatial distribution of the magnitude of the field together with its relative phase, while the time series (PCs) are uncorrelated and explain the time evolution of the corresponding EOF. In this analysis, each pair of PC and EOF is normalized so that the variance of PC equals unity and the EOF represents the magnitude of typical variation of the field and thus the physical units of the field are attributed to the EOF. The EOF analysis is performed on the monthly mean WS10 anomalies from the mean annual cycle to account for the seasonality. Since only the monthly WS10 anomalies from the mean annual cycle are considered in this section, we simply refer to them as WS10. EOF modes of WS10, related SLP and T2M patterns from NCR dataset for the complete NCR period (1948-2007) are shown in first part of this section, while in the second part, the differences between NCR and other two reanalysis datasets in the recent (1980-2000) and the past (1960-1980) period are discussed.

The EOF modes of WS10 from NCR reanalysis are calculated on three domains (NS, INS and NE, as defined in the previous section) and compared to investigate the sensitivity of the modes on the domain size, where the measure of similarity is the correlation coefficients between the corresponding PCs (Tab. 3.2). While the first EOF mode is almost identical on all three domains, the second mode is very similar on only the two largest domains (INS and NE), while on the smallest domain it deviates considerably. The third (and also higher) EOF modes are sensitive to domain selection. In addition, the rotation of the EOFs have been performed with the VARIMAX method (e.g. Richman, 1986) using the first 5 or 10 EOF patterns. In both cases, the first rotated pattern was almost identical to the first non-

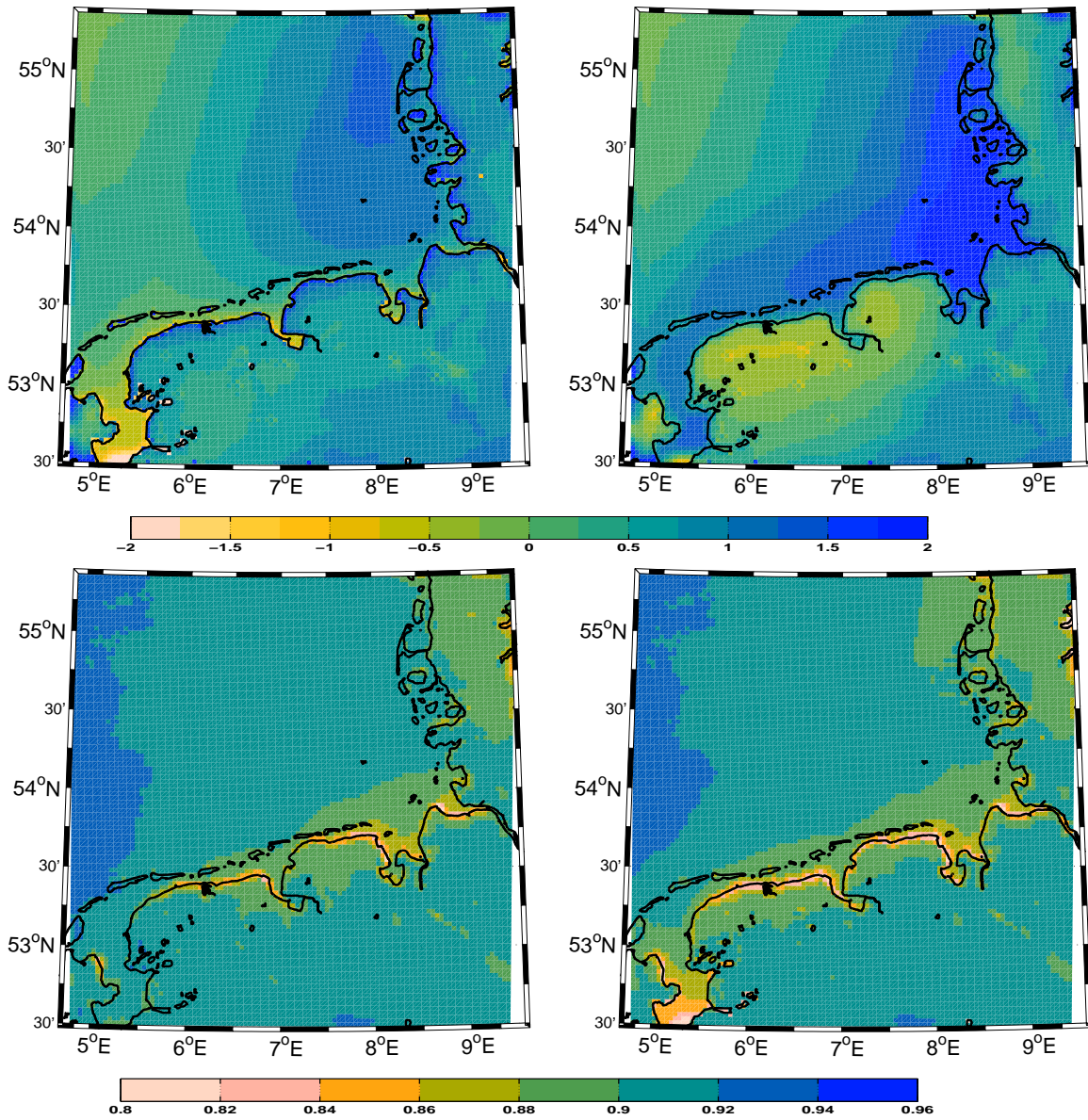


Figure 3.6: Mean difference (upper panel) and correlation coefficient (lower panel) between three years of WS10 [m s^{-1}] from WRF3 and NCEP interpolated on WRF3 grid. Left panel is for BILIN-COAST interpolation and right for BILIN interpolation (look in text for details).

3.3. ANALYSIS METHODS AND RESULTS

Mode	corr(NS,INS)	corr(INS,NE)
1	0.90	0.99
2	0.69	0.91
3	0.50	0.53
4	0.31	0.64

Table 3.2: Correlation coefficients for the first four PCs of monthly WS10 anomaly from NCR data for the time period 1948-2007 calculated over the NS and INS domain ($\text{corr}(\text{NS},\text{INS})$) and over the INS and NE domain ($\text{corr}(\text{NS},\text{INS})$).

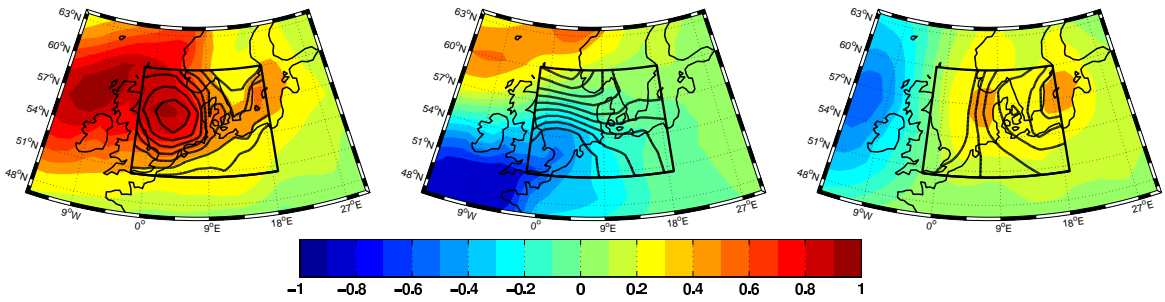


Figure 3.7: First three EOF patterns of monthly WS10 anomaly [m s^{-1}] for INS domain. EOF patterns for NS domain are also shown with the black contours.

rotated, while the second and third rotated patterns were mainly the linear combination of the second and the third non-rotated patterns (not shown). Since the rotated EOF modes do not seem to give additional information or better capture the relevant WS10 variability, only the non-rotated EOF modes are used in further analysis.

To investigate the relevance of the EOF modes of WS10, the explained variance of each mode is compared to the explained variance of the simple isotropic diffusive model modes projected on the EOF modes of WS10. The diffusive model is defined in Dommenges (2007) as AR(1) model in space and time:

$$\frac{d}{dt}\Phi = c_{damp}\Phi + c_{diff}\nabla^2\Phi + f \quad (3.3)$$

where the Φ is the synthetic field forced by the spatial and temporal white noise (f), the damping (c_{damp}) and diffusive (c_{diff}) coefficients are calculated from the WS10 data. As shown by Dommenges (2007), the comparison of the explained variance of the data modes and the ones from an AR(1) process projected on the data modes helps to separate the data modes which represent the spatial covariance of the data and modes which represent teleconnection patterns.

The first three EOFs of the monthly WS10 for the INS domain are plotted and the EOFs on the smaller NS domain are superimposed (Fig. 3.7). The explained variance of first five EOF modes of WS10 from the INS domain is shown in Fig. 3.8, where the confidence limits are obtained from the North's rule of thumb (North et al., 1982). The explained variance of the AR(1) process-modes projected on the EOF modes are also shown in this plot.

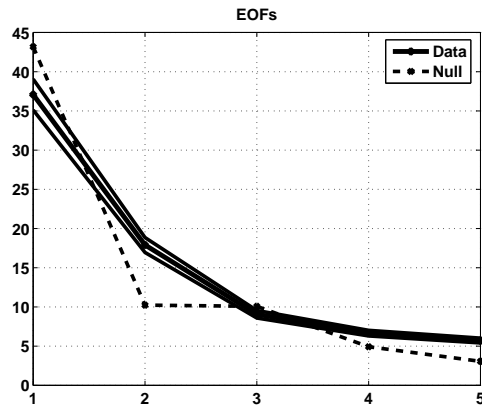


Figure 3.8: Explained variance [%] of the first five EOF modes of the WS10 anomaly with confidence interval (solid lines) and explained variance of the AR(1) modes projected on the data modes (dashed lines).

The first EOF mode of WS10, which explains around 38% of its variance is hardly separated from the stochastic AR(1) model, suggesting that this mode reflects that WS10 above the area studied is highly correlated in space (consistent with Fig. 3.4) and does not represent any specific teleconnection pattern. The higher magnitude of the WS10 in the first EOF above the sea is due to the higher variability of the WS10 over sea compared to land.

The second mode, which shows the negative correlation of WS10 above the North Atlantic north and south of Great Britain is statistically different from the AR(1) model. This mode explains around 18% of the WS10 variability, while the same mode will explain only around 10% of WSA10 variability under the assumption of an isotropic AR(1) process. The large separation of the explained variance between the WS10 mode and the same mode from the AR(1) process suggests that this mode represents a teleconnection pattern of the WS10 anomaly rather than just being a higher order mode of an AR(1) process or the first EOF mode. The EOF pattern from the smaller (NS) domain is very similar, although the corresponding PCs are not highly correlated. The negative correlation between the northern and southern part of the domain is consistent with the lower decorrelation lengths at those two areas (Fig. 3.4).

Third and higher modes cannot be distinguished from the EOF modes of the AR(1) process and seem to be partly determined by the domain geometry and the requirement of the orthogonality of the EOF modes. The third EOF spatial pattern explains the dipole in the WS10 anomaly between the western (west of England) and eastern (above the North Sea and the Baltic Sea) parts of the domain.

For further analysis, the EOF modes from the INS domain are used to ensure an adequate regional representation of WS10 over the North Sea. The first three modes of WS10 anomaly over the INS domain are related to the monthly SLP and T2M anomalies from the annual cycle. The relation between the WS10 and the SLP patterns describes the dynamical forcing of WS10, while relating the WS10 modes to T2M is an attempt to describe the baroclinic contribution to the WS10 anomalies. Even though the third EOF mode seem to only represent the orthogonality requirement of the first EOF mode of an AR(1) process, it was included in

3.3. ANALYSIS METHODS AND RESULTS

Correlation	summer	winter
SLP(1)/NAOI	0.24	0.81
T2M(1)/NAOI	0.52	0.72
SLP(2)/EAI	0.17	0.20
T2M(2)/EAI	0.46	0.13

Table 3.3: Correlation coefficient between NAOI (EAI) from CPC and the first (second) circulation index derived from SLP/T2M.

the following analysis. The justification to neglect the third mode in the following analysis was established with the cross-validation procedure.

For each of the first three PCs of the WS10, two maps of temporally averaged SLP and T2M anomalies are plotted after filtering days for which the PCs of WS10 are higher or lower than the standard deviation separately (Fig. 3.9). The filtered fields plotted in Fig. 3.9 are in the units of their local standard deviation; i.e. each grid point is divided by its standard deviation. For the first three PC modes of the WS10 anomalies, the SLP and T2M anomaly patterns show a bimodal structure. The sign of the extrema changes with a change in the sign of the PC, which suggests an approximately linear relationship between the PCs of WS10 and the large scale circulation. Therefore, a large scale index is defined as a time series of the difference between spatially averaged predictors within a defined centre of activity at extrema (shown in Fig. 3.9) in SLP and T2M separately and is used to predict the PC of WS10 anomalies.

As expected, the first SLP anomaly pattern has a similar spatial structure as the NAOI, although the northern centre is moved slightly eastwards. The correlation between the first SLP index and NAOI from CPC is fairly high only in the winter season, while it is low in the summer season (Tab. 3.3). The first T2M anomaly pattern appears to be almost identical to the surface temperature related to the NAOI (e.g. Trigo et al., 2002), which suggests that the T2M anomaly pattern describes a relationship between SLP and T2M anomalies but adds no additional information for predicting the PC of WS10 anomaly. The second SLP anomaly pattern is a dipole between the SLP over Great Britain/North Sea and Greenland and is not much related to the EA pattern, which is also indicated by a low correlation coefficient between EAI and the second SLP index (Tab. 3.3). The second T2M anomaly pattern is the dipole with minimum above Great Britain and maximum above the south-eastern part of Europe and may be explained by the advection related to the SLP pattern. In the positive phase of the anomaly pattern, the SLP is lower over Great Britain and the cyclonic circulation advects warmer air to eastern Europe and the colder air west of Great Britain. Therefore the T2M anomaly maxima are at these locations. In the negative phase, the situation is approximately inverse. The third SLP anomaly pattern is a dipole between Scandinavia and the North Atlantic west of Great Britain. It is seen that the third pattern has a much lower amplitude compared to the first two patterns, implying a lower association between the third SLP pattern and the third EOF pattern of WS10. The related T2M pattern is a dipole between west of Scandinavia and central North Atlantic. The relationship between the SLP and the T2M anomaly pattern may be explained as with the second pattern.

To test the relationship between the EOF modes of WS10 and the corresponding large scale patterns the cross-validation is preformed as follows. The large scale indices are linearly

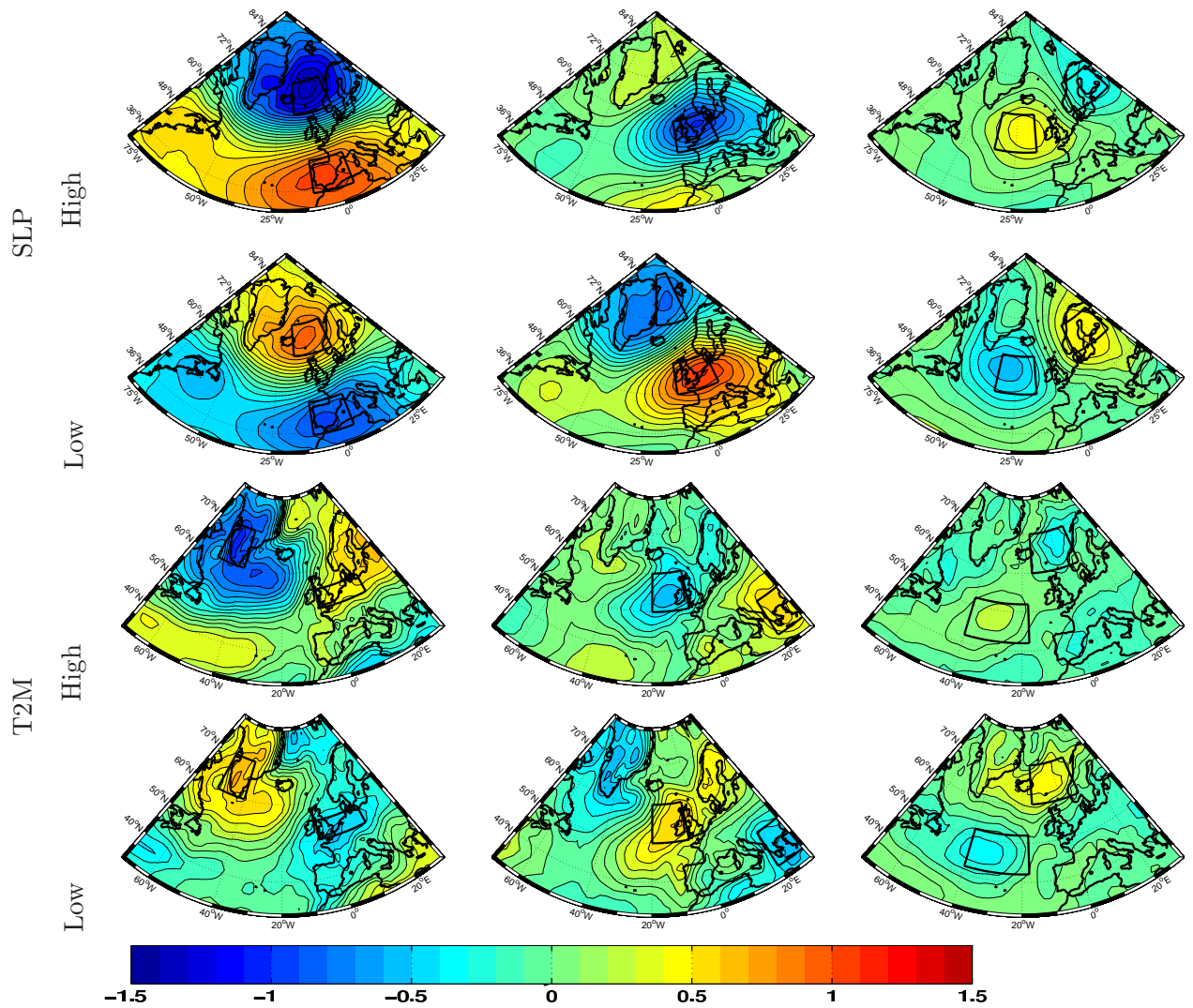


Figure 3.9: First and second row: The mean SLP anomaly for the days of high (first row) and low (second row) first three PCs of wind speed (left to right). Third and fourth row: Same as first and second row, only for T2M instead of SLP. The fields are in units of their local standard deviation.

3.3. ANALYSIS METHODS AND RESULTS

fitted to the corresponding PCs of WS10 anomaly on the 4/5 of the time series length and the fitted relationship was used to predict the remaining 1/5 time series of the PCs of WS10 anomaly. This procedure was repeated five times each time one fifth of the consecutive data was omitted from the fitting procedure and predicted. From the predicted PCs of WS10 anomalies, the whole WS10 anomaly field was reconstructed, assuming that the EOF spatial patterns are constant in time. The ability of the indices to predict WS10 anomaly was estimated by computing the correlation coefficient between the original and predicted WS10 anomaly field. In all cases, the SLP indices were better predictors than T2M indices (not shown). Also using both the SLP and T2M indices at the same time by multiple regressions did not improve the correlation coefficient between the original and the predicted WS10 time series. The highest correlation coefficients were obtained when the first two PCs of WS10 were predicted and used for reconstructing the WS10 anomaly. Including the third EOF mode of WS10 decreases the correlation coefficient. This is since the third EOF mode does not represent significant variability of WS10 and adds mostly noise. Therefore in the further analysis, only the first two EOF modes of WS10 and the related circulation patterns from the SLP are considered.

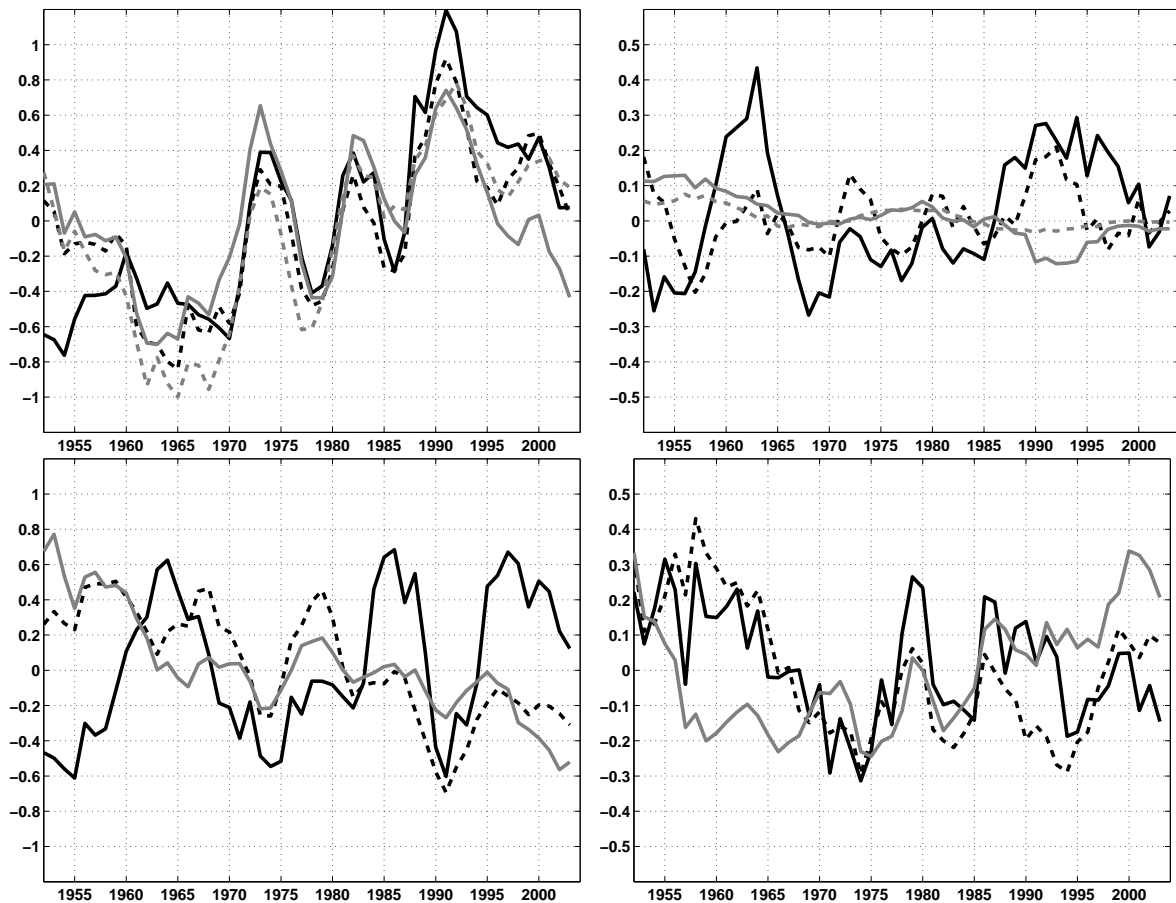


Figure 3.10: Time series of the 5 year running mean PCs of WS10 anomalies (solid black), linearly fitted corresponding SLP index (dashed black), T2M index (solid gray) and NAOI (dashed gray). Upper panel first PC, lower panel second PC. Left panels for winter, right for summer. All data except NAOI is from NCR.

PC	ERA40	NCR
1	0.99 (0.95)	0.99
2	0.95 (0.92)	0.98
3	0.91 (0.89)	0.97

Table 3.4: Correlation coefficient between PCs of WS10 anomalies from different datasets. The numbers in brackets are for the past period (1960-1980), all others for the recent period (1980-2000).

The PCs of WS10 and the large scale circulation indices of SLP and T2M as well as NAOI are shown on Fig. 3.10. The SLP and T2M indices and NAOI are linearly fitted to the PCs of WS10. In the winter, the PCs of WS10 are more variable than in the summer. The first PC of WS10 over the NCR period shows a strong inter-annual variability with an increasing trend. The increasing trend is most pronounced in winter, while only slight increase is observed in the summer. The positive trend is consistent with the NAOI trend (Marshall et al., 2001). In the last decade, a relatively strong decrease of the first PC of WS10 anomaly is observed, reaching almost its mean value over the NCR period. It is not clear if this decrease is due to a change in trend or a manifestation of the inter-annual variability. The first SLP and T2M indices as well as NAOI follow closely the first winter PC of the WS10 on an inter-annual time scales. There is some disagreement between the time series at the beginning of the period (from 1950 to 1960). The reason for this may be the lower quality of WS10 from NCR before 1960 (Kistler et al., 2001). In the summer, the first SLP index captures inter-annual variability of the first PC of WS10 anomaly relatively well, while the NAOI and the T2M index are not able to describe it.

The intra-annual variability of the second PC of WS10 is poorly described by either the SLP or the T2M indices. Especially poor agreement is seen in the winter where even the trends do not match. The trends of the second SLP and T2M index show a decrease, not observed in the PC of WS10 anomaly. During the summer period, inter-annual variability of the second SLP index follows the second PC of WS10 anomaly well. However since only a small improvement in the correlation coefficient of WS10 is achieved when the second PC of WS10 anomaly is related to the indices, it may be inferred that predicting only the first PC of WS10 anomaly is sufficient.

The EOF patterns of WS10 are not very sensitive to the reanalysis dataset used. The correlation coefficients between corresponding PCs of WS10 from NCR and other two reanalysis datasets are very high (up to 0.99), but decreases with the higher order of PC (Tab. 3.4). The correlation coefficient between PCs of WS10 anomalies are slightly higher in the recent period compared to the past period (in brackets).

The correlation coefficients between PCs of WS10 anomaly and the corresponding derived SLP circulation indices are shown in Tab. 3.5. In the winter, the surface winds are much better described by the large scale circulation patterns compared to the summer, which is indicated by high correlation coefficients between the PCs of WS10 and the circulation indices. In this season, the correlation coefficients between PCs of WS10 and circulation indices are not significantly dependent on the reanalysis dataset used. The correlation coefficients in the recent period are considerably higher than in the past period for both NCR and ERA40 data. The reason for the lower correlation coefficients in the past period may be due to the

3.3. ANALYSIS METHODS AND RESULTS

PCs	winter			summer		
	NCR	NCR2	ERA40	NCR	NCR2	ERA40
1	0.85 (0.61)	0.86 (-)	0.85 (0.55)	0.49 (0.43)	0.46 (-)	0.54 (0.47)
2	0.61 (0.29)	0.59 (-)	0.59 (0.42)	0.31 (0.35)	0.35 (-)	0.43 (0.49)

Table 3.5: Correlation coefficients between PCs of WS10 anomaly and the circulation patterns for the recent period (1980-2000, without brackets) and for the past period (1960-1980, in brackets).

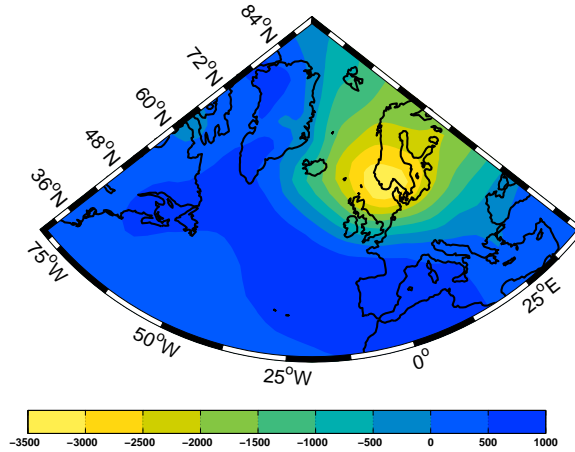


Figure 3.11: The SLP anomaly [Pa] from NCR related to high WS over the NS domain.

better quality of WS10 data in the recent period with the assimilation of the satellite derived near-surface wind speeds or the change in the climate dynamics within the last decades. Since the PCs of WS10 anomalies from different reanalysis in the past period differ more than in the recent period, we argue that at least part of the lower correlation between PCs of WS10 anomalies and circulation patterns in the past period may be related to the lower data quality of the reanalysis data of the past period.

3.3.3 Extreme wind conditions

In this paper, the extreme wind speeds are defined as for example in Pryor and Barthelmie (2003) with pre-defined high percentiles of the daily WS10 distribution. The WS10 percentiles are calculated for each winter season. The winter season was selected where the highest wind speeds during the storms are predominant. For example, the 90 percentile of WS10 is defined when WS10 is exceeded in 10% of the days during the winter season in a given year. The extreme WS10 and its relation to the circulation patterns can be assessed from the high PCs of WS10 or the high intensity of the circulation indices as shown in the previous chapter. However, EOF functions are not optimally designed to capture extreme values since the extreme values occur rarely and thus do not necessarily have an important contribution to the total variance of data which is the criteria for extracting EOF patterns. Moreover, there is also a scale mismatch between the circulation patterns that describe the variability of WS10

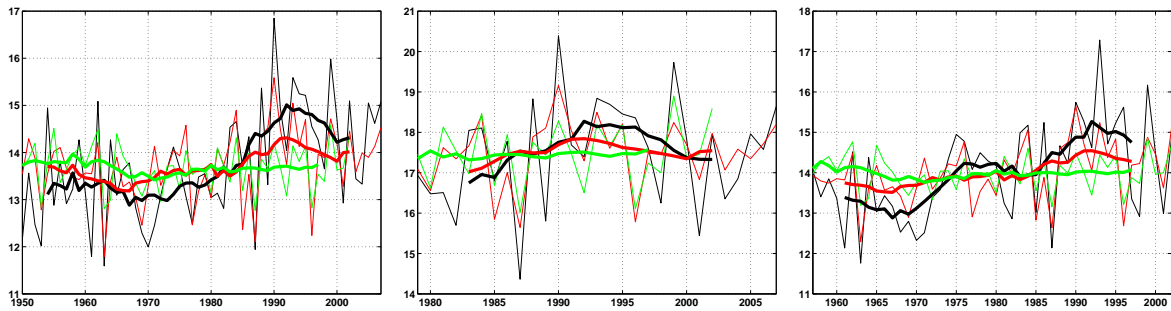


Figure 3.12: 90th percentile of winter WS10 [m s^{-1}] (black lines), related circulation indices from reanalysis models (red lines) and from measured SLP (green lines). Thin lines represent yearly data, the thick 9 yrs. moving average. Top for NCR, middle for NCR2 and bottom for ERA40 data.

and the typical duration of extreme WS10. Typical duration of the extreme wind speeds by definition cannot exceed a few days, while the first EOF pattern of WS10 is related to the NAO like patterns which is known to describe well the monthly to inter-decadal variability of the SLP (e.g. Hurrell and van Loon, 1997). The more scale-appropriate circulation patterns describing the extreme WS10 may be obtained for example from the circulation types such as from the Grosswetterlagen (GWL) catalogue, which usually persist for few days (e.g. James, 2007).

Therefore, to find a relationship between the extreme WS10 over the North Sea and the corresponding circulation patterns, a slightly different approach is considered as described below. For each day, a maximum WS10 (MWS10) over the German Bight region is first calculated. The circulation pattern related to the extreme WS10 is found in the following manner. The map of time averaged SLP anomalies for the days when the MWS10 exceeds twice its standard deviation over the mean value is plotted on Fig. 3.11. It is observed that the high WS10 are related to an anomalously low SLP over Scandinavia. This SLP pattern is related to the Cyclonic-Westerly and Cyclonic-Northwesterly GWL, which have already been identified and related to the wind storms over the North Sea. The resultant SLP pattern is very robust regarding the choice of the mean or the maximum WS10 over German Bight or the reanalysis dataset used. Also, almost the same pattern is obtained by using the more complicated method of extreme associated functions described in Panja and Selten (2007), which finds the combination of EOF patterns that are optimally related to the extreme WS10. The SLP index related to the extreme WS10 can be derived as the negative of the spatial averaged SLP anomaly over the area of the lowest SLP anomaly (lat. 55N–70N, lon. 10E–25E) as in Fig. 3.11. The index is also constructed from the SLP measurements at stations located in the southern part of the Scandinavian peninsula. The advantage of deriving the index from measurements is that the pressure measuring techniques did not significantly change in the last century and thus the measurement cause less problems regarding temporal inconsistencies compared to the SLP from the reanalysis data. Here, the measured index is constructed as the negative of the mean daily SLP measurement at the synoptic stations in Göteborg (Sweden) and Oksoy (Norway). The results do not change, if SLP from only one of the stations is taken instead of the average of both stations.

The relationship between the SLP index and the extreme WS10 is almost linear (not

3.3. ANALYSIS METHODS AND RESULTS

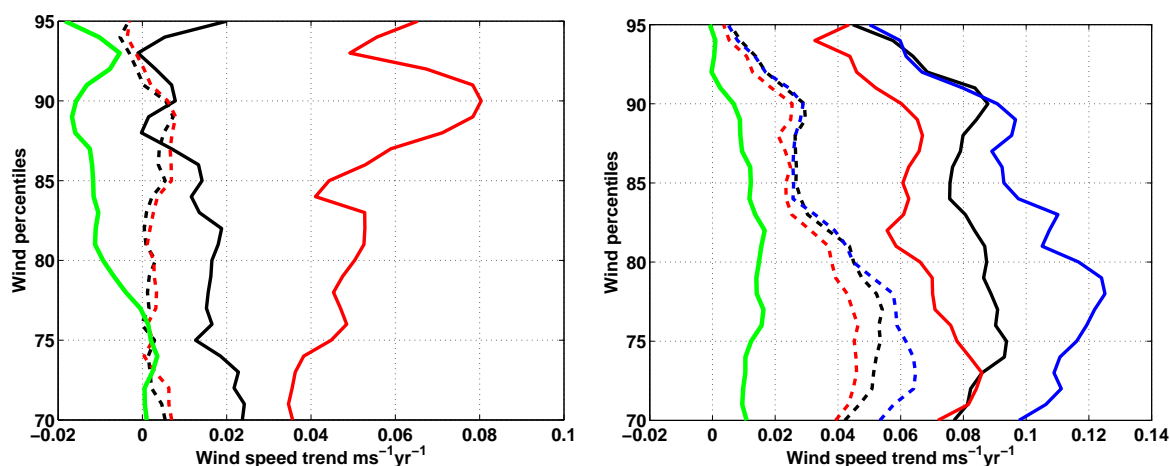


Figure 3.13: Linear trends of the high percentiles (from 70 to 90) of winter MWS (solid lines) and high percentiles of related circulation patterns (dashed lines) for past (left) and recent (right) period. Green line is for measured SLP, black for NCR, blue for NCR2 and red for ERA40.

shown), the high percentiles of the MWS10 are fitted to the high percentiles of the SLP index. For example, the annual time series of the 90 percentile of MWS10 and the 90th percentile of the indices (from both reanalysis and measurements) linearly fitted to the 90 percentile of MWS10 are shown in Fig. 3.12. The correlation coefficient between the time series of the 90th percentiles of MWS10 and 90 percentiles of the related indices are relatively high (exceeding 0.7 for all datasets). However, the time series of the 90th percentiles of MWS10 and the related indices show consistently different inter-annual variability. The time series of the 90th percentiles of MWS10s are also sensitive to the reanalysis dataset. The 90th percentile of the MWS10 from the NCR shows almost no inter-annual variability till the mid of 1970s and subsequently a strong increase which reaches a maximum in the mid 1990s and a decrease thereafter with a slight increase towards the end. The results from NCR2 are similar to NCR for the common data period. The 90 percentile of MWS10 from ERA40 is slightly decreasing till beginning of the 1970s, then shows a sudden jump over a few years followed by a constant period and an increase till mid 1990s with decrease thereafter. The 90 percentiles of the SLP index from the reanalysis agree with respect to the MWS10 being relatively constant till the mid-1980s and then show a slight increase till the mid-1990s and a decrease thereafter. The indices show significantly smaller trends compared to the WS10. The MWS10 index derived from the measurement is amazingly constant in time and does not show an increase from late 1970s till mid 1990s.

The disagreement of the inter-annual variability between the high percentiles MWS10 and the related indices fitted to the MWS10 are observed in other high percentiles. In Fig. 3.13, the linear trends are shown during the recent and the past period. The high percentile indices derived from the measurements show no significant trend. The index derived from the reanalysis SLP shows a slight trend in the recent period, which in most cases is not significant, while the high percentiles of WS10 show significant trends towards higher high percentiles of

WS10. We investigated if the trend in MWS10 may have resulted by the change in thermal forcing. The T2M and thickness between 700 hPa and 1000 hPa was used to calculate the extreme indices, same as with the SLP and were related to the MWS10. None of these two indices was able to explain the inter-annual variability of MWS10.

3.4 Discussions and Conclusions

The representation of daily mean WS10 over the North Sea between the NCR, NCR2 and ERA40 reanalysis data is compared with the main goal to assess the reliability and deficiencies of the datasets for applications such as the long term wind resource assessment. The WS10 over the North Sea from different reanalysis sources is highly correlated, as shown by the high linear correlation coefficient of the data as well as the correlation coefficient between the first three PCs from different reanalysis datasets (Tab. 3.2). The agreement between PCs of WS10 is slightly better in the recent period (1980-2000) compared to the past period (1960-1980) which can partially be attributed to the improved WS10 dataset in the recent period probably due to assimilation of satellite measured wind data.

Some important differences in the WS10, such as its mean magnitude and linear trends of time averaged values, are model dependent which can be at least partially attributed to the choice of parameterizations of boundary layer, surface layer and land surface processes and the model resolutions. The WS10 from reanalysis is interpolated from the first model level to 10 m height using surface layer parameterizations and is also sensitive to the vertical model resolution. As a result, in the recent period, the mean magnitude of NCR WS10 is around 2 m s^{-1} lower than in NCR2 WS10. Also, the linear trends of annual mean WS10 are significantly different among the three reanalysis datasets. Since the trends and the mean values of WS700hPa from all models are nearly the same again increases the confidence in this reasoning.

Next, the imprint of local circulation patterns on the WS10 climatology over the NS domain resolved in the high resolution model (WRF) simulations is investigated. Some of the processes such as the land-sea breezes are to some degree smoothed by averaging the WS10 on the daily time step. It is expected that the daily WS10 in the low resolution dataset is well represented since the decorrelation length of daily WS10 is around 800 km which is considerably larger than the horizontal resolution of the reanalysis models. Exceptions are only at the coast of Weser-Ems area and Holland which probably deviate due to the influence of the local circulation patterns. The comparison of WS10 reanalysis data with a high resolution dataset (WRF3) for the three year (2003-2006) period is sufficiently long to warrant a closer examination of the influence of local processes on the WS10. Comparing the NCR reanalysis data to the high resolution WRF3, it was again confirmed that the variability of daily WS10 over the North Sea is mostly well described by the low resolution reanalysis dataset. The highest deviations between NCR and WRF3 data were found mostly along the coast which indicates the influence of the local circulation patterns that can not be resolved in the low resolution dataset. As with the different reanalysis datasets, the mean magnitude of the WS10 from the NCR and high resolution datasets differ. The exact location of the coastline is not well resolved in the NCR resulting in larger deviations between the NCR and high resolution WS10 along the coast.

The dominant modes of the mean monthly WS10 described by the EOF modes are related to the SLP and T2M patterns. The SLP and T2M patterns were obtained empirically to

represent the forcing on WS10 such that the circulation indices (corresponding time series) are well correlated to the PCs of WS10. The circulation indices were fitted to the corresponding PCs of WS10 in order to hindcast the WS10. There are alternative approaches for searching the dominant modes of WS10 variability and its relationship to the circulation patterns. For example, Fil and Dubus (2005) preferred cluster analysis over EOFs of the northern European SLP in order to isolate the climate regimes since the cluster analysis does not require an assumption of the linearity. However, for the analysis presented here, the cluster analysis is not well suited, since it would be harder to obtain the continuous relationship between the large scale indices and the clusters of WS10 anomaly. The other alternative would be to use one of the multivariate methods for finding the relationship, such as Canonical Correlation Analysis (CCA) (von Storch and Zwiers, 1999) of the EOF pre-filtered fields. However, the disadvantage of the CCA is that its patterns do not necessarily represent a large proportion of the data variability. The T2M pattern does not bring a significant improvement in explaining the WS10 variability. Most of the inter-annual variability of the WS10 explained by the first EOF pattern describes a coherent increase of WS over the North Sea region and is related to a SLP pattern similar to the NAO. However, the northern centre of the pattern found in this study is shifted eastwards and is very similar to the pattern found by (Kaas et al., 1996). In the winter, the correlation coefficient between first SLP index and NAOI is high. The first SLP index is highly correlated to the first PC of WS10 only in the winter. The higher correlation between the first PC of WS10 and the SLP index in the winter reflects that the empirically found pattern is better correlated to the WS10 variability compared to the NAOI. The second SLP pattern is the SLP anomaly between Scandinavia and Greenland and is related to the WS10 dipole over south and north of Great Britain. The index from the second circulation pattern is well related to the WS10 in the recent period, whereas it was rather poor in the past period. Again, it is not self evident if this is an indication of the better quality of the WS10 data in the recent period compared to the past period or reflects the changes between the recent and past period. The second SLP and WS10 patterns seem to reflect the monthly mean position of the storm tracks and increases toward the end of the reanalysis period which is consistent with the observed northern shift of storms tracks in the recent period (Schneidereit et al., 2005; Wang et al., 2006).

The extreme wind speeds are described as the WS10 exceeding a predefined high percentile (e.g. 90th) of daily WS10 for each year in winter season separately. The extreme circulation patterns related to the high daily WS10 were found by filtering the SLP anomalies for the days when WS10 cross a predefined limit. The search for the different SLP patterns related to the extreme wind speeds may not be suitable since the patterns based on the EOF functions are not designed to find rare extreme values. The extreme wind speeds in the German Bight are related to the low SLP over Scandinavia. The time series of the extreme WS10s are insensitive to the reanalysis datasets used in the analysis. In the past period, there are an important differences between the extreme WS10s from different reanalysis, while in the recent period, the correspondence is better. The circulation indices defined as the same percentiles of the negative SLP over the Scandinavia and regressed on the extreme percentiles of the WS10 show considerably less inter-annual variability; especially the increase from the 1960s to the mid 1990s is underestimated. Similar SLP index was constructed from the daily SLP measurements at two stations in the south of the Scandinavian peninsula (Göteborg and Oksoy). The circulation index from these two stations shows incredibly little inter-annual variability. These results show high sensitivity to the methodology of the estimation of extreme wind speeds. It has been noted in the literature, that the time series of extreme

near surface wind speeds are very different when estimating them from the wind speeds and from the proxy data like the SLP. We showed here that even if the data from the same reanalysis is used, which is expected to be highly consistent, the deviations in the inter-annual variability of extreme wind speeds exist. The extreme wind speeds are probably only partially captured in the SLP patterns.

The analysis of different resolution data sets was undertaken in this study to comprehensively describe the current state of surface wind climate (WS10) over the North Sea. In particular a methodology to detect and examine a regional indicator of climate change influencing primarily the surface marine wind field is developed and applied. This methodology is applied in a subsequent study to compare and investigate the surface wind climate states in the regional climate hindcasts and future climate scenarios.

Acknowledgements

The data used in this study was obtained from NCEP/NCAR, ECMWF and CPC. The work was partially supported by the European Union Marie-Curie Early Stage Researcher Program Modobs (MRTN-CT-2005-019369).

Bibliography

- Alexandersson, H., H. Tuomenvirta, T. Schmith, and K. Iden, 2000: Trends of storms in NW Europe derived from an updated pressure data set. *Climate R.*, **14**, 71–73.
- Ansell, T. J., et al., 2006: Daily mean sea level pressure reconstructions for the European-North Atlantic region for the period 1850-2003. *J. Climate*, **19** (12), 2717–2742.
- Barnston, A. G. and R. E. Livezey, 1987: Classification, seasonality and persistence of low-frequency atmospheric circulation patterns. *Mon. Weather Rev.*, **115**, 1083–1126.
- Deser, C. and M. L. Blackmon, 1993: Surface climate variations over the North Atlantic during winter: 1900 – 1989. *J. Climate*, **6**, 1743–1753.
- Dommenges, D., 2007: Evaluating EOF modes against a stochastic null hypothesis. *Clim. Dynam.*, **28**, 517–531.
- Fil, C. and L. Dubus, 2005: Winter climate regimes over the North Atlantic and European region in ERA40 reanalysis and DEMETER seasonal hindcast. *Tellus*, **57A**, 290–307.
- Greatbatch, R. J. and P.-P. Rong, 2006: Discrepancies between different northern hemisphere summer atmospheric data products. *J. Climate*, **19** (7).
- Hurrell, J. W. and H. van Loon, 1997: Decadal variations in climate associated with the North Atlantic oscillation. *Climate Change*, **36**, 301–326.
- James, P. M., 2007: An objective classification method for Hess and Brezowsky Grosswetterlagen over Europe. *Theoretical and Applied Climatology*, **88**, 17–24.
- Janjić, Z., 2002: Nonsingular implementation of the Mellor–Yamada level 2.5 scheme in the NCEP Meso model. *NCEP Office Note*, **No. 437**.
- Kaas, E., T.-S. Li, and T. Schmith, 1996: Statistical hindcast of wind climatology in the North Atlantic and northwestern European region. *Climate R.*, **7**, 97–101.
- Kalnay, E., et al., 1996: The NCEP/NCAR 40-year Reanalysis Project. *Bull. Am. Meteorol. Soc.*, **77** (3), 437–471.
- Kanamitsu, M., W. Ebisuzaki, J. Woollen, S.-K. Yang, J. Hnilo, M. Fiorino, and G. L. Potter, 2002: NCEP-DOE AMIP-II reanalysis (R-2). *Bull. Am. Meteorol. Soc.*, **83** (11), 1631–1643.
- Kistler, R., et al., 2001: The NCEP-NCAR 50-year reanalysis: Monthly means CD-Rom and documentation. *Bull. Am. Meteorol. Soc.*, **82** (2), 247–268.
- Marshall, J., et al., 2001: North Atlantic climate variability: Phenomena, impacts and mechanisms. *Int. J. Climatol.*, **21**.
- Matulla, C., W. Schöner, H. Alexandersson, H. von Storch, and X. L. Wang, 2007: European storminess: Late nineteenth century to present. *Clim. Dynam.*
- North, G. R., T. L. Bell, and R. F. Cahalan, 1982: Sampling errors in the estimation of empirical orthogonal functions. *Mon. Weather Rev.*, **110**, 699–710.

BIBLIOGRAPHY

- Panja, D. and F. M. Selten, 2007: Extreme associated functions: Optimally linking local extremes to large-scale atmospheric circulation structures. *Atmos. Chem. Phys. Disc.*, **7**.
- Preisendorfer, R. W., 1988: *Principal Component Analysis in Meteorology and Oceanography*. Developments in Atmospheric Science no. 17, Elsevier, Amsterdam.
- Pryor, S. C. and R. J. Barthelmie, 2003: Long-term trends in near-surface flow over Baltic. *Int. J. Climatol.*, **23**, 271–289.
- Pryor, S. C., R. J. Barthelmie, and J. T. Schoof, 2006: Inter-annual variability of wind indices across Europe. *Wind Energy*, **9**, 27–38.
- Richman, M. B., 1986: Rotation of principal components. *J. Climatol.*, **6**, 293–335.
- Rogers, J. C., 1997: North Atlantic storm track variability and its association to the North Atlantic Oscillation and climate variability of northern Europe. *J. Climate*, **10**, 1635–1647.
- Santer, B. D., T. Wigley, J. S. Boyle, D. J. Gaffen, J. J. Hnilo, D. Nychka, D. E. Parker, and K. E. Taylor, 2000: Statistical significance of trends and trend differences in layer-average atmospheric temperature time series. *J. Geophys. Res.*, **105 (D6)**, 7337–7356.
- Schmidt, H. and H. von Storch, 1993: German Bight storms analysed. *Nature*, **365**, 791.
- Schneidereit, A., R. Blender, K. Fraedrich, and F. Lunkeit, 2005: Icelandic climate and North Atlantic cyclones in ERA-40 reanalysis. *Meteorol. Z.*, **14 (1)**.
- Skamarock, W. C., J. B. Klemp, J. Dudhia, D. O. Gill, D. M. Barker, W. Wang, and J. G. Powers, 2005: A description of the advanced research WRF version 2. Tech. rep., NCAR Technical Note.
- Sood, A., K. Sušelj, and D. Heinemann, 2007: Wind resource assessment in the offshore and coastal domain of the German Bight using high resolution validated mesoscale simulations compared to the standard techniques. *European Wind Energy Conference*, Milan, Italy.
- Trigo, R. M., T. J. Osborn, and J. M. Corte-Real, 2002: The North Atlantic Oscillation influence on Europe: Climate impacts and associated physical mechanisms. *Climate R.*, **20**, 9–17.
- Uppala, S. M., et al., 2005: The ERA-40 re-analysis. *Q. J. R. Meteorol. Soc.*, **131 (612)**, 2961–3012.
- von Storch, H. and F. W. Zwiers, 1999: *Statistical analysis in climatology*. Cambridge, Cambridge Univ. Press.
- Wang, X. L., V. R. Swail, and F. W. Zwiers, 2006: Climatology and changes of extratropical cyclone activity: Comparison of ERA-40 with NCEP-NCAR reanalysis for 1958-2001. *J. Climate*, **9 (13)**, 3145–3166.
- Weisse, R., H. von Storch, and F. Feser, 2005: Northeast Atlantic and North Sea storminess as simulated by a regional climate model 1958-2001 and comparison with observations. *J. Climate*, **18 (3)**, 465–479.

Yan, Z., S. Bate, R. E. Chandler, V. Isham, and H. Wheeler, 2006: Changes in extreme wind speeds in NW Europe simulated by generalized linear models. *Theor. Appl. Climatol.*, **83**, 121–137.

Yiou, P. and M. Nogaj, 2004: Extreme climatic events and weather regimes over the North Atlantic: When and where? *Geophys. Res. Lett.*, **31**.

4

The near surface wind speed over Europe and the North Atlantic in future climate[†]

Abstract

In this paper we investigate the climate change of the Wind Speed at 10 meters height (WS) over the North Atlantic and the Europe based on simulations from 16 Global Circulation Models (GCMs) presented in the 4th IPCC report. The future climate is from simulations forced by the IPCC SRES A2 greenhouse gas scenario (covering the period 2061-2100) and the past climate is forced by the observed greenhouse gas concentrations (period 1961-2000). First from the reanalysis data, the WS patterns explaining the dominant part of the WS trend were found and related to the Sea Level Pressure (SLP) patterns. The climate change of the WS was calculated based on the change of the strength of the SLP patterns from the past to the future climate. There is a clear signal of the increase of the future WS in winter (December-February), over most of the North Atlantic with the largest increase over the central North Atlantic reaching the magnitude between 0.5 m s^{-1} and 2.5 m s^{-1} . In other seasons, the climate change signal of the WS is weak. The WS is expected to increase over the north-western part of the North Atlantic and decrease over the south-eastern part of the North Atlantic whereas the expected magnitude of the climate change is smaller than 1 m s^{-1} . Some uncertainty of the above results remains since the GCMs are unable to properly reproduce the variability of the relevant SLP pattern in the 20th century climate. Although the results of this study are quantitative change of the WS with the uncertainty intervals, it can also be used as a study to help selecting the most appropriate GCM results to downscale them further in order to compute the best estimates of local high resolution wind conditions.

4.1 Introduction

The climate change of the Near Surface Wind (NSW) over the European and North Atlantic region is not only important for human activities such as wind power production, shipping, construction, etc. but it is also closely linked to other climate variables, such as temperature, cloudiness, etc. mainly due to the change of the advection of the air masses. For example, in the winter season the temperature and precipitation over the northern Europe are highly related to the magnitude and direction of the NSW (e.g. van Oldenburgh and van Ulden,

[†]The work presented in this chapter is under review for publication in Tellus Series A: Dynamic Meteorology and Oceanography as: Kay Sušelj and Abha Sood: *The near surface wind speed over Europe and the North Atlantic in future climate.*

CHAPTER 4. CLIMATE CHANGE OF WS OVER EUROPE AND NORTH ATLANTIC

2003). Westerly winds advect warmer and moister marine air from the Atlantic Ocean over the northern Europe, while the eastern winds advect cold and dry continental air from Siberia.

The 4th Intergovernmental Panel on Climate Change (IPCC) report (Christensen et al., 2007) concluded that the confidence in the climate change of the NSW magnitude over Europe in the next century is low. Recently, Räisänen et al. (2004) and Pryor et al. (2005) evaluated the change of the European NSW speed in the 21st century as simulated by the Swedish Rossby Center Regional Climate Model (RCM) forced by two different global circulation models (GCMs). Both studies show high sensitivity of the RCM results to the GCM forcing. The RCM results forced by one of the GCM do not show any significant change in the NSW characteristics, while the results forced by the other GCM show an increase of the annual NSW magnitude in the northern Europe and a decrease over the southern Europe. Räisänen et al. (2004) found that the possible change of the NSW depicts a strong annual cycle. In winter, over the northern Europe the NSW is expected to increase whereas in the summer it is expected to decrease. The main conclusion of both studies is that the change of the NSW is mainly induced by the change of the large scale circulation patterns which are well simulated by the GCMs, while the local forcings (such as change of the atmospheric stability) play a secondary role.

Therefore, one approach to study the climate change of NSW is to detect the climate change of the relevant circulation patterns and from the change of the circulation patterns derive the climate change of the NSW. This can be achieved for example by studying the change in the magnitude of the North Atlantic Oscillation (NAO) (e.g. Marshall et al., 2001), the dominant low frequency circulation pattern in the northern hemisphere, which is well related to the NSW over North Atlantic and Europe. In the positive NAO phase, the northern Europe is under the influence of stronger storm activity where the NSW is anomalously western, while the southern Europe is under influence of weaker storm activity and the NSW is anomalously eastern (Trigo et al., 2002). In the negative NAO phase, the situation is approximately reversed. The NAO not only explains the dominant part of the low frequency circulation in the northern hemisphere, but also the dominant part of the long term change in the Sea Level Pressure (SLP) pattern (Corti et al., 1999; Hannachi, 2007). Although NAO well describes the climate change of the NSW, it is however not clear whether the NAO is optimally related to the climate change of the NSW over the North Atlantic and Europe. Also, the magnitude of the NSW is nonlinearly related to the NSW, therefore the magnitude of the NSW has to be computed from the high resolution NSW (e.g. daily scale, on which the synoptic scale processes are captured), where the role of the NAO Index (NAOI) to describe the significant part of the SLP variability becomes weak (Blessing et al., 2005). The question which now arises is whether the climate change of the high resolution NSW can be described by the climate change of the NAOI or if it is better to relate it to the climate change of the synoptic weather types, such as Grosswetterlagen. Also, it has been shown by many authors (Osborn, 2004; Gillett et al., 2003; Miller et al., 2006) that the simulated NAOI from the state of the art GCMs in general underestimate its natural variability in the past climate. So far no consensus has been reached on the missing physical processes responsible for the underestimation of the NAO variability in the past climate (Schwierz et al., 2006). Some of the proposed causes are too low model heights unable to properly describe the coupling between the troposphere and stratosphere (Scaife et al., 2005; Miller et al., 2006) and improper setting of the gravity wave drag parameterization (Sigmond et al., 2008).

The importance of the circulation patterns for the NSW variability over the North Europe has been noted by many researchers (e.g. Alexandersson et al., 2000; Pryor and Barthelmie,

2003; Pryor et al., 2006). Pryor and Barthelmie (2003) related the observed increase of the NSW magnitude over the Baltic Sea in the last part of the 20th century to the increase in the westerly type of Grosswetterlagen. Pryor et al. (2006) linked the distribution of the past NSW magnitude described by the Weibull probability density function parameters to the SLP indices (i.e. gradient and vorticity of SLP) and based on the change of the SLP indices from numerous GCMs derived the climate change of the NSW. They found small increase of the NSW magnitude from the 20th to the 21st century which is also inconsistent among the GCMs.

In the work presented in this paper, the patterns explaining the dominant part of the NSW trend¹ in the past climate are extracted and optimally related to the circulation patterns obtained from the SLP. From the climate change of the relevant circulation patterns in the 21st century climate, the climate change of the NSW is estimated. We assume that the dominant patterns describing trend of NSW as well as their relation to the circulation patterns stays the same in the future climate. Our approach is similar to the one of Pryor and Barthelmie (2003) and Pryor et al. (2006) where they related the circulation patterns (or SLP) to the NSW in order to describe the climate change of the NSW. However, the relationship between the NSW and the SLP was not optimized in describing the trend of NSW but in describing its variance. Since the climate signal of NSW over North Atlantic and Europe is weak (e.g. Räisänen et al., 2004), it is important to find the NSW patterns optimally describing its trend.

The paper is organized as follows. In the Sec 4.2, the data and the methods used in this study are described. In Sec 4.3, the patterns describing the dominant part of the NSW trend and relation to the SLP patterns from the past reanalysis data are extracted and presented. Similar analysis as for the past data is done for a sample climate model in Sec 4.4 in order to investigate the sensitivity of the patterns to the dataset or the period under consideration. The time evolution of the relevant SLP patterns from the GCMs and the change of the NSW magnitude from the past to the future climate is shown in Sec 4.5. Finally, the discussions and conclusions are presented in Sec 4.6.

4.2 Data and methods

In order to derive the patterns explaining the significant spatially correlated wind speed trend, the mean daily Wind Speed at 10 m height (WS) over the North Atlantic and European region (lat. 35°N-80°N, lon. 70°W-30°E) as vector of the zonal and meridional components has been used. The related circulation patterns were derived from the Sea Level Pressure (SLP) over the northern hemisphere (lat. 30°N-90°N). Both WS and SLP are part of the ECMWF ERA40 reanalysis (ECMWF) (Uppala et al., 2005) dataset available on $2.5^\circ \times 2.5^\circ$ horizontal resolution and cover a 45 years period (September 1 1957 to August 31 2002). The mean daily values are 4 time per day averaged analysis values. Although the main focus of this analysis is to investigate the magnitude of the WS, the wind vector is preferred for the analysis, since the SLP directly influences wind vector implying that its patterns are better related to the SLP patterns. The reason for the preference of the daily WS data for the analysis is that on the daily time step the WS variability caused by the synoptic scale processes is well described, while it does not contain a signal from diurnal cycle. Here, we develop a methodology to statistically reconstruct the daily WS from the strength of the

¹ Trend is a smooth and usually monotonic change, in this study of the NSW, which over the long periods of many decades indicates a change in the state of the climate.

monthly SLP patterns and then calculate the magnitude of the WS from the daily WS as described below.

As an additional historic SLP dataset, the mean monthly SLP from the HadSLP2 dataset covering period from 1850 to 2004 were used (Allan and Ansell, 2006). The HadSLP2 data is based on the observations and is gridded on horizontal resolution of $5^\circ \times 5^\circ$. Allan and Ansell (2006) showed that HadSLP2 data well reproduce the observed temporal variability of the prominent modes of the atmospheric circulation in the Northern hemisphere such as NAOI.

The results from the General Circulation Models (GCMs) prepared for the 4th IPCC report² were used to investigate the climate change of the WS. We constructed a 250 years (1851-2100) time series of the mean monthly SLP. The SLP for the past and the future climate are from the simulations forced by the observed greenhouse gases and aerosols and the radiative forcings based on IPCC SRES A2 scenario respectively. Results from 16 GCMs were used, for some models multiple ensembles are available calculated from perturbed initial conditions. Tab. 4.1 lists the GCMs, the country of origin, their code names used for further reference, horizontal resolution and the number of available ensembles.

To investigate the sensitivity of the significant WS patterns and their relation to SLP patterns obtained from the ECMWF data, the mean daily SLP and WS were used as a combination from one of the ensemble members of the ECHAM5/MPI-OM GCM with the observed forcings (1981-2000) and the IPCC SRES A2 scenario forcings (2046-2065 and 2081-2100). The reason for selecting ECHAM5/MPI-OM simulations is that the near-surface daily wind speeds are available and that the ECHAM5/MPI-OM results of the past climate well represent the mean circulation over Europe (van Ulden and van Oldenborgh, 2006).

The analysis was performed on the four seasons independently: December-February (DJF), March-May (MAM), June-August (JJA) and September-November (SON). The mean annual cycle was removed from each grid point of the data as described next. First, the monthly mean annual cycle was computed as a mean of the values in each calendar month. The daily mean annual cycle was calculated by assuming that the values of the monthly mean annual cycle are valid for the 15th day of the daily mean annual cycle for corresponding month and linearly interpolated in between. The data with removed annual cycle were calculated as the difference between the original data and the daily mean annual cycle. For each season separately, the data were normalized to have the unit variance at each grid-point in order that the spatially varying magnitude does not play the role in defining the patterns.

Trend Empirical Orthogonal Functions (TEOF) analysis is used to derive the patterns explaining the majority of spatially coherent trend of WS. The method is described in detail by Hannachi (2007); here a brief overview of the method is given and its application is described. The TEOFs can be seen as a rotation of data, similar to EOF, but with different criteria defining the dominant modes as follows.

Let the primary multivariate data measured at n locations and t times be written in matrix \mathbf{S} with the dimension of $n \times t$ and the secondary data measured at m (not necessarily the same) locations and at the same t times be written in the matrix \mathbf{Z} with the dimension $m \times t$. The primary data is the data for which the trend patterns are to be extracted (i.e. WS in this study), while the secondary data is the forcing data (SLP) from which the akin patterns are statistically extracted and envisaged to be physically linked to the primary data. Before the analysis, the data in matrices \mathbf{S} and \mathbf{Z} are centered in time and normalized to

²Data were downloaded from the World Climate Research Programme's (WCRP's) Coupled Model Inter-comparison Project phase 3 (CMIP3) multi-model dataset

Originating Group(s)	Country	Short Name	Horizontal Resolution (lat.×lon.)	Num. of ensembles
Canadian Center for Clim. Modelling and Analysis	Canada	CGCM3.1	3.75° × 3.75°	4
CSIRO Atmosph. Res.	Australia	CSIRO-Mk3.0	1.9° × 1.9°	1
CSIRO Atmosph. Res.	Australia	CSIRO-Mk3.5	1.9° × 1.9°	1
Meteorol. Institute of the Univ. of Bonn / Meteorol. Research Institute of KMA	Germany Korea	ECHO-G	3.75° × 3.75°	3
US Dept. of Commerce / NOAA / Geophysical Fluid Dynamics Laboratory	USA	GFDL-CM2.0	2° × 2.5°	1
Hadley Centre for Clim. Prediction and Res. / Met Office	UK	UKMO-HadCM3	2.5° × 3.75°	1
Institute for Numerical Mathematics	Russia	INM-CM3.0	5° × 4°	1
Institute Pierre Simon Laplace	France	IPSL-CM4	2.5° × 3.75°	1
Center for Clim. System Res. / National Institute for Environmental Studies / Frontier Res. Center for Global Change	Japan	MIROC3.2 (medres)	2.8° × 2.8°	3
National Center for Atmospheric Research	USA	CCSM3	1.4° × 1.4°	3
Météo-France / Center National de Recherches Météorologiques	France	CNRM-CM3	2.8° × 2.8°	1
Max Planck Institute for Meteorology	Germany	ECHAM5/MPI-OM	1.9° × 1.9°	3
US Dept. of Commerce / NOAA / Geophysical Fluid Dynamics Laboratory	USA	GFDL-CM2.1	2° × 2.5°	1
NASA / Goddard Institute for Space Studies	USA	GISS-ER	4° × 5°	1
Hadley Center for Clim. Prediction and Res. / Met Office	UK	UKMO-HadGEM1	1.25° × 1.875°	1
Meteorol. Res. Institute	Japan	MRI-CGCM2.3.2	2.8° × 2.8°	4

Table 4.1: List of the GCMs with the contry of origin, code name for reference, horizontal resolution and number of ensembles from which the SLP is used in this study

unit variance, i.e. the mean of each row in data matrices \mathbf{S} and \mathbf{Z} is zero and its standard deviation is one.

The modes which explain the largest proportion of a coherent trend in the primary data are obtained with the EOF analysis (e.g. von Storch and Zwiers, 1999, chap. 13) of the weighted matrix \mathbf{Q} , where the rows of \mathbf{Q} are permutations \mathcal{P} of the $[1\ 2\ \dots\ t]$ where \mathcal{P} is such that it orders the values of the corresponding row of matrix \mathbf{S} from the smallest to the largest. The data in matrix \mathbf{Q} are weighted by the square root of the cosine of the corresponding latitude to account for the converging latitudes towards the pole. Let the k -th Empirical Orthogonal Function (EOF, spatial pattern) of matrix \mathbf{Q} be written in column vector \mathbf{q}_k and the k -th Principal Components (PC, time series) be written in a row vector \mathbf{a}_k so that $\mathbf{Q} = \sum_{k=1}^n \mathbf{q}_k \cdot \mathbf{a}_k$. To obtain the k -th Trend Empirical Orthogonal Function (TEOF, spatial pattern) and Trend Principal Component (TPC, time series), first the time series $\mathbf{w}_k = \mathbf{q}_k^T \cdot \mathbf{S}$ is calculated and scaled to the unit variance. The k -th TEOF pattern (\mathbf{r}_k) is the correlation of the time series \mathbf{w}_k to the original field. With the normalization of data as described above, it is simply $\mathbf{r}_k = \mathbf{S} \cdot \mathbf{w}_k^T$. The TEOF pattern is normalized to have unit length (i.e. so that $\mathbf{r}_k \cdot \mathbf{r}_k^T = 1$) and the k -th TPC is obtained by projecting the normalized k -th TEOF pattern on the original data: $\mathbf{b}_k = \hat{\mathbf{r}}_k^T \cdot \mathbf{S}$, where the i -th element of $\hat{\mathbf{r}}_k$ is:

$$\hat{\mathbf{r}}_k[i] = \frac{\mathbf{r}_k[i] \sqrt{\cos \varphi_i}}{\sqrt{1/n \sum_{j=1}^n \mathbf{r}_k^2[j] \cos \varphi_j}} \quad (4.1)$$

In Eq. 4.1, the φ_i represents the corresponding latitude for the i -th element and the denominator weights the $\hat{\mathbf{r}}_k$ to unit length. For calculating the TPC, we prefer to use the $\hat{\mathbf{r}}_k$ instead of \mathbf{r}_k , where each grid point is weighted by the area it represents. The sets of the TPCs and TEOFs are normalized by dividing the TPC by its standard deviation and multiplying the TEOF by the same number. In this way, the TPC is normalized to unit variance and the TEOF represents the typical variation of the field in its original units, i.e. in the local standard deviation of the field.

The patterns of secondary data written in matrix \mathbf{Z} are optimally related to the patterns from the data in \mathbf{S} as follows. We call the spatial patterns of \mathbf{Z} Akin Trend Empirical Orthogonal Functions (ATEOF) and the corresponding time series Akin Trend Principal Components (ATPC). Let the k -th ATEOF of \mathbf{Z} be written in a column vector \mathbf{p}_k and k -th ATPC in the row vector \mathbf{c}_k . The k -th ATEOF is a map of correlation coefficients between the k -th TPC and field in matrix \mathbf{Z} , which is simply $\mathbf{p}_k = \mathbf{Z} \cdot \mathbf{b}_k^T$. The k -th ATPC is obtained by projecting the weighted k -th ATEOF to the original field $\mathbf{c}_k = \hat{\mathbf{p}}_k \cdot \mathbf{Z}$, where $\hat{\mathbf{p}}_k$ is calculated from \mathbf{p}_k as in Eq. 4.1.

The main aim of this analysis is to estimate the change in the WS from the past to future climate over the North Atlantic and European region, which for the purpose of this paper covers periods of Jan. 1961 to Dec. 2000 and Jan. 2061 - Dec. 2100 respectively. Since the daily near surface wind speed from the most of the GCMs is not available, the climate change of the WS magnitude is estimated from the change in the time series of the low resolution³ SLP modes from the past to the future climate period by statistically ‘reconstructing’ the WS data as:

³With the low resolution we mean the seasonally (3 months) averaged values within a calendar year.

$$\tilde{\mathbf{S}} \approx \sum_{i=1}^K \mathbf{r}_i f(\mathbf{c}'_i) \quad (4.2)$$

where the $\tilde{\mathbf{S}}$ are reconstructed daily WS anomalies and after proper rescaling (multiplying with the standard deviation and adding the annual cycle) leads to the WS, \mathbf{r}_i is the i -th TEOF patterns of WS (obtained from the ECMWF data). The \mathbf{c}'_i represents the i -th low resolution SLP time series of the relevant spatial pattern from GCM obtained with two different methods: i) the projection of the ATEOF of SLP from ECMWF on the SLP anomalies from GCM which were previously interpolated on ECMWF grid; ii) the i -th TEOF of SLP anomalies calculated for each GCM and run separately. As shown later in the paper the second method is also suitable, since the time series of TPC of SLP and TPC of WS show similarities. The summation in Eq. 4.2 goes over the first K dominant modes, which here is simply $K = 1$.

The function f estimates the daily time series of TPC of WS from the low resolution time series of SLP as follows. The low resolution time series of WS is calculated first, by averaging the high resolution TPC within a year. Both low resolution SLP and WS time series are normalized to the unit variance and zero mean in the past climate. The function f first multiplies the normalized time series of SLP with the standard deviation of WS and adds the mean of the WS. Next, the function f statistically reproduce the daily values of WS as follows. The standard deviation of the daily WS within each calendar year for each season separately from the ECMWF is calculated and averaged over all years. The function f reproduce the daily data by calculating normal stochastic time series of WS with the mean of the low resolution time series and the standard deviation from the past climate data. We assumed that the daily WS is normally distributed and that only the mean of the distribution changes from the past to the future time period⁴. When comparing the climate change of the WS the reconstructed WS from the past and from the future time series are compared.

4.3 Trend of wind speed in the past climate

In all seasons, only the first TEOF mode of WS explains a significant part of the trend over selected domain. Since the daily data is used in the study and the WS is highly variable on the daily time step, the first EOF mode of the matrix \mathbf{Q} is able to explain less than 1% of its variance. However, the first mode is significantly separated from the second and further modes (not shown), whose corresponding TPCs do not show a significant trend. Fig. 4.1 shows the first TEOFs of WS, ATEOFs of SLP, first TEOFs of SLP over extended North Atlantic Domain (lat. 30°N-90°N, lon. 120°W-60°E)⁵ and time series corresponding to the patterns linearly fitted to the first TPCs of WS.

In DJF, the first TEOF pattern of WS in its positive state explains the above normal westerly flow south of 65°N and the above normal southerly to easterly flow north of 65°N. The first TEOF pattern of WS is dynamically related to the first ATEOF of SLP which shows the higher than average zonal gradient of SLP over the Northern Atlantic and Europe with the extrema of the SLP anomaly between Greenland and Iceland (minimum) and in the southwestern Europe extending over the southern part of the North Atlantic (maximum). The

⁴This assumption is tested on the ECMWF data as well as on the sample climate model data.

⁵The TEOF of SLP was calculated over the extended Atlantic domain in order to avoid the influence of the Pacific variability on the results.

CHAPTER 4. CLIMATE CHANGE OF WS OVER EUROPE AND NORTH ATLANTIC

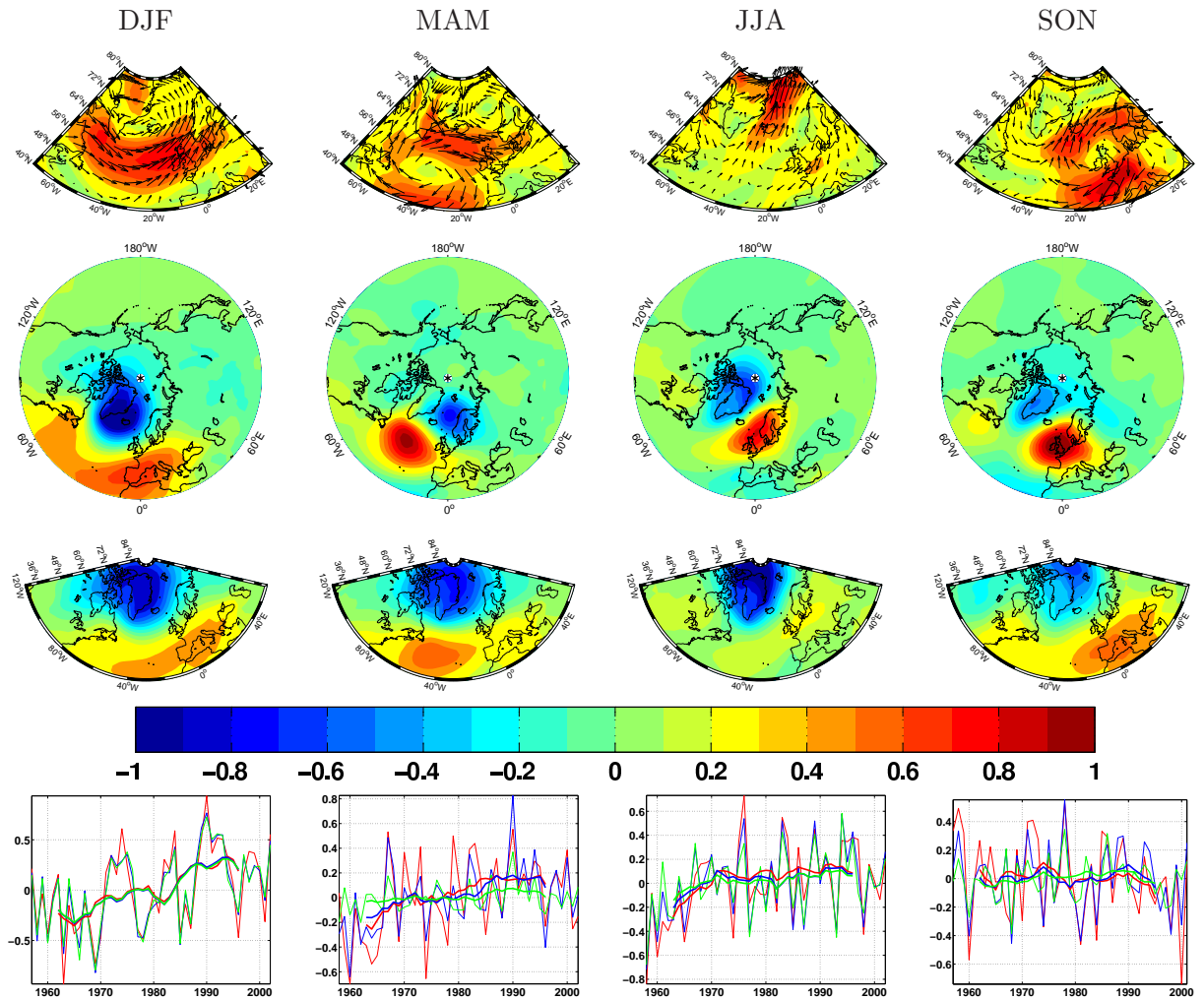


Figure 4.1: First modes from ECMWF data. First row: TEOF modes of WS; second row: ATEOF modes of SLP; third row: TEOF modes of SLP; fourth row: TPC of WS (red lines) and linearly correlated ATPC of SLP (blue lines) and TPCs of SLP (green lines) as a mean yearly values and 11 year running mean averages.

ATEOF patterns of SLP resemble the North Atlantic Oscillation (Marshall et al., 2001). The first ATEOF pattern of SLP is almost identical to the first TEOF pattern of SLP, therefore in DJF the climate change of the WS can be detected by the change of the strength of the first TPC of SLP. In DJF, the first TPC of WS and both ATPC and TPC of SLP have been increasing from early 1960s till mid 1990s therefore the wind speed south (north) of the 65°N was becoming more western (eastern) and the zonal SLP gradient over North Atlantic and Europe have been increasing. The increase of the zonal SLP over the North Atlantic (explained by NAO index) in the second half of the 20th century has been well documented (Marshall et al., 2001). ATPC of SLP is only slightly better correlated to the TPC of WS than the TPC of SLP (Tab. 4.2) and also slightly better explains the long term variability of

4.3. TREND OF WIND SPEED IN THE PAST CLIMATE

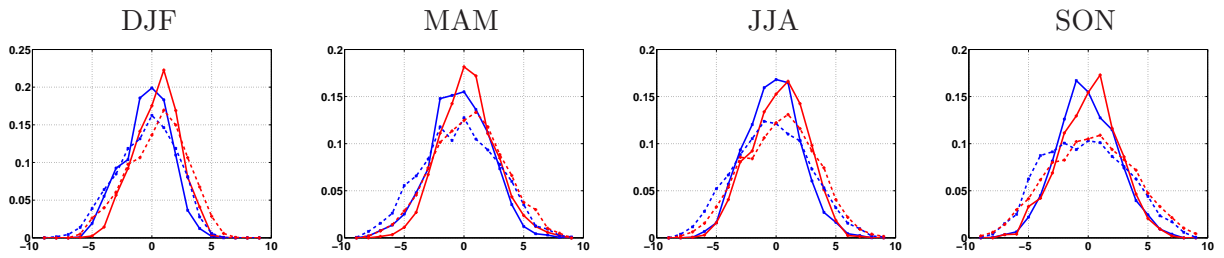


Figure 4.2: Histograms of the TEOF time series of the wind speed (dashed lines) and SLP patterns (solid lines) for earlier period (first 22 years) (red) and recent (second 22 years) (blue) period.

TPC of WS. Around one quarter of the year to year variance of the first TPC of WS can be explained by the simple linear trend (Tab. 4.2). The second TPC of WS is only poorly related to its ATPC of SLP and almost show no linear trend over the studied period (Tab. 4.2) which again indicate that the first TEOF of WS is sufficient for explaining the WS trend.

In MAM, the spatial patterns of WS and the akin SLP are essentially similar to the DJF case, only the location of extreme is displaced. The southern center of ATEOF of SLP pattern is moved considerably northward to around 50°N over the Atlantic, while the Northern center is over the Norwegian Sea. The first TEOF of WS explains above normal westerly winds between 50°N and 60°N and above normal easterly to northerly winds over the North Atlantic south of 50°N . The shape of the first TEOF pattern of SLP is similar to the ATEOF pattern of SLP, although the centres of extrema are displaced. The southern extreme of the TEOF pattern of SLP is at around 10° south of the southern extreme of the ATEOF pattern of SLP, while the northern extreme is above Greenland instead of over the Norwegian Sea. The first TEOF of SLP clearly reflects the NAO pattern. The TPC of WS and ATPC of SLP are well correlated (Tab. 4.2) and have been increasing from the beginning of the period till beginning of 1970s and in the 1980s, while TPC of SLP has a different time dynamics and is thus poorly related to the TPC of WS. In MAM, the small proportion of the TPC of WS can be explained by the linear trend, which is not surprising since its time series are nonlinear function of time.

In JJA, the WS variability explained by the first TEOF is spatially limited mainly to the Norwegian Sea where it is related to above normal south to south-westerly wind and over the north-western Europe related to anomalously north-easterly flow. The akin SLP pattern is above normally high over the Great Britain and north-western Europe and anomalously low over Scandinavia. The first TEOF of SLP is basically the same as the akin SLP pattern and similarly as in DJF representing the zonal SLP gradient but with the southern center shifted significantly northward. The displacement of the southern center of the zonal SLP toward the north in the warm period of the year is consistent with the findings of Ogi et al. (2004). Both the time series of the SLP are well correlated to the first TPC of WS and have been strongly increasing from the beginning of the period till early 1970s and slightly thereafter. In JJA, relatively high proportion of the variance of TPC of WS can be explained by linear trend showing the persistent increase of TPC throughout the ECMWF period.

In SON, the first TEOF pattern of WS explains above normal westerly (easterly) flow

	Pattern 1			Pattern 2	
	<i>exp.var.</i>	<i>ccATPC</i>	<i>ccTPC</i>	<i>exp.var.</i>	<i>ccTPC</i>
DJF	0.25	0.872	0.768	0.11	0.527
MAM	0.18	0.740	0.458	0.017	0.575
JJA	0.31	0.823	0.754	0.02	0.9067
SON	0.094	0.750	0.320	0.058	0.565

Table 4.2: Explained variance (*exp.var.*) of the first two TPC of WSs by the linear trend and the correlation coefficient between the first two TPCs of WS and ATPC of SLP (*ccATPC*) and the first TPC of WS and TPC of SLP (*ccTPC*). All measures are calculated on the mean yearly data.

north (south) of Great Britain which is related to the dipole of SLP with the minima over Greenland and maxima over the northern part of Great Britain. The TEOF pattern of SLP is similar to the NAO pattern, whereas its southern center is significantly south of the southern center of the ATEOF pattern of the SLP. The TPC of WS and related SLP patterns show the long term variability, but almost no long term trend. The TPC of SLP is poorly correlated to the TPC of WS which is due to the different position of the southern maxima in those two patterns.

As discussed earlier, the WS magnitude is a nonlinear function of the TPC of WS which also depends on the local values of the standard deviation and the mean of the WS, therefore from the climate change of the TPC, the change of the WS magnitude is not immediately obvious. For example, in the DJF season, the mean wind speed is westerly to southwesterly over most of the North Atlantic and European domain (not shown). An increase of the higher percentiles of the TPC distribution leads to an increase in the magnitude of the westerly WS between 45°N and 65°N. However, the lower percentiles of the TPC distribution are related to the easterly flow and the increase of the lower percentiles of TPC of WS leads to the decrease of the easterly WS magnitude. Therefore to characterize the climate change of the WS magnitude, the change of the whole distribution of TPC of WS must be known. Fig. 4.2 compares the distributions of the daily TPC for all seasons from the earlier 22 years to the latest 22 years of the ECMWF period. In all seasons and specifically in DJF and JJA, the shift of the TPC of WS distribution toward the highest mean value can be seen in the recent compared to the earliest part of the period. In all seasons, the shape of the TPC distribution has not changed (according to the Kolmogorov-Smirnov test at 5% significance level) and is also not significantly different from the normal distribution except in DJF.

The WS trend can be considerably better captured by the TEOF patterns compared to the EOF patterns of WS. As an example, the first four EOF modes of WS and akin SLP patterns in DJF are shown on Fig. 4.3, where the akin patterns were computed similarly to the akin TEOF patterns (see Sec. 4.2). The first EOF pattern is in its positive (negative) phase related to the blocking (low) west of the Great Britain and the anticyclonic (cyclonic) WS circulation around the maxima (minima) of SLP. In the positive phase, the maxima of SLP from the first akin EOF pattern of SLP is consistent with the area of the most frequent blocking occurrence over the Atlantic (Scherrer et al., 2006). The second EOF pattern of WS show in its positive phase anomalously southerly wind in the north-east Atlantic and northerly in the north-west Atlantic and is related to the SLP between Scandinavia and north-western

4.4. WS IN THE PAST AND FUTURE CLIMATE FROM ECHAM5/MPI-OM MODEL

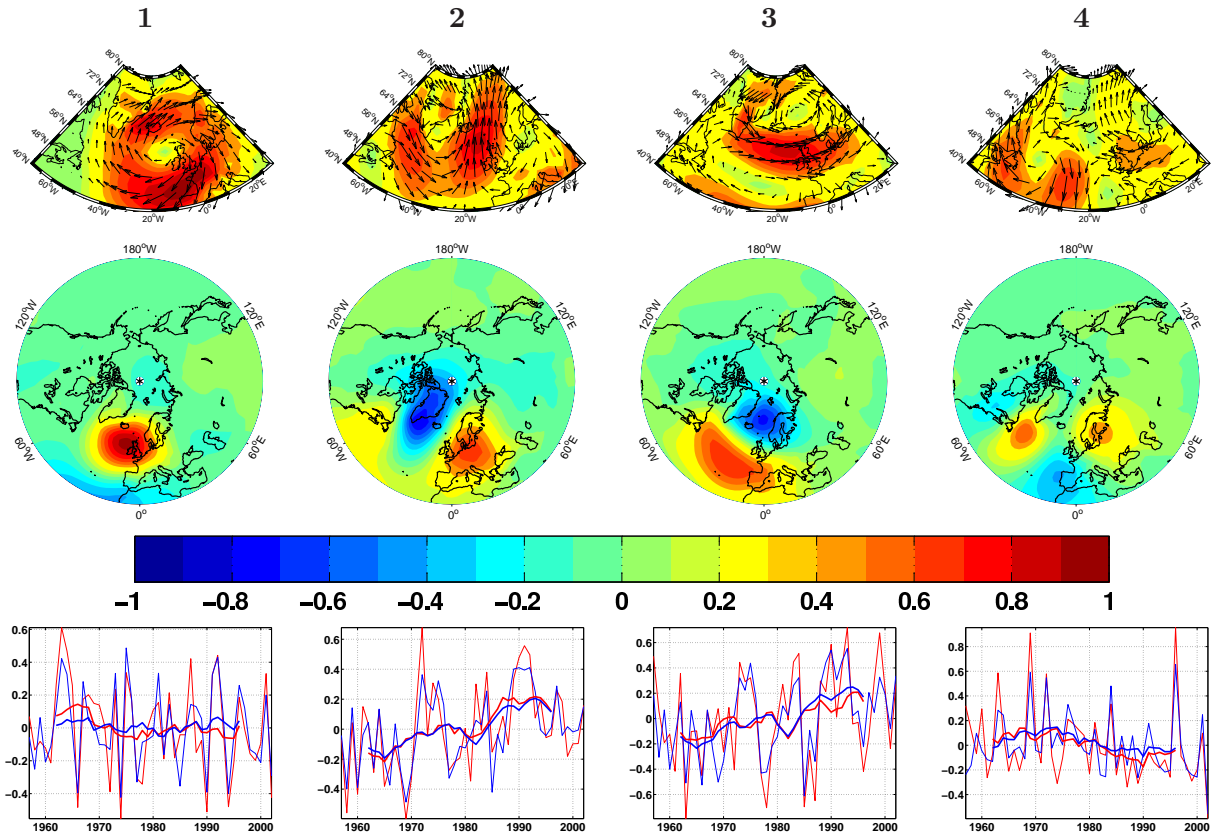


Figure 4.3: ECMWF data. First EOFs of WS (first row), related SLP patterns (second row), TPC of WS (red lines) and regressed time series of the SLP patterns (blue lines) as a yearly values and 11 year running mean values (third row) and the first TEOF patterns of the SLP.

Europe. The third EOF pattern of the WS and akin SLP is similar to the first TEOF pattern of WS and first ATEOF pattern of SLP. The linear trend explains 0.13 year-to-year variability of the second PC of WS, and 0.06 variability of the third PC, while it cannot explain the significant part of the variability of the first and fourth PC.

4.4 WS in the past and future climate from ECHAM5/MPI-OM model

The TEOF modes of WS and related SLP patterns from the ECHAM5/MPI-OM calculated from the whole available period (1981-2000, 2046-2065 and 2081-2100) are shown in Fig. 4.4. As in case of the ECMWF data modes, in all seasons only the first TEOF modes of WS are sufficient to explain the significant part of the spatially coherent trend of the WS over the North Atlantic European region. The TEOF and related ATEOF patterns of WS and SLP as well as TEOF patterns of SLP are similar to the ones obtained from the ECMWF data, the differences are discussed below.

In DJF, the TEOF pattern of WS and ATEOF of SLP from ECHAM5/MPI-OM are al-

Season	cc. ATEOF	cc. TEOF
DJF	0.865	0.542
MAM	0.781	0.693
JJA	0.907	0.838
SON	0.904	0.837

Table 4.3: The correlation coefficients of the yearly TPC of WS with the ATPC of SLP and TPC of SLP from ECHAM5/MPI-OM data.

most identical to the ones obtained from ECMWF data, although the location of the southern center of SLP and the wind pattern has moved southwards and the southern center of SLP is weaker compared to the one from the ECMWF patterns. In MAM, the shape of the WS pattern from ECHAM5/MPI-OM is similar to the one from ECMWF, but it is moved around 10° westwards, as is also in the case of the southern center of the ATEOF of SLP. In MAM, TEOF and ATEOF patterns of SLP are almost identical which was not the case from the ECMWF data. Therefore the TPC of SLP is well able to describe the variability of the TPC from WS, which is indicated by the higher correlation coefficient between the two time series. In JJA, the TEOF patterns from ECMWF and ECHAM5/MPI-OM are relatively different. The southern center of the WS pattern is stronger and the northern center has moved southwards compared to in the ECMWF case. The TEOF of SLP has a maxima of the southern center over the eastern USA. In SON, there is almost no difference between ECMWF and ECHAM5/MPI-OM modes. In all seasons, the southern centres of the SLP in ECHAM5/MPI-OM TEOF patterns are weaker compared to the southern centres from ECMWF data. The patterns from the ECMWF show more inter-seasonal variability compared to the ones from the ECHAM5/MPI-OM. The correlation coefficients between the first TPCs of WS and the ATPCs of WS as well as to the TPCs of SLP are in all seasons in the same range than the ones from ECMWF. The similarity of the patterns between the ECMWF and ECHAM5/MPI-OM gives the confidence that the TEOF patterns are stable regarding the period and dataset used and well represent the trend of the data in the past as well as in the future climate.

The distribution of the TPC of WS in all seasons except MAM do not significantly change from the past to both future periods (20046 – 2065 and 2081 – 2100) (Fig. 4.4, lowest row) and is not significantly different from the normal distribution, based on the Kolmogorov-Smirnov test at 5% confidence level. Therefore, the estimation of the daily WS by assuming the normal distribution of the TPC as explained in Sec. 4.2 is justified.

To test the method developed for detecting the climate change, the change of the mean WS between the past (1961-2000) and future (2081-2100) climate calculated from the difference of the mean WS from ECHAM5/MPI-OM and the difference of the reconstructed WS from the change of the first ATPC of SLP as explained in Sec. 4.2 are compared (Fig. 4.5). In DJF, the reconstructed WS magnitude increased in the future climate in the southern part of the domain (from around 50°N to 60°N) centred over the Atlantic and approximately agrees with the increase of the WS magnitude. However, the increase of the WS magnitude is confined to the smaller geographical area. The change in reconstructed WS underestimates the decrease of the WS magnitude in the northern part of the domain. In MAM, the reconstructed WS shows only a minor change in magnitude in the future climate with a slight increase over the North Atlantic at around 50° and a decrease southern and northern parts, while the WS

4.5. FUTURE CHANGE OF THE NORTH ATLANTIC AND EUROPEAN WIND SPEED

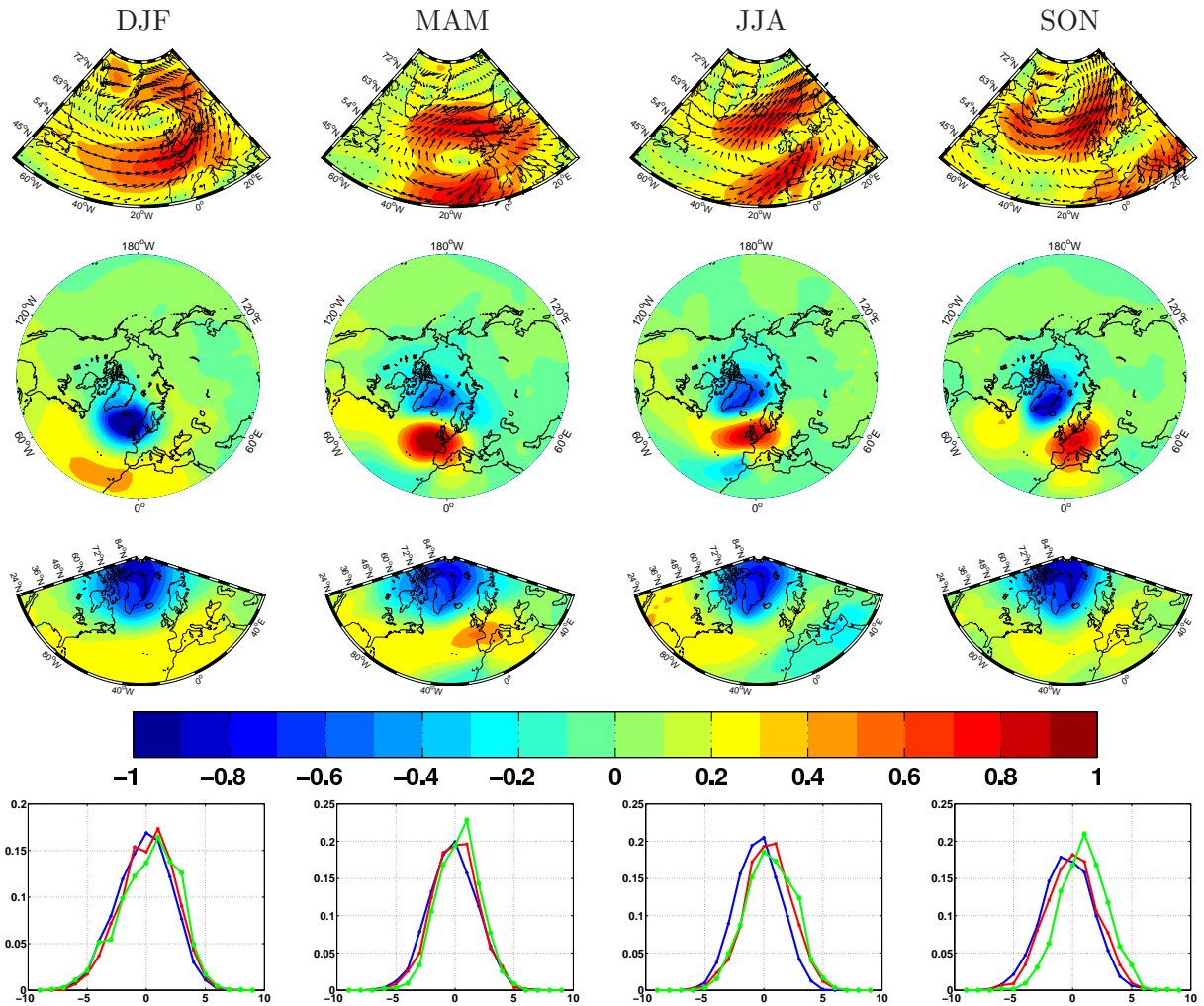


Figure 4.4: First modes from ECHAM5/MPI-OM data. First row: TEOF modes of WS; second row: ATEOF modes of SLP; third row: TEOF modes of SLP; fourth row: the probability density of TPC of WS for period 1961-2000 (blue), 2045-2065 (red) and 2081-2100 (green).

from the ECHAM5/MPI-OM show decrease over most of the domain. In JJA and SON, the reconstructed WS change indicates an increase in magnitude over the northern part and a decrease over the southern part of the domain. A similar change is observed in the WS although the location of the maxima and minima are not at exactly the same place.

4.5 Future change of the North Atlantic and European wind speed

The time series of the monthly SLP obtained from the GCMs and related to climate change of the WS are constructed by i) projecting ATEOF of SLP from ECMWF on the monthly SLP anomalies from the GCMs (Fig. 4.6), termed as the Projected Principal Components (PPC), and ii) as the first TPCs of the monthly SLP anomalies calculated for each GCM

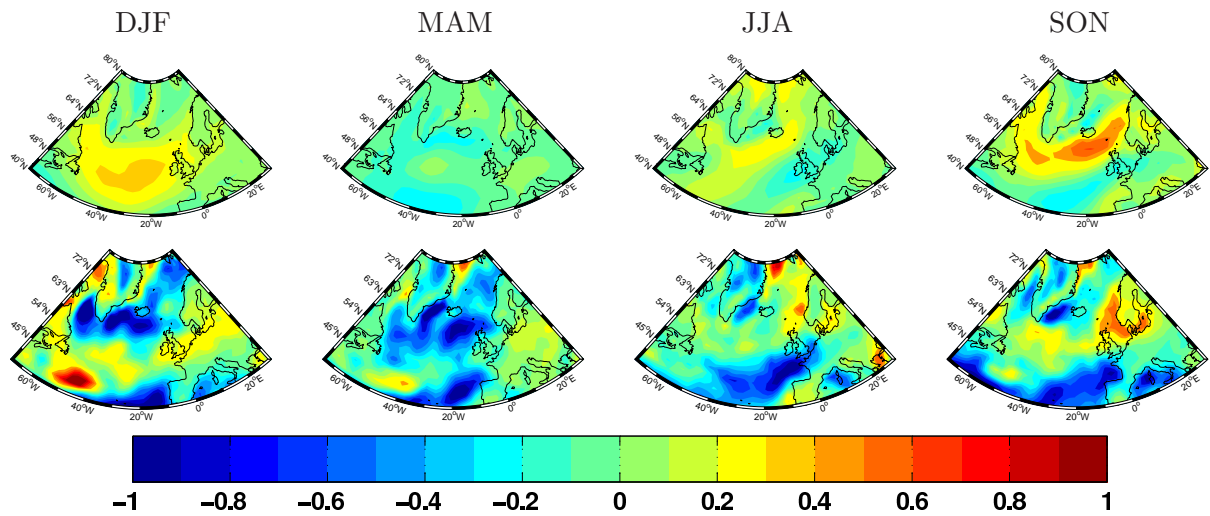


Figure 4.5: Difference between mean WS magnitude (in m s^{-1}) from the future (2081-2100) and past (1981-2000) climate reconstructed from the change of the first ATPC of SLP (top row) and directly from the ECHAM5/MPI-OM WS (bottom row).

run separately (Fig. 4.7). All time series (PTS and TPC) are normalized to the unit year to year variance and zero mean in the past climate. The first and the third row in Figs. 4.6 and 4.7 show the 15 year averaged time series for each GCM and run separately and the second and fourth row, the 9 year running model-mean values, as well as the values between 10th and 90th percentile of the 9 year running mean time series. The 10th and 90th percentile are interpreted as the limiting values of the time series. The historic data from ECMWF reanalysis and the HadSLP2 are also plotted. Since the TEOFs and thus TPCs are invariant to the sign of the pattern, we chose the sign of the TPCs from GCM so that the correlation coefficient between the TEOFs from GCM and from ECMWF is positive.

In all seasons, the time series from ECMWF and HadSLP2 in common time period agree very well among each other. The slight difference between the TPC from ECMWF and HadSLP2 is only in JJA. In the second part of the 19th century and in the whole 20th century all time series (PPCs and TPCs) from GCMs in all seasons show relatively constant variability and almost no trend. The time series of the ECMWF and HadSLP2 show considerable interdecadal variability which in most seasons exceeds the values from GCMs (10th and 90th percentile). The reason for the difference is different properties of the time series. In the past period, the time series from GCMs show random from year-to-year uncorrelated departures from the mean values while the time series from HadSLP2 show a decades of the positive and negative anomalies. Therefore, the time series from HadSLP2 are significantly autocorrelated at the time lag of one and in some seasons even higher time lags, while this is not the case for the majority of the time series from GCMs. Fig 4.8. shows the example for the autocorrelation function of the PPC in DJF for the HadSLP2 and mean GCMs as well as 10th and 90th percentile values from GCMs.

In all seasons of the 21st century climate, the time series from almost all GCMs are increasing, indicating the increase of nearly zonal SLP gradient. The time series from one of the

4.5. FUTURE CHANGE OF THE NORTH ATLANTIC AND EUROPEAN WIND SPEED

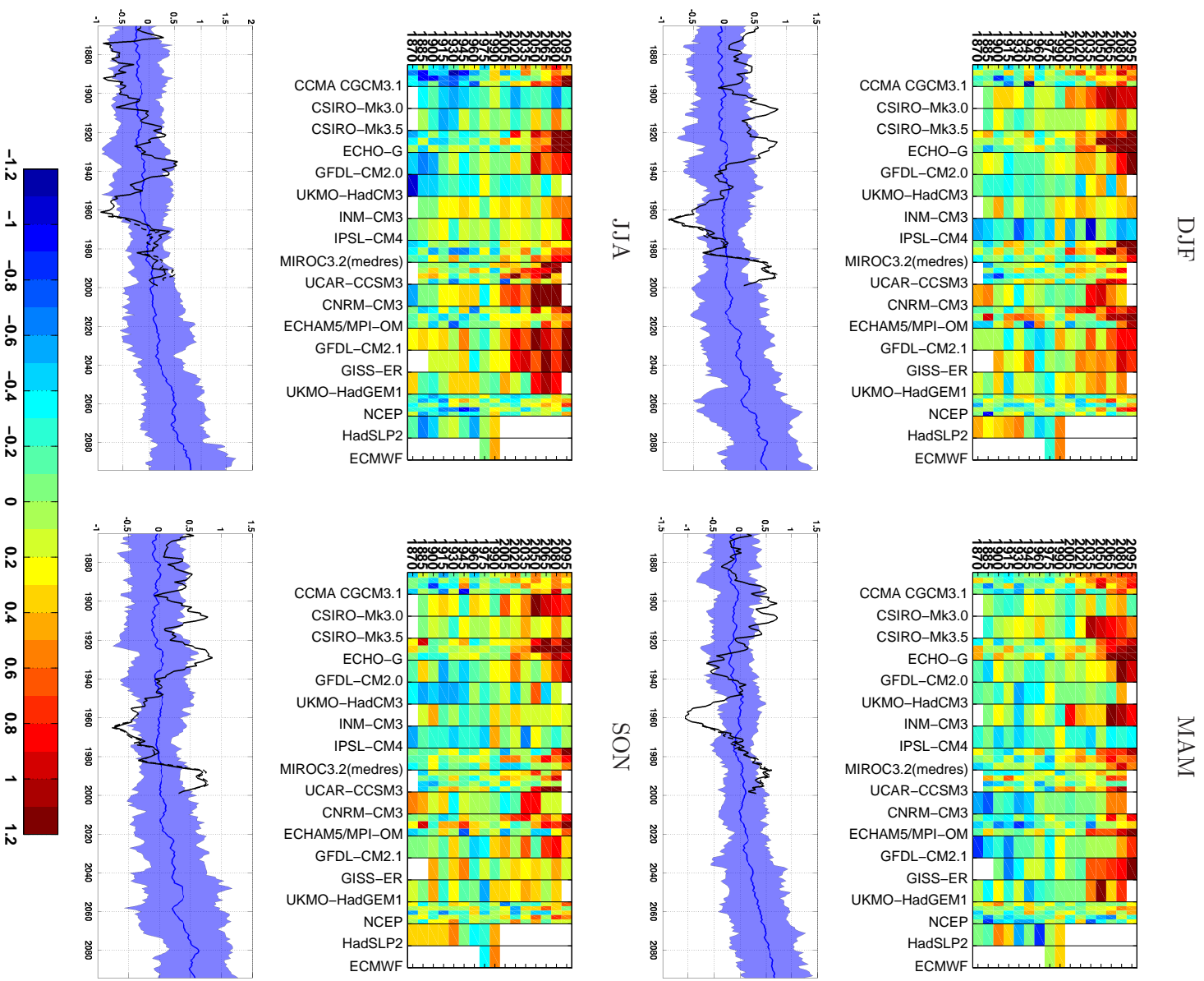


Figure 4.6: Time series of the PTS for all data as a decadal variability for each model separately (first and the third rows). second and the fourth rows: the GCM 9 year averaged mean variability (blue line), the area covered the 10th and 90th percentile (blue area), the HadSLP2 (black solid line) and, ECMWF (black dashed line).

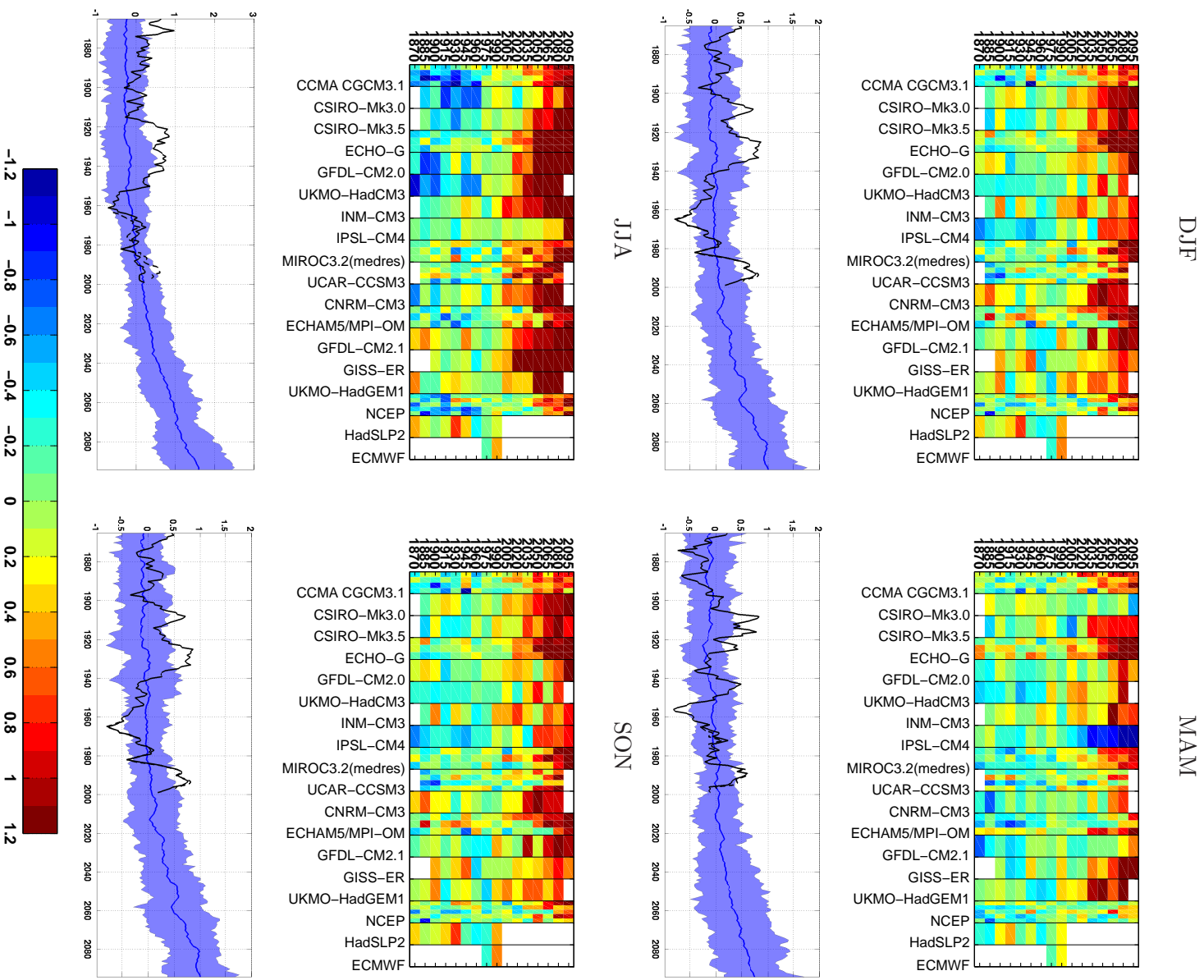


Figure 4.7: Same as in 4.6, only TPC instead of PTS.

4.5. FUTURE CHANGE OF THE NORTH ATLANTIC AND EUROPEAN WIND SPEED

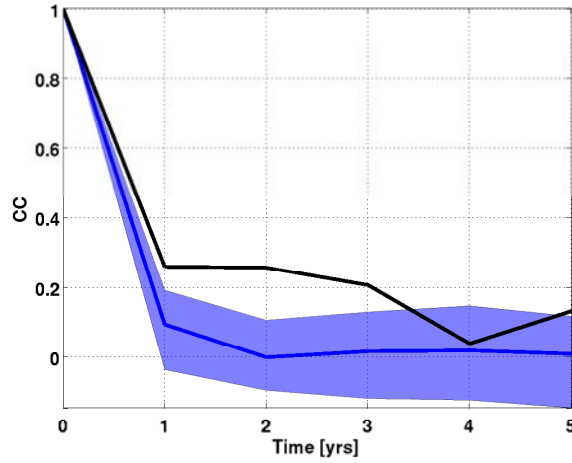


Figure 4.8: Autocorrelation for the PPC in DJF. Blue line: GCM average, blue area covers the 10th to 90th percentile of autocorrelation from GCMs, black line HadSLP2. The autocorrelation higher than 0.2 is significant at 1% confidence level.

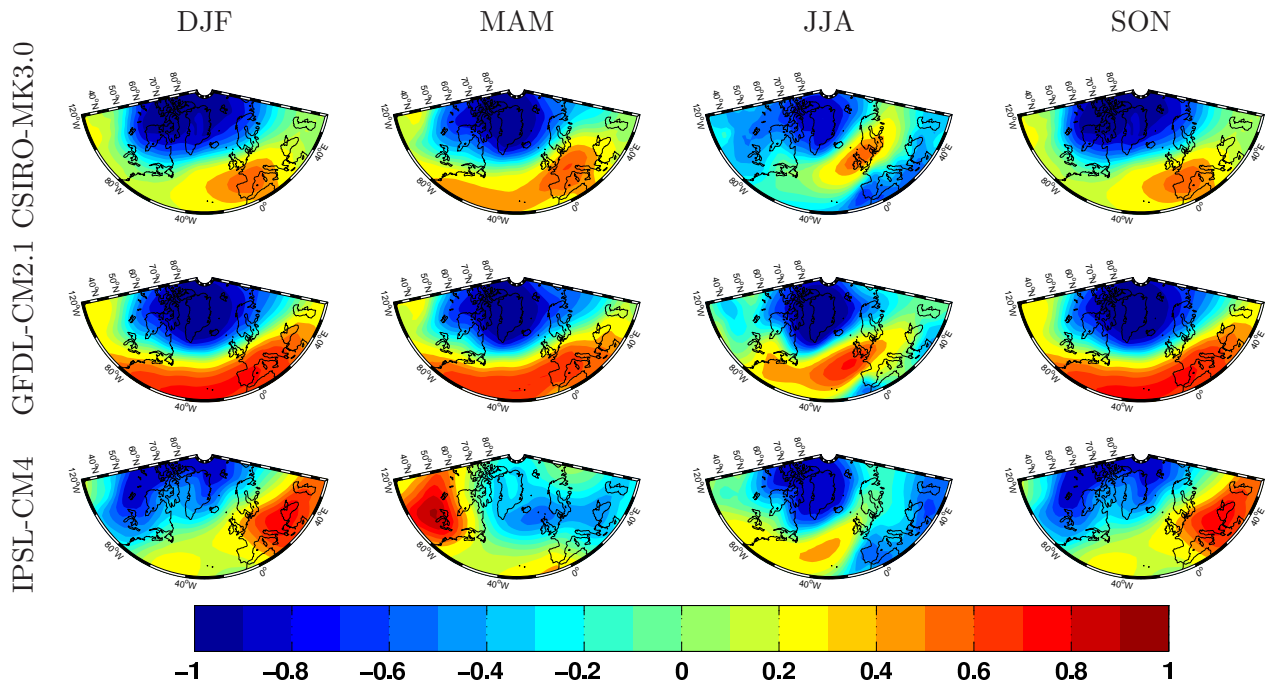


Figure 4.9: Sample TEOF patterns from the climate models: CSIRO-Mk3.5 (top row), GFDL-CM2.1 (middle row) and IPSL-CM4 (bottom row).

CHAPTER 4. CLIMATE CHANGE OF WS OVER EUROPE AND NORTH ATLANTIC

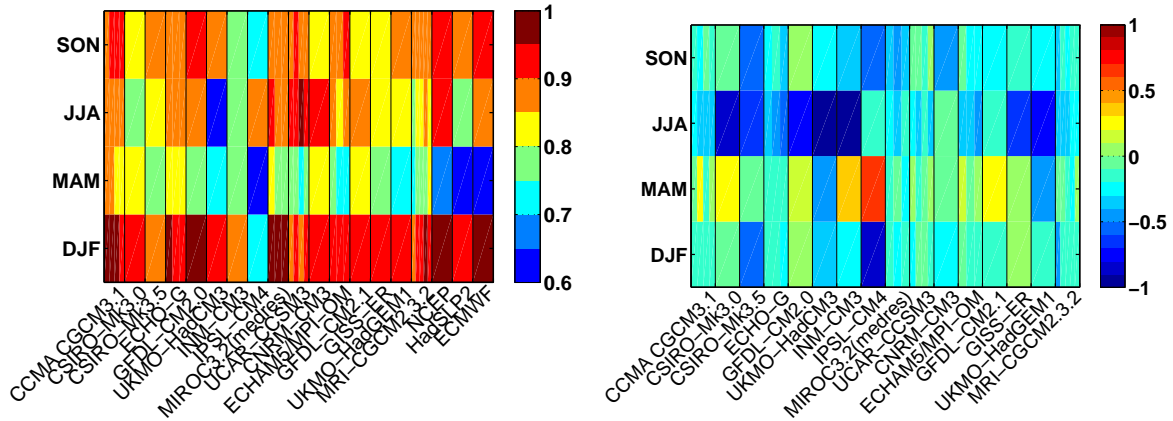


Figure 4.10: The correlation coefficient between the yearly TPC and PTS data (left) and the difference of the PTS and TPC in the 21st century and 20th century (right).

GCM, namely IPSL-CM4 is strikingly different than from the others. It shows the decrease of the 21st century PTS in DJF and MAM. In order to investigate the difference between the PTSs from IPSL-CM4 and other models, the TEOF patterns of SLP from three sample models are plotted on Fig. 4.9. The TEOF patterns from most of the models show the zonal SLP gradient whose southern center is in the warm part of the year usually displaced northwards. The zonal SLP from most of the models can be interpreted as the Arctic Oscillation, as for the example in the GFDL-CM2.1, while from some of the models it clearly shows the North Atlantic Oscillation such as in CSIRO-Mk3.0. The TEOF of IPSL-CM4 shows almost meridionally oriented dipole of SLP instead of the zonal. Therefore, its TPC is also considerably different from the time series of other models.

The PTSs and TPCs are relatively well correlated in all seasons except MAM (Fig. 4.10, left). However, the TPCs show considerably higher trend than the PTSs. This is not surprising result. The TEOFs are able to optimally find the patterns so that corresponding TPCs explain the highest trend of the data and the TEOFs and TPCs are adjusted to each model separately and account for possible displacements of the patterns in each model.

Since the multiple model runs are available, the reliability of climate change for the WS between the future climate (2061-2100) and the past climate (1961-2000) can be estimated. As the most probable change in the mean speed, the mean expected change of the WS magnitude in the future climate are the reconstructed from the TPC and PPC averaged over all models. The upper limit of the WS change was estimated as the 90th percentile of the WS change reconstructed from the TPC. TPC was chosen as a upper limit since it shows higher increase than PPC in the future climate. The minimum change of the WS was estimated as a 10th percentile of the WS reconstructed from the PPC since PPCs show smaller trend than TPCs. The climate change of the WS is shown on Fig. 4.11.

In DJF, the clear signal of the increase of the WS magnitude over the Atlantic is found. The maximum increase of the WS in the future climate is expected to be between 0.5 m s^{-1} and 2.5 m s^{-1} over the central Northern Atlantic. In MAM, climate change of the WS is the expected to be small and not very consistent among the models. The WS is expected to increase over the Atlantic at latitude of around 55°N and decrease in south and western

4.5. FUTURE CHANGE OF THE NORTH ATLANTIC AND EUROPEAN WIND SPEED

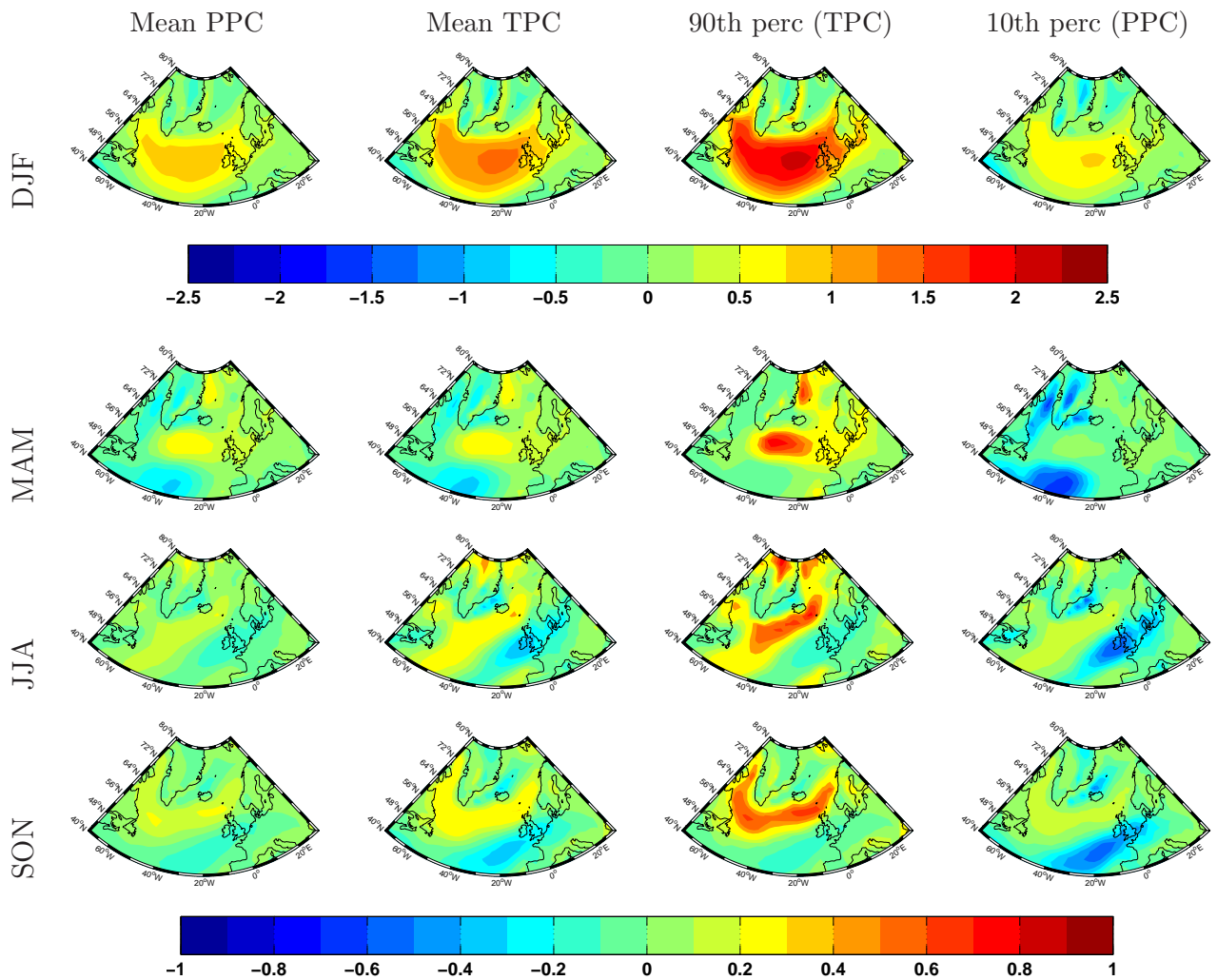


Figure 4.11: The change of the mean WS from past (1961-2000) to future (2061-2100) climate. First column: the GCM mean change derived from PPC, second column: GCM mean change derived from TPC, third column: 90th percentile of WS change derived from TPC and fourth column: 10th percentile WS change estimated from the PPC.

part of the domain. The expected change of the WS is smaller than 1 m s^{-1} . In JJA and SON, the climate change of the WS is also below 1 m s^{-1} and is expected to increase over the northern to north-western part of the North Atlantic and decrease over the south-eastern part of the North Atlantic and over north-western Europe.

4.6 Discussion and conclusions

The aim of the work was to quantify the change of the near surface wind speed (at 10 meters height, WS) over the North Atlantic and Europe in the 21st century under IPCC SRES A2 greenhouse gas scenario. From the 45 years of the ECMWF reanalysis, the WS patterns explaining the dominant part of the spatially coherent trend were found. The dominant WS patterns were defined as Trend Empirical Orthogonal Functions (TEOFs). The TEOFs are not well suited for isolating the local trends but this limitation of TEOFs is not the drawback of our study, since the climate change of the WS over the Northern Europe mainly depend on the large scale forcings (Räisänen et al., 2004) while the regional WS changes play secondary role and is also not well resolved by the GCMs. The dominant WS patterns were optimally related to the SLP patterns with the goal to investigate the climate change of WS from the climate change of the relevant SLP patterns. The climate change of the WS between the past (1961-2000) and future (2061-2100) climate was investigated from the SLP as simulated by the ensemble of 16 GCMs, where for each GCM one to four simulations based on perturbed initial conditions were available. Although the GCMs are not independent, due to partly common development, the simulated SLP from ensemble of GCMs were used to estimate the reliability of the climate change of the WS. The assumption used to derive the climate change of the WS is that the dominant climate modes which describe the trend in the past WS data remain the most important also in the future climate and leads to the climate change. The first attempt to define the WS patterns was based on the Empirical Orthogonal Functions (EOFs). However, the EOFs are not suited to isolate the trend of the data, therefore the most significant part of the WS trend is spread over many EOFs.

For all seasons, only the first TEOFs of WS are sufficient to explain the significant part of the spatially coherent WS trend. The second and further TEOF patterns exhibit significantly weaker trend and are in most seasons poorly related to the corresponding SLP pattern. Therefore to estimate the WS change, only the first TEOF patterns of WS were considered. The first TEOFs of WS explain nearly zonal WS variability over the North Atlantic and Europe, while the exact location of the WS magnitude is seasonally dependent. In DJF, the WS from the first TEOF is variable over most of the North Atlantic and European domain, and is related to zonal SLP gradient over Atlantic and Europe, which essentially represent the North Atlantic Oscillation (NAO). In the warmer part of the year, the WS pattern is spatially isolated to a smaller extend and displaced northward, while in the southern part of the domain the wind has nearly easterly direction. The smallest and the most northern extend of the WS is found in JJA. The shift of the WS pattern toward north is partially explained by the northward movement of the southern center of NAO dipole in the warm part of the year. Similar shift of the southern center of zonal SLP gradient over the northern Europe toward north has been documented by Ogi et al. (2004). Although the SLP patterns related to WS partially resemble NAO, in most seasons they are locally restricted to smaller region. Especially in MAM, the akin SLP pattern does not well resemble NAO.

The change of the WS from the past to the future climate was statistically reconstructed

from the change of the strength (i.e. time series) of the relevant SLP patterns. Still some uncertainties exist regarding to the best SLP patterns from GCMs related to WS change, since the exact location of the WS as well as SLP patterns is dependent on the model. Therefore to account for the uncertainties of the best SLP patterns, two sets of the relevant time series were computed from each GCM by projecting the SLP patterns related to WS from ECMWF on GCM anomalies and by computing the first Trend Principal Component (TPC) from each GCM run separately. As expected, the TPCs show higher trend as the projected time series, since the TPCs are designed to find SLP trend more efficiently. Most of the models show consistent variation of the relevant time series, with almost no trend in the second half of the 19th and in 20th century and the increase of the time series in the 21st century, representing the increase of the nearly westerly wind over most of the domain in DJF and increase of the westerly wind over northern part of the domain and easterly over southern part of the domain in the warmer part of the year. The exact location of the WS change depends on the season and is defined by the first TEOF of WS. However, compared to the measurement and reanalysis data, the time series from the second half of the 19th and 20th century data do not agree in their inter-annual variability. The measured time series have more pronounced intra-annual variability which can be seen by higher autocorrelation on the yearly to few yearly time step, while the time series from GCM almost no inter-annual variability. Too low variability of the NAO Index (NAOI) from GCMs, which is strongly related to the time series explaining WS has been already noted (Osborn, 2004; Gillett et al., 2003; Miller et al., 2006).

The strongest climate signal of the WS change was observed in the DJF, where the increase of the WS magnitude up to between 0.5 m s^{-1} and 2.5 m s^{-1} in its maximum over the northern Atlantic is expected. In other seasons the climate change of the WS is less pronounced. The WS is expected to increase over the north west part of the domain up to the 1 m s^{-1} and decrease over the south-east part of the domain also for around 1 m s^{-1} . Contrary to the analysis of the Räisänen et al. (2004) and Pryor et al. (2006), we observed a significant increase of the WS over the North Atlantic and Europe in DJF, while in the other seasons the change of the WS is smaller. The work presented in this paper qualitatively estimates the WS change over North Atlantic and Europe in the future climate as well as estimates the reliability of the climate change of the WS. The dynamical downscaling of the GCM would be desired to account for the additional local influence on the WS change, such as the change of the surface stability. However, when interpreting dynamically downscaled GCM results, it should be clear that the WS change crucially depends on the large scale forcing from the GCMs.

Acknowledgements

The data used in this study was obtained from European Centre for Medium-Range Weather Forecasts, Hadley Centre for Climate Prediction and Research and the World Climate Research Programme's Coupled Model Intercomparison Project phase 3 multi-model dataset. The work was supported by the European Union Marie-Curie Early Stage Researcher Program Modobs (MRTN-CT-2005-019369).

Bibliography

- Alexandersson, H., H. Tuomenvirta, T. Schmith, and K. Iden, 2000: Trends of storms in NW Europe derived from an updated pressure data set. *Climate R.*, **14**, 71–73.
- Allan, R. J. and T. J. Ansell, 2006: A new globally complete monthly historical mean sea level pressure data set (hadslp2): 1850-2004. *J. Climate*, **19**, 5816–5842.
- Blessing, S., K. Fraedrich, M. Junge, T. Kunz, and F. Lunkeit, 2005: Daily North-Atlantic Oscillation (NAO) index: Statistics and its stratospheric polar vortex dependence. *Meteorol. Z.*, **14** (6), 763–769.
- Christensen, J. H., et al., 2007: *Climate Change 2007: The Physical Science Basis. Contribution of Working Group I to the Fourth Assessment Report of the Intergovernmental Panel on Climate Change*, chap. Regional Climate Projections. Cambridge University Press, Cambridge.
- Corti, S., F. Molteni, and T. N. Palmer, 1999: Signature of recent climate change in frequencies of natural atmospheric circulation regimes. *Nature*, **398**, 799–802.
- Gillett, N. P., F. W. Zwiers, A. J. Weaver, and P. A. Stott, 2003: Detection of human influence on sea-level pressure. *Nature*, **422**, 292–294.
- Hannachi, A., 2007: Pattern hunting in climate: a new method for finding trends in gridded climate data. *Int. J. Climatol.*, **27**, 1–15.
- Marshall, J., et al., 2001: North Atlantic climate variability: Phenomena, impacts and mechanisms. *Int. J. Climatol.*, **21**.
- Miller, R. L., G. A. Schmidt, and D. T. Shindell, 2006: Forced annular variations in the 20th century Intergovernmental Panel on Climate Change fourth assessment report models. *J. Geophys. Res.*, **111**, D18 101.
- Ogi, M., K. Yamazaki, and Y. Tachibana, 2004: The summertime annular mode in the Northern Hemisphere and its linkage to the winter mode. *J. Geophys. Res.*, **109**, D20 114.
- Osborn, T. J., 2004: Simulating the winter North Atlantic Oscillation: the roles of internal variability and greenhouse gas forcing. *Clim. Dynam.*, **22** (605–623).
- Pryor, S. C. and R. J. Barthelmie, 2003: Long-term trends in near-surface flow over Baltic. *Int. J. Climatol.*, **23**, 271–289.
- Pryor, S. C., R. J. Barthelmie, and E. Kjellström, 2005: Potential climate change impact on wind energy resource in northern Europe: analyses using regional climate model. *Clim. Dynam.*, **25**, 815–835.
- Pryor, S. C., J. T. Schoof, and R. J. Barthelmie, 2006: Winds of change? Projections of near-surface winds under climate change scenarios. *Geophys. Res. Lett.*, **L11702** 10.1029/2006GL026000.
- Räsänen, J., et al., 2004: European climate in the late twenty-first century: regional simulations with two driving global models and forcing scenarios. *Clim. Dynam.*, **22**, 13–31.

BIBLIOGRAPHY

- Scaife, A. A., J. R. Knight, G. K. Vallis, and C. K. Folland, 2005: A stratospheric influence on the winter NAO and North Atlantic surface climate. *Geophys. Res. Lett.*, L18715.
- Scherrer, S., M. Croci-Maspoli, C. Schwierz, and C. Appenzeller, 2006: Two dimensional indices of atmospheric blocking and their statistical relationship with winter climate patterns in the Euro-Atlantic region. *Int. J. Climatol.*, **26**, 233–249.
- Schwierz, C., C. Appenzeller, H. C. Davies, M. Linger, W. Müller, T. F. Stocker, and M. Yoshimori, 2006: Challenges posed by and approaches to study of seasonal-to-decadal climate variability. *Climatic Change*, **79**, 31–63.
- Sigmond, M. J., J. F. Scinocca, and P. J. Kushner, 2008: Impact of the stratosphere on tropospheric climate change. *Geophys. Res. Lett.*, **35** (L12706).
- Trigo, R. M., T. J. Osborn, and J. M. Corte-Real, 2002: The North Atlantic Oscillation influence on Europe: Climate impacts and associated physical mechanisms. *Climate R.*, **20**, 9–17.
- Uppala, S. M., et al., 2005: The ERA-40 re-analysis. *Q. J. R. Meteorol. Soc.*, **131** (612), 2961 – 3012.
- van Oldenburgh, G. J. and A. van Ulden, 2003: On the relationship between global warming, local warming in the Netherlands and changes in circulation in the 20th century. *Int. J. Climatol.*, **23**, 1711–1724.
- van Ulden, A. P. and G. J. van Oldenborgh, 2006: Large-scale atmospheric circulation biases and changes in global climate model simulations and their importance for climate change in Central Europe. *Atmos. Chem. Phys.*, **6**, 863–881.
- von Storch, H. and F. W. Zwiers, 1999: *Statistical analysis in climatology*. Cambridge, Cambridge Univ. Press.

5

Improving Mellor-Yamada-Janjić parameterization for the wind conditions in the Marine Planetary Boundary Layer[†]

Abstract

The structure of the lower part of the Marine Planetary Boundary Layer (MPBL) is relevant not only for climate and numerical weather prediction simulations but also for commercial applications such as offshore wind energy harvesting. A proper description of the turbulence is crucial for accurate simulations of the wind field properties such as the mean wind speed, turbulent fluxes and especially the vertical wind profile. In this study, the Mellor-Yamada-Janjić (MYJ) boundary and surface layer parameterization within the Weather Research and Forecasting Model (WRF) was improved by redefining the Master Length Scale (MLS), which controls the diffusion and dissipation of the turbulent fluxes as well as the pressure-temperature and pressure-strain covariances. In the surface layer, the modified MLS is dependent on the surface stability. In the boundary layer, the surface stability correction of the MLS is included which has the strongest influence close to the surface. The non-local effects in the stable boundary layer based on surface heat forcing are also included. The Single Column Model studies were performed to compute the changes of the wind field properties due to the change in the formulation of the MLS. The three dimensional version of the model was then used to downscale some real cases and compare them with the measurements. Improvements in the simulations of the wind shear in the lower part of the boundary layer (up to around 30 m) with the new parameterization have been shown, while its impact higher in the MPBL is less pronounced. On the other hand, the simulated wind speed is only slightly modified by the new approach.

5.1 Introduction

Planetary Boundary Layer (PBL) is characterized by enhanced turbulence influencing larger scale atmospheric motions by increase of the vertical mixing. The effect of the turbulence is not explicitly resolved in the atmospheric mesoscale models but parameterized in terms of larger scale mean quantities. For some applications, such as in wind energy, pollution studies,

[†]The work presented in this chapter is under review for publication in *Boundary Layer Meteorology* as: Kay Sušelj, Abha Sood: *Improving Mellor-Yamada-Janjić parameterization for the wind conditions in the Marine Planetary Boundary Layer.*

air traffic, etc., where the near surface atmospheric conditions are the most relevant, the accurate parameterization of the PBL structure is the critical part of the mesoscale model.

Turbulence parameterizations of different complexities were proposed in the literature. Example of the simple first order closure model is described by Hong and Pan (1996). A family of popular models, based on the second order closure was introduced by Mellor and Yamada (1974) and further developed in their succeeding paper (Mellor and Yamada, 1982), thus they are called Mellor-Yamada (MY) models. MY models were successively simplified by neglecting the highest orders of the turbulent anisotropy terms and are named according to the level of anisotropy they can describe. This simplification reduces the number of differential equations of the turbulence model. For example, widely used level 2.5 model retains only prognostic equation for the trace of the stress tensor (which represent turbulent kinetic energy); while the equations for the other stress tensor components, the velocity-temperature covariances and temperature covariance are simplified to the algebraic equations. MY level 2.5 model is a popular turbulent parameterization in mesoscale models, since it can reasonably well represent the turbulent effects in the PBL while adding only one prognostic equation to the mesoscale model. Even the more simplified level 2 model, where no prognostic equation for the turbulent fluxes remains (the turbulent mixing is the function of the stability alone), can be used to provide the lower boundary conditions for any higher order MY models.

Three main weaknesses of the original MY models were identified in the literature (e.g. Moeng and Wyngaard, 1989; Cheng et al., 2002): i) the low order of pressure-velocity and pressure-temperature covariance closure, ii) downgradient closure of the turbulent fluxes and iii) the uncertainty in the definition of the *Master Length Scale* (MLS) which controls the rate of the turbulent diffusion and dissipation, the pressure-strain and the pressure-temperature covariances. All three weaknesses were treated separately by different authors developing turbulence models. For example, Cheng et al. (2002) improved the closure of the pressure-strain and pressure-temperature covariances by including the additional higher order terms. Their improved MY scheme produced the turbulent fluxes closer to the measurement data as well as to the large eddy simulations. Among others, Canuto et al. (2001) derived the closures for the third order terms that were not restricted to be downgradient. They showed that with their closure, the modelled turbulent fluxes well resemble results from large eddy simulations. A lot of work on the improvement of the MLS was published since no useful physical equation for it exists. Rather, it is defined from the plausible assumptions. Umlauf and Burchard (2003) derived the generic equation for the MLS applicable to the large range of the turbulent flows. They also showed that many of the well known models can be derived by simplifying the generic length scale. However their generic length scale is more of theoretical value, since in its original form, it can not be implemented in the boundary layer parameterization model. Therry and Lacarrère (2002) distinguished between the dissipative and the diffusive length scales and further included the countergradient term into the turbulent exchange coefficient for heat. They argued that with these improvements, they were able to more realistically model the turbulent fluxes in the unstable atmosphere. Lenderink and Holtslag (2004) proposed the MLS in the neutral to convective conditions as a combination of two length scales, both as vertically integrated function of the Richardson number. The first length scale limits the total length scale at the surface and the second one at the top of the boundary layer. They showed that with their MLS formulation, the predictions of the wind and temperature profiles agree well with the measurements at Cabauw in the neutral and unstable atmosphere. Nakanishi (2001) changed the MLS definition of the level 2 MY model (used as a surface layer parameterization) and level 3 MY model (used as a boundary layer parameterization). He

5.2. BOUNDARY AND SURFACE LAYER PARAMETERIZATION

included the stability corrections close to the ground and non-local corrections in the stable atmosphere, improved the closure assumption of the pressure-temperature and pressure-strain covariance closures and retuned the parameters with the large eddy simulation results for the dry atmosphere.

In this paper, the MLS in the non-singular implementation of MY level 2.5 model in the boundary layer and MY level 2 in the surface layer by Janjić (2002) (therefore MYJ model) as formulated in the Weather Research and Forecasting Model (WRF) – Advanced Research Version (ARW) (Skamarock et al., 2005) was modified as described by Nakanishi (2001). The goal of this approach was to obtain improved wind profile structure in the lower part (up to a few 100 m's) of the Marine PBL (MPBL) for different stability conditions applying only simple adjustments to the WRF code. In the original version of the boundary layer MYJ model, the length scale following Blackadar (1962) was used as a MLS, which combines the Prandtl mixing length and the length scale depending on the bulk turbulent properties of the vertical column of the PBL. The surface layer parameterization in WRF is written in terms of the Monin-Obukhov similarity theory where the surface integrated stability functions must be specified. In the original WRF version, the integrated stability functions are based on Paulson (e.g. Chen et al., 1997) functions in the unstable surface layer and Holtslag and de Bruin (1988) functions in the stable surface layer. The integrated stability functions were recalculated to be consistent with the MY level 2 model. The sensitivity of the simulation results to the original or the modified parameterization was first investigated by idealized single column simulations. WRF with the original and adjusted parameterization was used for downscaling real (3 dimensional) data over the North and Baltic Sea. The improvement of the modified vs. the original parameterization was estimated by comparing the simulation results with the measurements in the lower part of the MPBL.

The organization of paper is as follows. In Sec. 5.2 and App. 5.A the original MYJ PBL parameterization is introduced. The modification of the MLS is described and the new surface integrated stability functions are derived. The measurement data used for the validation of the new scheme is introduced in Sec. 5.3. The results of the single column model are presented in Sec. 5.4. The ability of the new scheme to reproduce the observed structure of the PBL was tested against the measurements in Sec. 5.5 and compared to the original scheme for selected cases as well as evaluated for a longer time period. Finally, the discussions and conclusions are presented in the Sec. 5.6.

5.2 Boundary and surface layer parameterization

The surface and boundary layer parameterization model based on the second order closure by Mellor (1973); Mellor and Yamada (1974, 1982) as implemented in the WRF model by Janjić (2002) and the modification introduced in this study are briefly described in this section. The parameterization equations are presented in App. 5.A. The definition of the so called Master Length Scale (MLS) is altered to include the effect of surface stability close to the ground and in addition the nonlocal surface heat forcing in the statically stable atmosphere is included.

5.2.1 Original Mellor-Yamada-Janjić (MYJ) boundary layer parameterization

As is with the other second order schemes, in the MYJ model, closure assumptions for the third order moments ($\overline{u'_i u'_j u'_k}$, $\overline{u'_i u'_j \theta'}$ and $\overline{u'_i \theta'^2}$), dissipation rates ($\nu \frac{\partial u'_i}{\partial x_k} \frac{\partial u'_j}{\partial x_k}$ and $\alpha \frac{\partial \theta'}{\partial x_k} \frac{\partial \theta'}{\partial x_k}$), pressure-strain ($\frac{p'}{\rho} \left(\frac{\partial u'_i}{\partial x_j} + \frac{\partial u'_j}{\partial x_i} \right)$) and pressure-temperature ($\frac{p'}{\rho} \frac{\partial \theta'}{\partial x_i}$) covariances must be made¹. In MYJ scheme, the third order moments are parameterized as a downgradient flux, i.e. they are equal to the minus the product of the gradients of the second order terms and the diffusion length scale. The dissipation terms are proportional to the inverse of the dissipation length scale. The pressure-strain covariances are closed following the assumption of Rotta (e.g. Cheng et al., 2002), but retaining only the two highest order terms, the so called turbulence self interaction (return to isotropy, slow part) and mean shear-turbulence interaction (rapid part) terms. The turbulence self interaction term is assumed to be proportional to the inverse of the typical length scale over which the turbulence interacts. The pressure-temperature covariances are closed similarly, as the self interaction term of the pressure-strain closure. The important assumption of the MYJ scheme is that all the above mentioned length scales are proportional to each other everywhere in the boundary layer, therefore the MLS l is postulated which controls all of the above mentioned processes.

The MYJ scheme further simplifies the model equation by successively neglecting the highest orders of turbulent anisotropy. For the surface layer (from the ground to the first model level), so called level 2 model can be used, which assumes local balance between turbulence production, diffusion and dissipation. In level 2 model, the differential equations are simplified to yield the algebraic equation, where the turbulent mixing can be written as a function of Richardson flux number (R_f). The level 2 MYJ parameterization is equivalent to the Monin-Obukhov (MO) similarity theory, if the surface integrated stability functions are defined accordingly (Łobocki, 1993). The surface integrated stability functions derived in this paper are obtained from the MYJ level 2 model and used in WRF, whereas in the original version of WRF they were based on the Paulson (e.g. Chen et al., 1997) functions in unstable surface layer and Holtslag and de Bruin (1988) functions in the stable surface layer. In the proper boundary layer (from the first model level to the top of the PBL), the MYJ level 2.5 model is used where only prognostic equation for the Turbulent Kinetic Energy (TKE) is retained. For completeness, the equations of the level 2 and 2.5 MYJ model are given in App. 5.A, where the coupling of the surface layer with the surface is also briefly described.

In the original MYJ parameterization, the MLS close to the surface is assumed to be equal to the Prandtl mixing length (Stull, 1988):

$$l_S = kz \tag{5.1}$$

where k is von Karman constant (0.4) and z height above the ground. Far from the surface, the MLS l is the function of the bulk vertical structure of the PBL layer:

$$l_T = \alpha \frac{\int_0^\infty z q dz}{\int_0^\infty q dz} \tag{5.2}$$

The constant $\alpha = 0.3$ and the q^2 is the Turbulent Kinetic Energy (TKE), i.e $q^2 = \frac{1}{2} \overline{u_i'^2}$. The

¹The dash represent the fluctuations from the Reynolds averaged values, α and ν are kinetic heat conductivity and kinetic viscosity. Other symbols have their usual representation.

5.2. BOUNDARY AND SURFACE LAYER PARAMETERIZATION

integration in the Eq. 5.2, goes in principle till infinity, but in practice the TKE is zero above the top of the PBL. Inside the PBL, the MLS is a combination of l_S and l_T , so that the shortest length imposes the strongest constrain on the MLS:

$$\frac{1}{l} = \frac{1}{l_S} + \frac{1}{l_T} \quad (5.3)$$

5.2.2 Modifications of the original MYJ scheme

Surface layer

Usually the Prandtl mixing length l_S (Eq. 5.1) is used as a relevant macro-length scale for the turbulence in the near-neutral atmosphere close to the surface (e.g. Stull, 1988). Therefore the Blackadar MLS approaches Prandtl mixing length close to the surface. Prandtl mixing length is stability independent, while in the atmosphere far from neutral, it is expected that the stability plays a strong role in the rate of turbulent mixing and diffusion. In the statically stable atmosphere, the vertical movements require additional energy in order to overcome the environmental stability, which suppresses the vertical movements and thus effectively decrease the MLS. In the unstable atmosphere, the buoyancy assists vertical movements and therefore enhances turbulent vertical mixing and diffusion, causing an effective increase of the mixing length. Clearly, the characteristics of surface layer itself are stability dependent since the turbulent fluxes are a function of the stability (App. 5.A). With stability correction of the surface MLS, the rate of the dissipation and diffusion is adjusted accordingly. Loboeki (1992) also showed that the MY level 2 model with Prandtl mixing length does not have the right limits of the normalized fluxes and suggested to make the surface MLS stability dependent. To resolve the above mentioned problems, Nakanishi (2001) suggested that the new surface MLS be the function of the nondimensional surface stability $\zeta = z/L$, where L is Obukhov length and z height above the ground:

$$l = kz(a + b\zeta)^c \quad (5.4)$$

where a , b and c are empirical constants and Obukhov length (L) is defined as:

$$L = -\frac{u_*^3 \theta}{kgw'\theta'} \quad (5.5)$$

with the friction velocity $u_* \equiv (\overline{u'w'^2} + \overline{v'w'^2})^{1/4}$. Nakanishi (2001) performed a set of the idealized large eddy simulations (LES) and using the assumptions of the MY level 2 models, fitted the surface MLS to the LES results. For the stable layer ($\zeta > 0$), he found the best fit of l to the LES data with parameters $a = 1$, $b = 2.7$ and $c = -1$ from Eq. 5.4. In the unstable layer ($\zeta < 0$), he used the original Prandtl mixing length (i.e. $c = 0$ in Eq. 5.4) and changed the l as a function of stability for the unstable boundary layer with parameters $a = 1$, $b = -100$ and $c = 0.2$. Our experiments showed that decreasing the surface MLS in the unstable surface layer improves the agreement between the simulations and measurements. The surface MLS used in this paper is defined:

$$l = \begin{cases} kz(1 + 2.7\zeta)^{-1} & \zeta > 0 \\ kz & \zeta = 0 \\ kz(1 - 100\zeta)^{0.2} & \zeta < 0 \end{cases} \quad (5.6)$$

According to Łobocki (1992) analysis, the MLS should become independent of height in a very stable surface layer ($\zeta \rightarrow \infty$) since the turbulence becomes uncoupled from the ground and thus the height becomes irrelevant parameter. The new definition of the MLS agrees with this limiting values ($l \rightarrow kL/2.7$ when $\zeta \rightarrow \infty$). In the very unstable surface layer ($\zeta \rightarrow -\infty$), the MLS should be proportional to z . The newly defined MLS does not exactly fulfil this requirements since $l \propto z^{1.2}$ when $\zeta \rightarrow -\infty$. The mismatch between the expected limiting value and the one from Eq. 5.6 in the unstable surface layer however does not play an important role for the range of the stabilities modelled by the atmospheric mesoscale models.

The WRF surface layer parameterization is written in terms of the Monin-Obukhov (MO) similarity theory. Therefore the integrated stability functions for momentum and heat ($\Psi_M(\zeta)$ and $\Psi_H(\zeta)$, respectively) are required in order to represent the surface values of temperature, momentum and moisture to the first model level. In the approach taken here, the integrated stability functions are derived from the MY level 2 model with the surface length scale as defined in Eq. 5.6. The turbulent mixing in the MY level 2 scheme is expressed as a function of the flux Richardson number (R_f), while the integrated stability functions are dependent on the stability $\zeta = z/L$. The implicit relation between R_f and ζ based on the level 2 MY equation is derived by Łobocki (1993) in his Eq. A31.

$$\frac{l}{kz} = \frac{R_f(1 - R_f)^{-1/4}}{S_M^{3/4} B_1^{1/4} \zeta} \quad (5.7)$$

where S_M is the nondimensional diffusion coefficient for momentum and B_1 is the constant of the level 2 MYJ model (for details look in the App. 5.A). From the definitions of integral stability functions (Ψ_M and Ψ_H), flux Richardson number (R_f) and the gradient Richardson number (R_i) the integrated stability functions are calculated as (Łobocki, 1993):

$$\Psi_M(\zeta) = \int_0^\zeta \left(\frac{1}{R_f} - \frac{1}{\zeta'} \right) d\zeta' \quad (5.8)$$

$$\Psi_H(\zeta) = \int_0^\zeta \left(\frac{R_i}{R_f^2} - \frac{1}{\zeta'} \right) d\zeta' \quad (5.9)$$

The ratio of the gradient and flux Richardson numbers (R_i/R_f) in the Eq. 5.9 can be expressed by the ratio of the nondimensional diffusion coefficients for momentum and heat ($S_M(R_f)$ and $S_H(R_f)$, respectively) defined in App. 5.A or numerically as a function of ζ using Eq. 5.7:

$$\frac{R_i}{R_f} = \frac{S_M(R_f)}{S_H(R_f)} = f(\zeta) \quad (5.10)$$

The integrated stability functions are obtained by numerically integrating Eqs. 5.8 and 5.9. In Fig. 5.1, the following integrated stability functions are shown: i) from original WRF model, ii) derived by Łobocki (1993) (from MY level 2 model where Prandtl mixing length is used as a MLS) and iii) derived in this paper (new) with the similar procedure as in Łobocki (1993), where the MLS is described by Eq. 5.6. Both the integrated stability functions for heat and momentum from the original WRF implementation and Łobocki (1993) approach do not differ considerably among each other, while the new stability functions are significantly different. In the unstable surface layer ($\zeta < 0$), the new stability functions for momentum

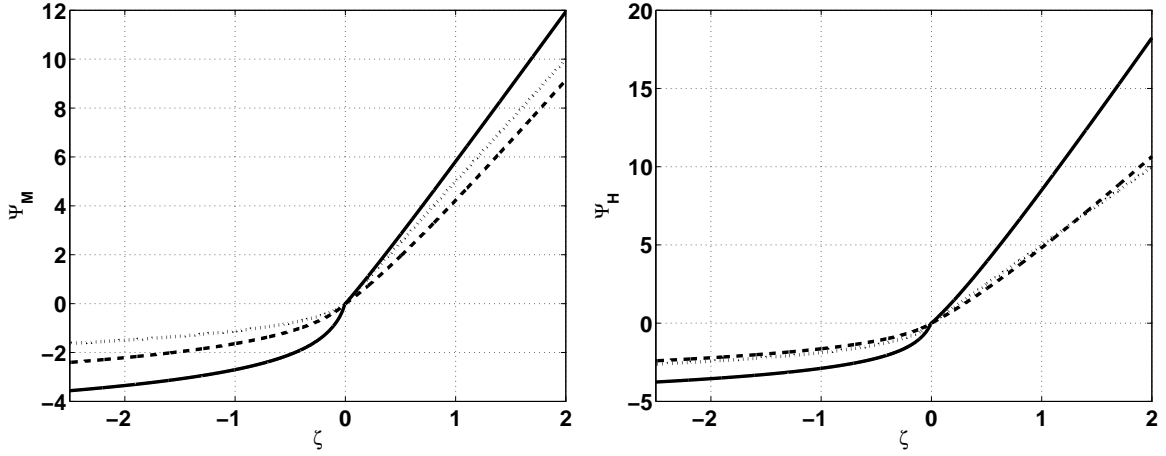


Figure 5.1: Integrated stability functions for momentum (Ψ_M , left) and heat (Ψ_H , right). Dotted line represent original WRF, dashed Loboeki (1993) (MY level 2 with Prandtl mixing length) and solid lines new stability functions.

(heat) are lower than the other two which implies that the parameterization with new stability functions will yield weaker momentum (potential temperature and moisture) gradients. In the stable surface layer ($\zeta > 0$), the opposite is true; the new stability functions for momentum (heat) are considerably higher than the other two which implies that the parameterization with the new stability functions will yield higher momentum (potential temperature and moisture) gradients.

The numerical fitting of the new stability functions to ζ from Fig. 5.1 gives the following relationships:

$$\Psi_M(\zeta) = \begin{cases} \frac{\zeta}{R_{fc}} + 1.12 \cdot \exp(1 - 1.67/\zeta) & \zeta > 0 \\ -0.99 \cdot \ln(1 - 14.2\zeta) & \zeta \leq 0 \end{cases} \quad (5.11)$$

$$\Psi_H(\zeta) = \begin{cases} \frac{\zeta R_{ic}}{R_{fc}^2 \Phi_T(0)} + 8.21\zeta^{1.11} & \zeta > 0 \\ -1.0 \ln(1 - 16.3\zeta) & \zeta \leq 0 \end{cases} \quad (5.12)$$

The values for the critical Richardson number $R_{ic} = 0.183$ and critical flux Richardson number $R_{fc} = 0.19$ and the ratio between gradient and flux Richardson number in the neutral atmosphere $\Phi_T(0) = 0.8$ were used above.

Boundary layer

The MLS in the boundary layer was taken from Nakanishi (2001). Similarly to Blackadar (1962), he defined the inverse of the MLS as the sum of the inverses of three different length scales: the surface layer length scale (l_S), the length scale depending on the turbulence property of the PBL (l_T) and the buoyancy suppression length scale (l_B). Formally, the MLS is written as:

$$\frac{1}{l} = \frac{1}{l_S} + \frac{1}{l_B} + \frac{1}{l_T} \quad (5.13)$$

Where the l_S , l_T and l_B are defined as:

$$l_S = \begin{cases} kz(1 + 2.7\zeta)^{-1} & \zeta > 0 \\ kz & \zeta = 0 \\ kz(1 - 100\zeta)^{0.2} & \zeta < 0 \end{cases} \quad (5.14)$$

$$l_T = \alpha_1 \frac{\int_0^\infty qz dz}{\int_0^\infty q dz} \quad (5.15)$$

$$l_B = \begin{cases} \alpha_2 q / N & \partial\Theta/\partial z > 0 \text{ and } \zeta \geq 0 \\ (\alpha_2 q + \alpha_3 q \sqrt{(q_c/l_T N)}) / N & \partial\Theta/\partial z > 0 \text{ and } \zeta < 0 \\ \infty & \partial\Theta/\partial z \leq 0 \end{cases} \quad (5.16)$$

The l_S is equal to the surface MLS which constrains the total master length scale at the surface. The function of l_T was not changed from the original definition of the MLS although the constant is now $\alpha_1 = 0.23$. The role of the buoyancy length scale (l_B) is to constrain the MLS in the statically stable atmosphere, especially in the upper part of the boundary layer. Here N is Brunt-Väisälä frequency and q_c the vertical velocity scale defined $q_c = (g/\theta_0 \overline{w'\theta_g} l_T)^{1/3}$, where the subscript g indicates values at the ground. The parameters in the Eq. 5.16 were set to $\alpha_2 = 1$ and $\alpha_3 = 5$ based on the LES simulation results.

5.3 Measurement Data

In order to compare the new with the original WRF surface/boundary layer parameterization for reproducing observed wind conditions in the lower part of the boundary layer, the results of the WRF simulations with both parameterizations are compared to the measurements of the wind profiles. Data from two measurement towers were used for validation. The Östergarnsholm tower operated by the University of Uppsala (Sweden) located in the Baltic Sea outside Gotland measures high resolution wind and temperature data up to around 30 m height above sea level. The data from the Östergarnsholm tower were widely used in the studies of the sea-atmosphere interactions (e.g. Smedman et al., 1999; Rutgersson et al., 2001b). As discussed below, the lower measurement levels are strongly influenced by the interaction of atmosphere-sea dynamics and are not useful for the purpose of this study. The tower structure does not influence the wind field as long as the wind does not come from the tower direction. In this study, seven months of the measurements were used (June 2005 - December 2005). FINO tower in the North Sea, build as a research platform mainly for the wind energy applications, is operated by German Wind Energy Institute (DEWI). The measurements are performed between 30 m and 100 m above msl. Due to the massive structure of the tower, different corrections were applied to the data. For this study, one year of measurements (January 2005 - December 2005) were used.

5.3.1 Measurements at Östergarnsholm

The field station Östergarnsholm is situated 4 km east of Gotland in the Baltic Sea (lat. 57°26'N, lon. 18°54'E). The wind measurements at Östergarnsholm tower are available at the heights of 6.9 m, 11.8 m, 14.3 m, 20.2 m and 28.8 m above the tower base which is 1 m above the mean sea level. The magnitude of the tide is around 0.5 m. The measuring levels in this paper are referred to as the levels from 1 (lowest level) to 5 (highest level). The variation of

measuring height due to the tide is neglected. The heat and momentum fluxes are derived from the high resolution (20 Hz) sonic wind speed and virtual temperature measurements 9 m above msl. The turbulent fluxes were provided by the University of Uppsala and were calculated from the deviations of wind speed/temperature from the 10 min running mean average and then averaged over an hour. More details on the flux calculation, and the applied corrections can be found in Smedman et al. (1999). Only the measurements representing the open sea conditions are used (wind direction between 80° and 220°) where the wind speed is not influenced by the tower structure or limited water depth.

The lower boundary layer structure over the sea can be significantly different from the boundary layer over land, mainly due to the influence of the waves (Sjöblom and Smedman, 2003). The wave influence on the atmosphere depends on the wave state; the growing waves behave almost like the land surface while mature or swell waves alter the momentum flux due to their dynamics. In the presence of long waves (or swell) the surface momentum flux is reduced or even changes sign. A smaller friction velocity changes the Obukhov length and the surface will appear to be more unstable (Rutgersson et al., 2001a). Close to the interface between atmosphere and the sea, the so called wave boundary layer (WBL) develops, where the wind speed does not follow the Monin-Obukhov scaling (Sjöblom and Smedman, 2003). In case of the developed or swell waves, the WBL can influence the lower part of the measuring levels. As was shown by Sjöblom and Smedman (2003), the wind profiles in the upper measuring levels (from 3 to 5) do not significantly suffer from the wave effects.

To properly describe the wave-atmosphere interaction in the mesoscale model, additional information about the state of the waves would be needed, i.e. the wave model would have to be run and coupled to the atmospheric model. Current version of WRF cannot describe the wave state, but couples the atmosphere to the ocean with the simple Charnock relationship, which assumes the local and instantaneous relationship between the wave state and the atmosphere. In order to avoid the complexities of the WBL influence on the atmosphere, only the wind speed measured at levels from 3 to 5 were used.

5.3.2 Measurements at FINO

FINO research platform (Neumann et al., 2004) located in the North Sea (lat. 54°0.86' N, lon. 6°35.26' E) performs multilevel measurements of three dimensional wind speed and temperature with high resolution (10 Hz) sonic instruments as well as with the lower resolution (1 Hz) cup anemometers. The sonic and cup instruments are positioned in the opposite tower arms, enabling correction of the tower wake effects on wind measurements. In this paper, the wind speeds at 40 m, 60 m and 80 m above mean sea level were used to derive the wind shear. The turbulent momentum and heat fluxes were calculated from the 40 m height and taken to represent the surface conditions. The measurements from the sonic anemometers were used as a primary source of the data while cup anemometer measurements were used to determine the corrections of the sonic measurements. The correction algorithms are crucial to obtain the reliable measurements of the wind speed and turbulent fluxes.

The data was pre-processed the following manner. First, the high resolution measurements were quality controlled by discarding data exceeding set limits (wind speed higher than 35 m s⁻¹, temperature higher than 30°C or lower than -15°C), based on the instrument limitations and the prevalent weather conditions over North Sea. Further, unreasonable peaks in the sonic data were removed with the method described by Vickers and Mahrt (1997). Additional corrections were applied to the data: i) calibration of cup anemometer, ii) anemometer

tilt angle correction and iii) tower-wake influence correction. The tilt correction was based on the planar fit (PF) method (Wilczak et al., 2001) which removes the contamination of the vertical wind speed by the horizontal wind speed. As shown by Wilczak et al. (2001), the tilt correction is important even for small tilt angles, since the vertical wind speed is around an order of magnitude smaller than the horizontal wind speed. At FINO, the tilt angles of the mounted instruments were between $0.5^\circ - 2^\circ$. The tower wake influence on the anemometer is significant for the winds coming from the direction of tower (anemometer is in the shade of wake), even though the tower has a mesh structure. For the wind directions between 90° and 170° the sonic anemometers are in the tower shade, therefore these data were discarded from further analysis. The wake however influences the wind measurements even beyond the shaded sector. In this case, the wake influence was assumed to be proportional to the sinus of the wind direction. The ratio between the sonic and cup anemometer 10 minute averaged wind speed was fitted to the ratio of sinus with different phase angles and the fit was used to correct the sonic measurements. The wake correction is up to 4% of the measured wind speed.

The hourly wind speeds used for comparison with the simulation results were obtained by averaging the wind speeds within each hour. The turbulent fluxes ($\overline{T'w'}$, $\overline{u'w'}$ and $\overline{v'w'}$) were calculated from a relevant covariances of the wind speed components and temperature anomalies over shorter time τ . The calculated fluxes obtained within each hour were then averaged to obtain the hourly fluxes. The time period τ has to be short enough that the mesoscale variability does not influence the turbulent fluxes and long enough that most of the turbulent variability is captured. Here, τ was chosen based on the multiresolution decomposition method (Vickers and Mahrt, 2003), in which τ depends on the bulk Richardson number calculated between 60 m and 40 m height. In most cases, the atmosphere is slightly unstable and τ reaches its maximum allowed value of 20 min.

If the measurements at the lowest FINO level (40 m) are taken to represent the surface conditions, the surface MLS can be derived from the high resolution wind data using the following assumptions. The turbulent eddies in the flow cause the turbulent diffusion and dissipation, where the largest eddies are the most efficient. Therefore, the MLS is approximately proportional to the dimension of the typical largest eddies in the flow. The integral time (T_0), which represents the time it takes for the typical large eddy to pass the anemometer can be calculated from the autocorrelation of the detrended horizontal wind speed (r_{uu}) (e.g. Davidson, 2006):

$$T_0 = \int_0^{\tau_0} r_{uu}(\tau) d\tau \quad (5.17)$$

The integration in Eq. 5.17 goes in principle to infinity ($\tau_0 \rightarrow \infty$), but due to the numerical stability in calculation of the integral time we choose τ_0 to be the value of time when the r_{uu} reaches its first zero. From the integral time scale (T_0), the integral length (L_0), which is the measure of the large eddy sizes, is obtained by assuming eddies are frozen in the atmosphere and move with the mean atmospheric flow (U_0).

$$L_0 = U_0 T_0 \quad (5.18)$$

The integral length (L_0) calculated from FINO at 40 m is assumed to be proportional to the surface MLS. In Fig. 5.2, the surface MLS normalized by kz calculated from each hour of FINO data and the one from the new parameterization are plotted against stability parameter

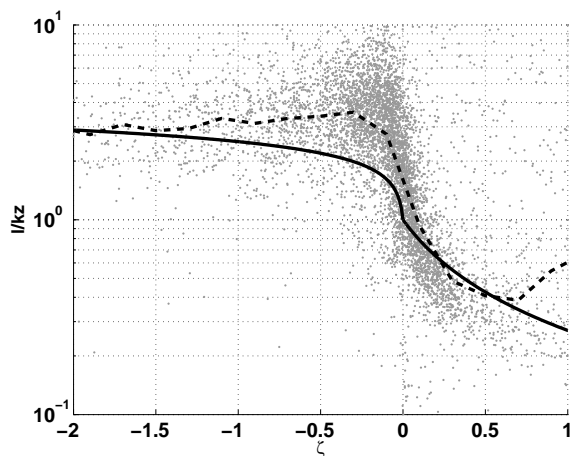


Figure 5.2: Scatterplot of the normalized integral length scale (l/kz) as a function of stability (ζ) from FINO at 40 m height. The new normalized surface Master Length Scale (MLS) is shown by black line and the median values of the MLS from the FINO measurements by the dashed line.

ζ . The spread of the measured data is relatively high especially for the neutral atmosphere ($\zeta \approx 0$) which can partially be related to assumptions used for calculating the surface MLS. However, there is a clear indication that the surface MLS is stability dependent and agrees better to the new parameterization than to the original one. The normalized original MLS is independent on stability and equal to one. The increase of the MLS with a very stable atmosphere ($\zeta > 0.5$) is probably related to the fact that in the stable boundary layer the surface layer is very shallow and that the 40 m measurement does not properly represent the surface layer.

5.4 Idealized single column studies

The simulations of WRF Single Column Model (SCM) with specified initial and boundary conditions were used to investigate the impact of the modified surface and boundary layer parameterization on the vertical structure of the planetary boundary layer. The SCM in WRF model can be created by setting the namelist variables accordingly, though minimal additional changes of the code are required. Richardson et al. (2005) provide an example on how to setup WRF model to run it as a SCM.

Initial conditions were chosen by specifying the following variables on pressure levels: i) potential temperature, ii) wind speed deviation from the geostrophic wind speed and iii) geopotential height. The Sea Surface Temperature (SST) and geostrophic wind speed, which are kept constant over time have to be additionally specified. The geostrophic wind speed is also constant with height. Moisture content of the atmosphere has been set to zero. The wind speed calculated by the SCM is interpreted as the ageostrophic component, since all the horizontal gradients (as well as pressure) are zero and thus the model cannot explicitly support the geostrophic wind speed. The sum of the geostrophic and ageostrophic wind speed is the input of the surface and boundary layer parameterizations.

	Experiment		L (m)	u_* (m s ⁻¹)	$\overline{w'\theta'}$ (10 ⁻³ K m s ⁻¹)	PBLH (m)
$N^2 = 0.2 \cdot 10^{-4} \text{s}^{-2}$ $\Delta T = -4\text{K}$	A	new	110	0.183	-4.7	60
		contr.	100	0.198	-5.1	100
$N^2 = 0$ $\Delta T = -2\text{K}$	B	new	220	0.196	-2.6	90
		contr.	240	0.209	-2.9	140
$N^2 = 0.5 \cdot 10^{-4} \text{s}^{-2}$ $\Delta T = 6\text{K}$	C	new	-250	0.342	12.6	550
		contr.	-200	0.321	12.6	540
$N^2 = 0.2 \cdot 10^{-4} \text{s}^{-2}$ $\Delta T = 4\text{K}$	D	new	-250	0.352	13.2	780
		contr.	-210	0.331	12.9	780

Table 5.1: SCM experiments defined in terms of the static stability of the free atmosphere (N^2) and initial temperature difference between atmosphere at surface and SST (ΔT). The results: surface Obukhov length (L), friction velocity (u_*) and boundary layer height (PBLH) for both the control (contr.) and the new parameterization. The results are averaged for 5 to 10 hours after the simulation start. The absolute errors estimated from the variability of the variables inside the averaging time are 10 m for L , 0.01 m s⁻¹ for u_* , $0.2 \cdot 10^{-3}$ K m s⁻¹ for heat flux and 20 m for PBLH for stable surface layer and 40 m for PBLH for unstable surface layer

The SCM was set over the sea point at lat. 54°00'N, lon. 6°35'E (Coriolis parameter $f=1.1812 \times 10^{-4} \text{s}^{-1}$) corresponding to the centre of the North Sea. 70 vertical levels were defined, which is twice the number of levels as in the real (three dimensional) simulations presented in the next section. The same conclusions are valid also for 35 vertical levels. The radiation (long- and short-wave) and moist physics (cloud, convection and evaporation) were turned off. The vertical profiles of all variables were specified up to 400 hPa (approximately 7000 m), depending on the experiment. Above 400 hPa, the profiles of the temperature and geopotential height from the US standard atmosphere were used. Due to the instabilities in the model related to wind initialization, model was first run with the prescribed starting logarithmic wind profile from the ground to 800 hPa (around 2000 m). After 48 h of model running, the resultant wind profile was used as the initial wind for the same run, from which the results are shown.

Zilitinkijevich et al. (2007) showed that the stability of the boundary layer can be characterized by two parameters: i) Brunt-Väisälä frequency (representing static stability) of the background atmosphere in which the PBL grows and ii) the surface heat flux. To perform simulations for wide range of the atmospheric conditions, the geostrophic wind speed has been set to 10 m s⁻¹ in the zonal direction (u component), while the proportion of the buoyancy and the shear contribution to the TKE production was controlled by altering the SST (i.e. surface heat flux). The background atmosphere was always statically stable or neutral ($N^2 \geq 0$). If this is not the case, the boundary layer almost immediately extends up to the tropopause.

Tab. 5.1 show some characteristic results for the parameters obtained in experiments for two stable and two unstable surface layers: Obukhov length (L), friction velocity (u_*) and heat flux ($\overline{w'\theta'}$) as well as the height of the boundary layer (PBLH). In the following, the WRF with the original parameterization will be referred as the *control* parameterization and the WRF with the parameterization described in this paper as a *new* parameterization.

5.4. IDEALIZED SINGLE COLUMN STUDIES

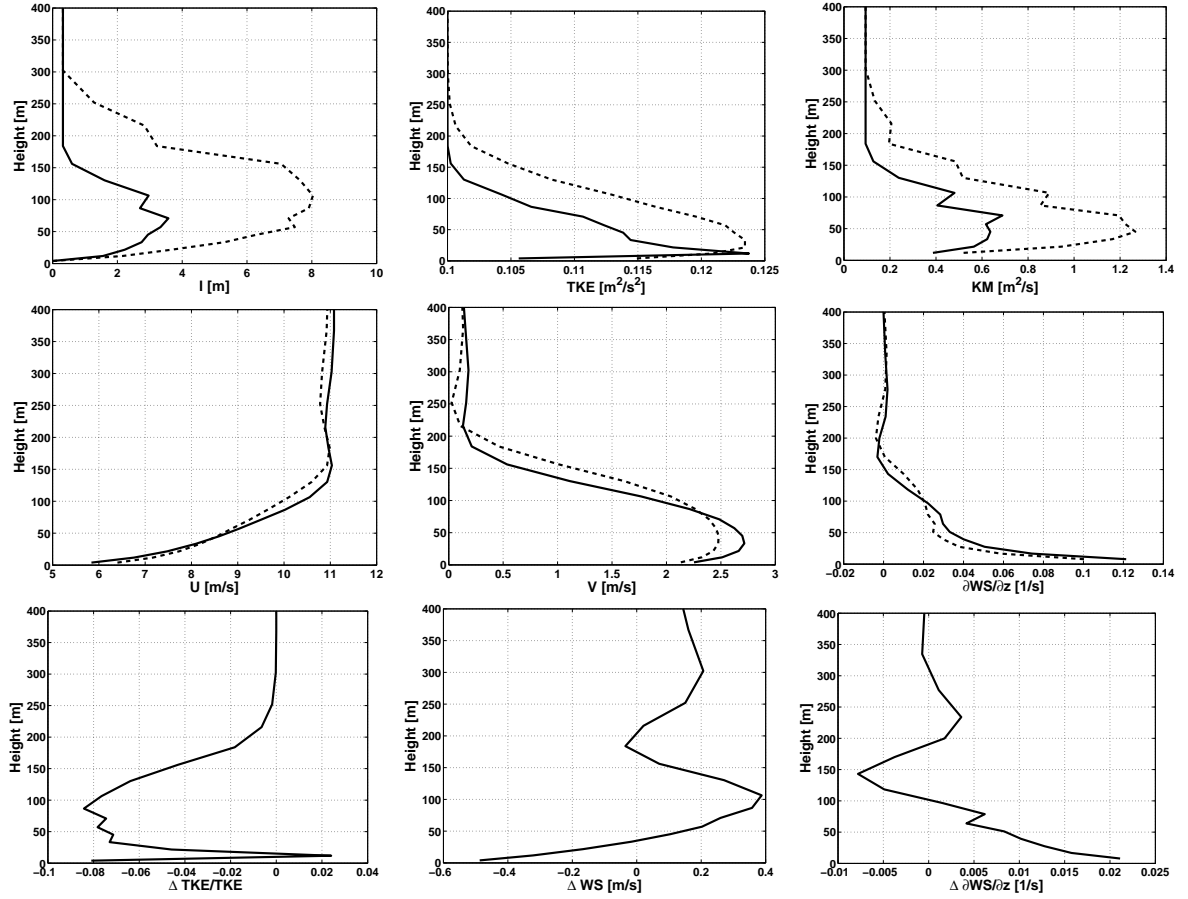


Figure 5.3: Experiment B ($N^2 = 0$, $\Delta T = -2$ K). Vertical profiles of MLS (l), Turbulent Kinetic Energy (TKE) and turbulent exchange coefficient for momentum (K_M) (upper panel), wind speed along the geostrophic wind (U), perpendicular to geostrophic wind (V) wind shear ($\partial WS/\partial z$) (middle panel), relative difference between new and control TKE , the difference between WS and wind shear between the new and control simulation. In the upper and middle panel solid lines represent the new parameterization, dashed control.

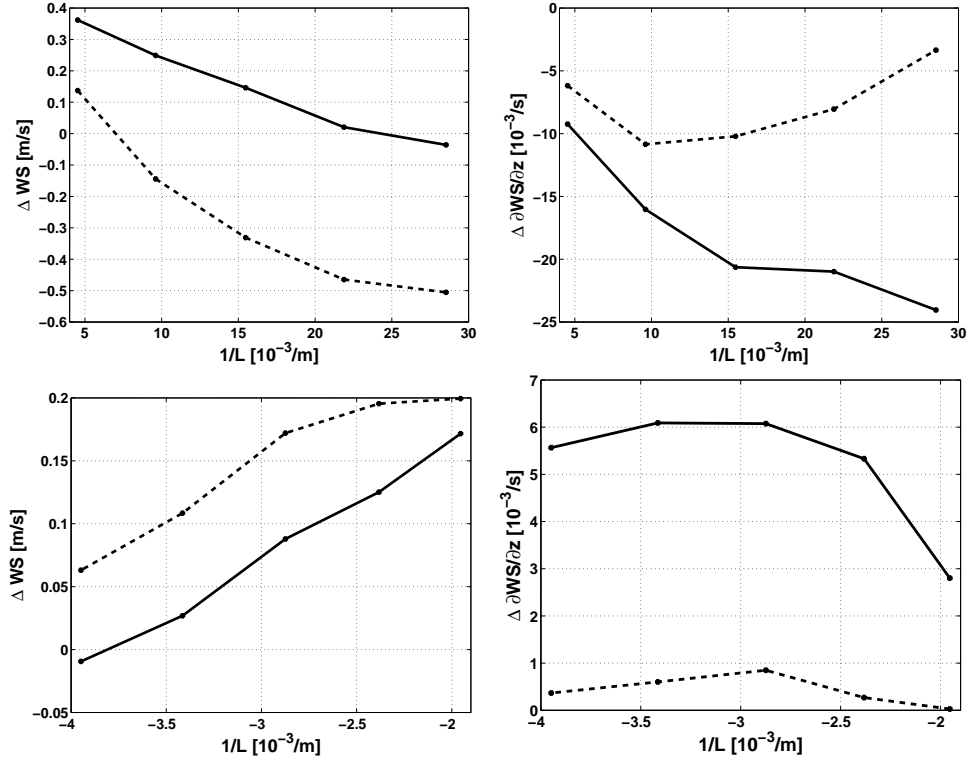


Figure 5.4: Left panels: The wind speed difference between the new and the control simulation at 20 m above the sea level (solid lines) and 50 m above sea level (dashed lines). Right panels: The difference between wind shear from the control and new parameterization between levels 30 m and 10 m (solid line) and between 60 m and 40 m (dashed line). Upper panel is for stable surface layer, lower for unstable surface layer.

In order to study the difference between wind characteristics from new and control simulation results at FINO and Östergarnsholm measurement levels for different surface stability conditions, additional simulations were performed. For the atmosphere with the stable surface layer, the free atmosphere was set to neutral ($N^2 = 0$) while the temperature difference between the SST and the air above the sea was changed in steps from -0.5 K to -8 K. For the simulations with the unstable surface layer the free atmosphere was stable ($N^2 = 0.2 \cdot 10^{-4} \text{s}^{-2}$), while the temperature difference between SST and the air above the sea was varied from 3 K to 8 K.

5.4.1 Negative surface heat flux - stable surface layer

The wind shear difference between the new and control parameterization is expected to be higher with increasing stability of the surface layer. In upper panel of the Fig. 5.4, the wind speed and the wind shear differences between the new and control simulations at roughly the Östergarnsholm and FINO measuring heights are shown. At the Östergarnsholm levels, the wind shear difference is higher and clearly increases with the higher stability of the atmosphere (higher $1/L$), while at the FINO level for the very stable cases, the wind shear difference start decreasing again. In the very stable surface layer, the boundary layer is very shallow and the

FINO measurement levels are at the heights where wind speed from the new simulation is already higher than from the control. The difference of the wind speed between the new and control simulation is below 0.5 m s^{-1} which is small compared to the geostrophic wind speed of 10 m s^{-1} .

5.4.2 Positive surface heat flux - unstable surface layer

The results from the experiments *A* and *B*, where the surface heat flux is negative are discussed. The experiments *A* and *B* differ by the amount of the surface heat flux and the stability of the free atmosphere acting with the buoyancy force against growing boundary layer. The heat flux from the atmosphere to the surface in the experiment *A* is around 50% higher than in experiment *B* (Tab. 5.1). The resultant profiles of relevant parameters from both experiments are qualitatively the same, therefore only the profiles from the experiments *B* are shown (Fig. 5.3). In both experiments *A* and *B*, quasi-equilibrium between the growth of the boundary layer by the shear production of the *TKE* and suppression due to the stability is reached. In the new parameterization the MLS is shorter than in the control one mainly due to the shorter surface length scale (l_S). MLS is the reflection of the effective distance over which the turbulence fluxes are diffused and mixed. Therefore, shorter length scale indicates more localized turbulence. As a direct consequence of the shorter MLS in the new parameterization, the diffusion coefficients for momentum and heat (not shown) in the new parameterization are smaller. The *TKE* and consequently the wind profiles are adjusted in the new parameterization as follows. In the lower part of the boundary layer, the smaller diffusion coefficient for momentum (heat) is compensated by the higher wind shear (potential temperature gradient) therefore the turbulent surface fluxes are only slightly smaller in the new parameterization compared to the control (Tab. 5.1). Since the wind shear in the new parameterization is higher in the lower part of the boundary layer, it is compensated by the lower wind shear in the upper part of the boundary layer. At around 10 m above the ground, the wind shear from the new parameterization is around 20% higher than in the control. In the new parameterization the wind speed is smaller close to the surface, while around 40 m above the ground it becomes higher and again smaller close to the top of the boundary layer. The difference between the wind speed from the new and control parameterization is small with the highest value of around 0.45 m s^{-1} in the first model level (around 5 m above the surface). In the new parameterization, the *TKE* is generally lower than in the control, but has a sharper peak in the second model level. The boundary layer height in the new parameterization is lower as the consequence of less efficient mixing in the boundary layer.

In case of the positive surface heat flux and stable background atmosphere, the boundary layer does not stop growing but it slowly penetrates through the inversion by mixing and transporting heat from the surface to the inversion. In general, the effect of the new parameterization in experiments *C* and *D* (positive surface heat flux) is qualitatively the opposite to the experiments *A* and *B* (negative surface heat flux). In the new parameterization, the MLS is longer in the lower part of the boundary layer and slightly shorter in the upper part of the boundary layer due to the buoyancy suppression length scale (l_B) which leads to higher turbulent exchange coefficients. Almost opposite as is for the stable surface layer, the higher exchange coefficients for momentum (heat) in the lower part of the boundary layer are compensated by the smaller wind shear (potential temperature gradient), while the turbulent fluxes at the surface are only slightly smaller in the new parameterization compared to the control one. The wind shear close to the ground is around half of the stable layer wind shear

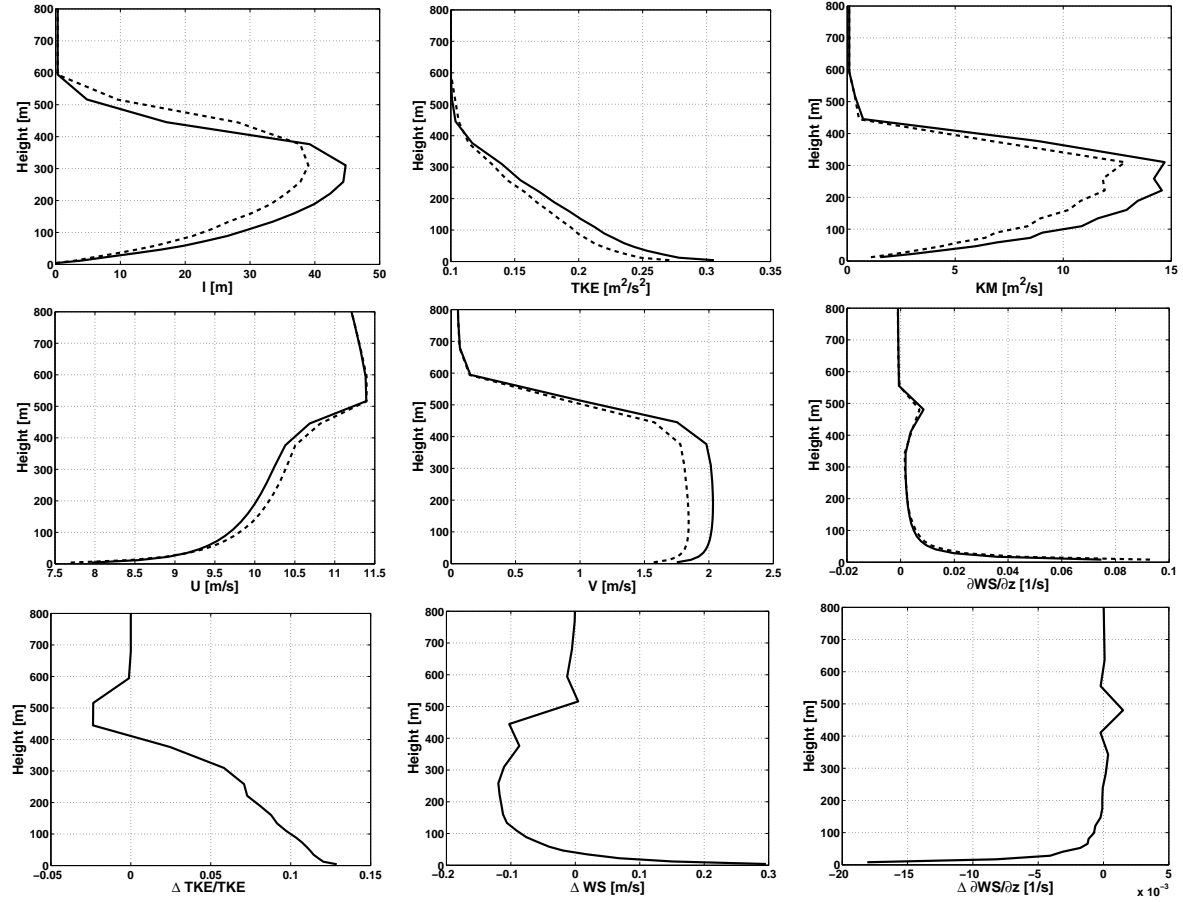


Figure 5.5: The same as 5.3, only for experiment C ($N^2 = 0.2 \times 10^{-4} \text{ s}^{-2}$, $\Delta T = 6 \text{ K}$).

(experiment B). The difference between the wind speed and wind shear from the new and control simulation is the highest close to the ground and rapidly decreases with the height.

In lower panel of Fig. 5.4, the wind speed difference and the wind shear difference between the new and the control simulations for the levels of the measuring platforms are shown. In all experiments difference between the wind speed from the new and control simulation is always lower than 0.2 m s^{-1} . The wind shear at Östergarnsholm levels is considerably smaller in the simulation results from the new parameterization than from the original.

5.5 Real Simulations

The WRF model was used to downscale the atmospheric conditions and refine the atmospheric boundary layer structure over the measuring platforms for the periods of the available measurement data. The non-hydrostatic WRF model with Ferrier microphysics, rapid radiative transfer longwave, Dudhia shortwave and Bets-Miller-Janjić convective (not used in the third domain; look below for the explanation of the domain) scheme was used. The Noah surface scheme over the land was selected, where the viscous sublayer over the sea was implemented. More details of the model and references can be found in Skamarock et al. (2005).

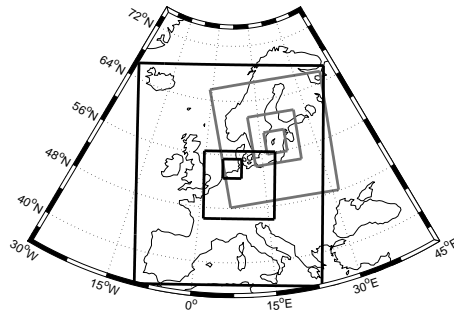


Figure 5.6: Domains for real WRF simulations. The black boxes indicate FINO simulation domains, gray the domains for the Östergarnsholm simulations.

Two sets of simulations were performed, with each i) the *Control* (original WRF MJY) and ii) the *New* surface and boundary layer parameterizations in order to investigate whether the representation of the boundary layer conditions can be improved. Separate simulations were done for each measurement tower, where three (two-way) nested domains were defined with their horizontal resolution of 27 km, 9 km and 3 km, respectively. Fig. 5.6 shows the location of the domains. In the vertical, 35 eta levels were set, usually 4 half-levels (where the horizontal wind speed is calculated) were below 100 m and the first half-level is at around 8 meters above the mean sea level. The WRF model was initialized every second day at 18UTC from the NCEP Final Analysis (FNL) data² with the horizontal resolution of $1^\circ \times 1^\circ$. First 6 hours of the simulation were discarded as the spinup of the model, and the subsequent 48 hours starting at 00UTC were used to form the downscaled hourly resolved dataset. The lateral boundary conditions of the first WRF domain were updated every 6 hours from the FNL analysis. The boundary layer structure is very sensitive to the sea surface temperature (SST), since the difference between SST and temperature of the overlying air defines the surface stability. In the Baltic Sea, the SST is highly variable in space which cannot be properly described by the relatively low resolution FNL data. Therefore for the simulations at Östergarnsholm, the 3-day averaged high resolution ($\sim 1 \text{ km} \times 1 \text{ km}$) analysis of satellite measured SST, provided by the German Federal Maritime and Hydrographic Agency (Bundesamt für Seeschifffahrt und Hydrographie, BSH) was used instead. For the simulations at FINO the SST from FNL was used, since it is well able to describe its spatial variability. SST field was kept constant through the simulation period.

The main aim of the boundary/surface layer modification was to improve the near surface wind conditions. The WRF fields: Wind Speed (WS), which is a three dimensional field computed at each level from the magnitude of zonal and meridional wind components and variables that describe the forcing at the bottom of the surface layer, namely the friction velocity (u_*) representing the momentum flux and the inverse of the Obukhov length ($1/L$) representing the surface stability are shown. The WRF results were first bi-linearly interpolated in the horizontal from the nearest four points to the measurement tower location. The wind speed was linearly interpolated in the vertical from the model half-levels to the measurement heights. The comparison between the measurements with the simulation data is shown first for the selected cases (Sec. 5.5.1) and then for the complete analysis period

²Available at: <http://dss.ucar.edu/datasets/ds083.2/>

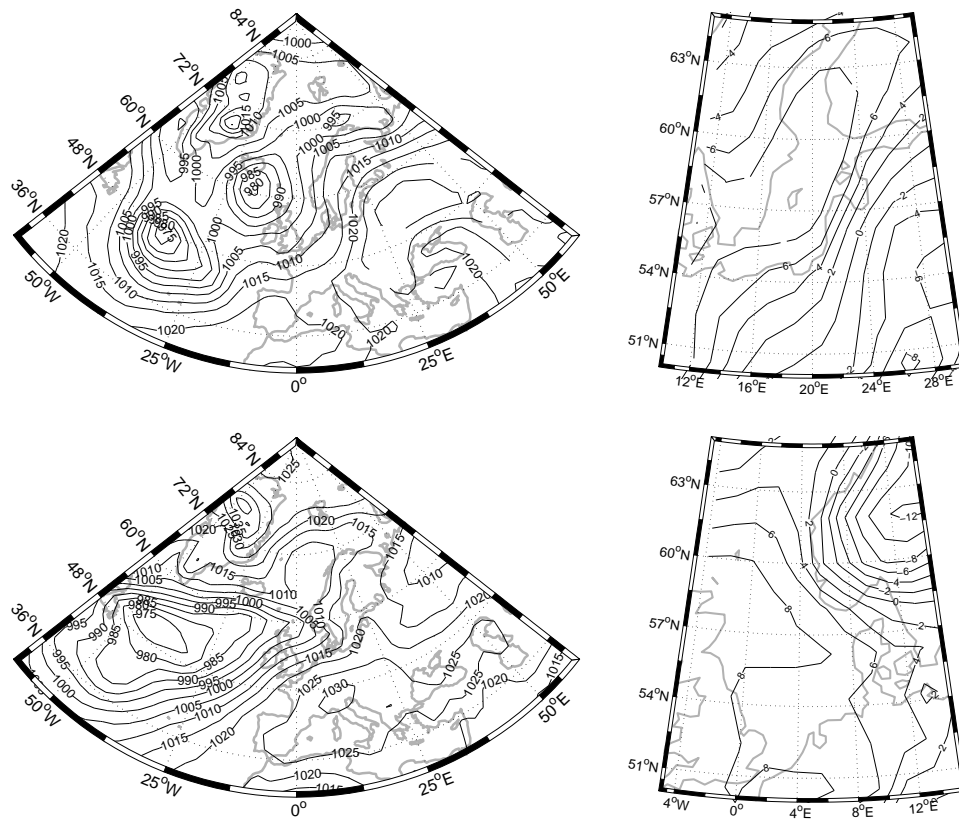


Figure 5.7: SLP (left) and T2M (right) representing synoptic situation for the stable cases at Östergarnsholm - November 1. 2005 at 00 UTC (top) and FINO March 16. 2005 at 00 UTC (bottom). The plots are from NCEP/NCAR reanalysis.

(Sec. 5.5.2).

5.5.1 Case studies

The simulations of lower boundary layer with control and new parameterization are compared to measurements for selected unstable and stable surface layer cases at Östergarnsholm and FINO. The criteria for the stability is inverse Obukhov length ($1/L$) at surface, where for stable cases $1/L > 0$ and for unstable $1/L < 0$.

Usually, the surface stability over the sea does not have a pronounced diurnal cycle as is the case over land, but it is mainly determined by the properties of the advected air masses due to large scale forcings. At FINO especially in the cold part of the year, the south-westerlies to westerlies advect warmer air over a cold sea which results in a stable surface layer. In the unstable surface layer, the wind direction is mainly from North-West to North-East advecting the cold air over the North Sea. The wind speed is generally higher in stable cases and is determined by the horizontal, approximately zonal pressure gradients. Similar, although less clear relationship between stability and large scale forcing can be observed at Östergarnsholm (not shown). In the Baltic Sea, the complexity of the surrounding land masks the direct relationship between stability and large scale forcings.

Stable case at Östergarnsholm

As a representation of the stable case at Östergarnsholm the period from the Nov. 1 2005 at 00 UTC to Nov. 2 2005 at 11 UTC was selected. The synoptic situation defining weather conditions over the Baltic Sea did not change significantly during these two days and was determined by the low pressure system over the Atlantic and North-Western Europe with minima over the Atlantic (at around lat. 45°N, lon. 30°W), North-East of Great Britain and North of Scandinavia and high pressure above the South-Eastern and Eastern Europe (upper left panel of Fig. 5.7)³. Near surface winds over the Baltic Sea were southerly and turned toward South-West direction with height (not shown). The southerly near-surface winds advect the warmer air over the Baltic Sea (upper right panel of Fig. 5.7). In the southern Baltic Sea, the difference between the SST and the near surface air temperature is around 2°C, which results in the stable surface layer and a surface inversion which persisted throughout the study period (not shown).

The atmosphere at Östergarnsholm is stable during most of the period with increasing stability toward the end (upper left panel on Fig. 5.8). The wind speed increases from around 10 m s⁻¹ at the beginning of the period to around 14 m s⁻¹ in the evening of Nov. 1 and decreases down to 8 m s⁻¹ towards the end of the period. The wind speed simulated by both parameterizations (control and new) is slightly underestimated (around 1 m s⁻¹) at the 5th measurement level. The simulated friction velocity (u_*) and stability ($1/L$) from both versions (new and control) well reproduce the measurements and do not differ considerably from each other. The relative good agreement between the measured friction velocity and the stability suggests that the lower boundary conditions in simulations are well captured. Surface friction velocity and the surface Obukhov length are crucial parameters defining the wind profiles since they are the main parameters of the surface layer parameterization. Both of the fields are partially related to the lower boundary conditions (through SST and roughness length) and partially result from the surface layer parameterization.

The results of the control simulation show that the model underestimate the wind speed difference between the 5th and 3rd as well as between the 5th and 4th measurement level. The results from the new simulations yield higher wind shears which agree better with the measurements (middle panel on Fig. 5.8). The structure of the vertical profile of the time averaged wind speed (lower right panel on Fig. 5.8) from measurements agrees much better to the new than to the control simulation results. The control scheme seems to underestimate wind shears at the upper measurement levels at Östergarnsholm which are significantly improved on applying the new parameterization.

Stable case at FINO

The case from March 16. 2005 at 00 UTC to March 18. 2005 at 12 UTC was chosen as a representative for stable surface condition at FINO. The synoptic situation during this period is similar to the one defining stable surface condition at Östergarnsholm. The low pressure system resides over the Atlantic and high pressure over the southern Europe (lower left panel of Fig. 5.7). During the simulation time, the high pressure system moves in the north-west direction (not shown). At the beginning of the period western near surface winds dominate over the North Sea which turn toward North-West at the end of the study period. The wind

³The synoptic situation is plotted from the NCEP/NCAR Reanalysis data available at: <http://www.cdc.noaa.gov/cdc/reanalysis>

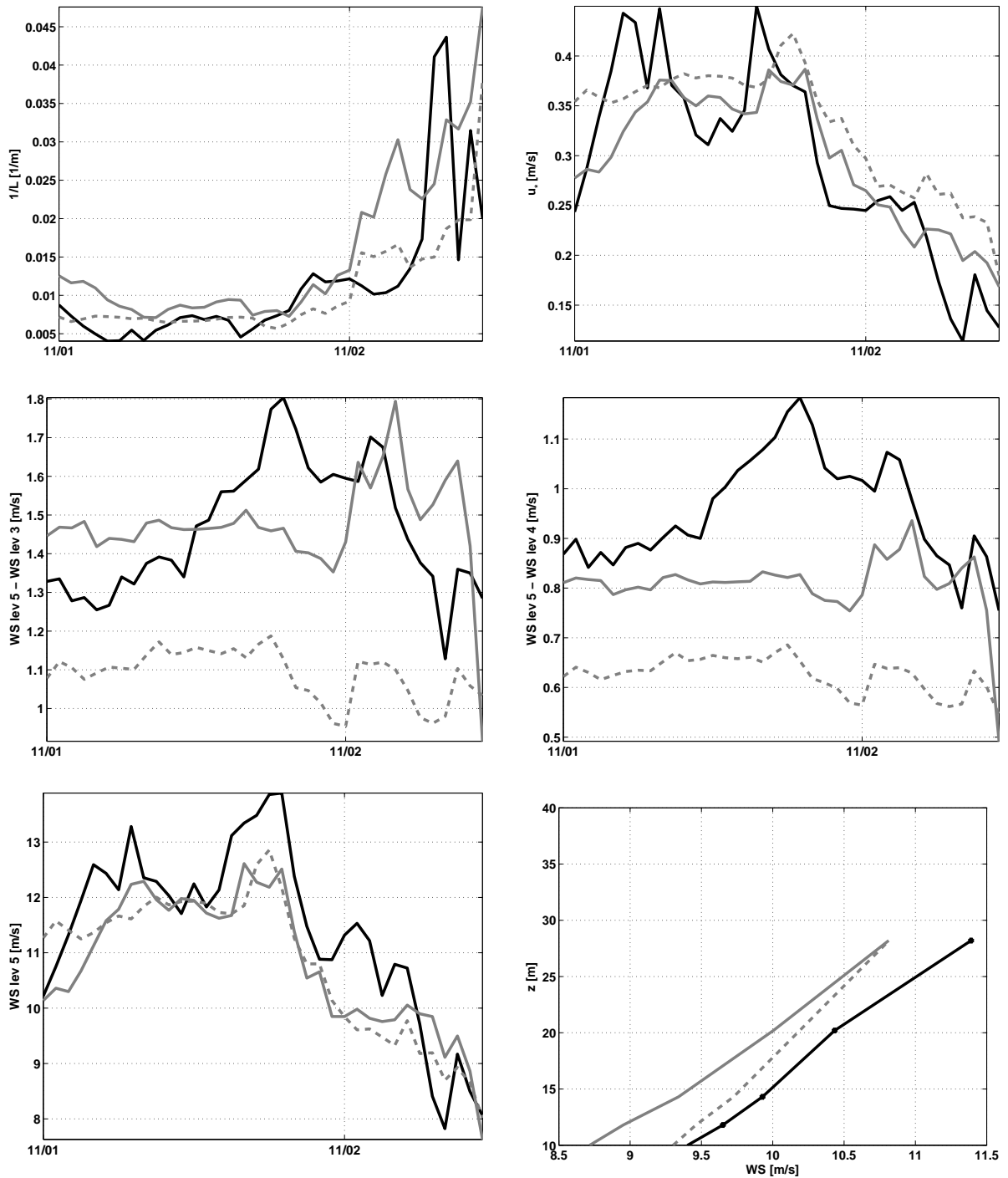


Figure 5.8: Stable case at Östergarnsholm (Nov 3. 2005 at 00 UTC to Nov 5. 2005 at 00 UTC): comparison of the measured $1/L$, u_* (upper panel), wind speed difference between level 5 and 3 and level 5 and 4 (middle panel), wind speed at level 5 and time averaged wind profile (lower panel). The black line: measurements; Dashed gray: control; Solid gray: new WRF.

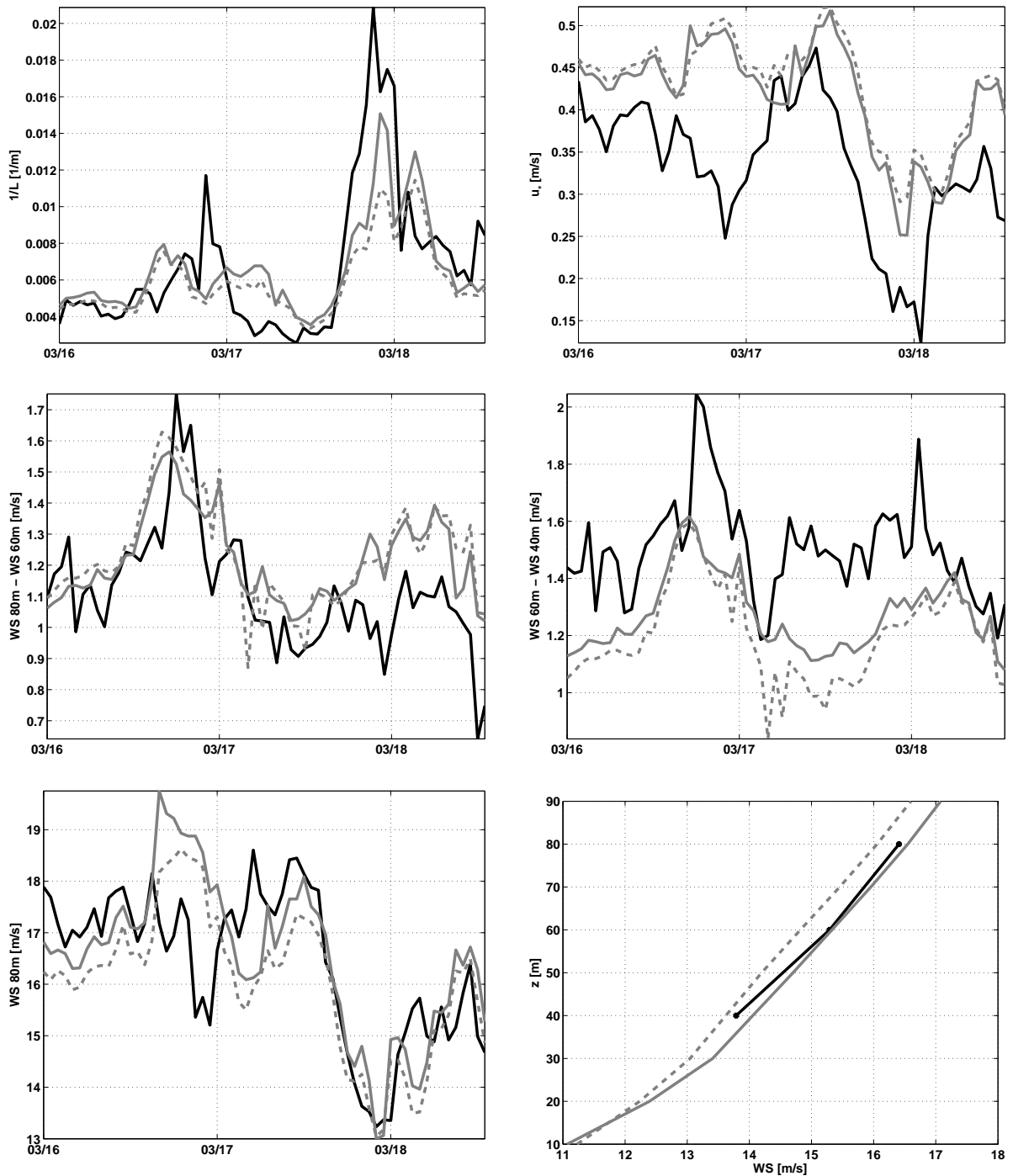


Figure 5.9: Stable case at FINO (March 16. 2005 at 00 UTC to March 18 2005 at 12 UTC): comparison of the measured $1/L$, u_* (upper panel), wind speed difference between height of 80 m and 60 m and 60 m and 40 m (middle panel), wind speed at 80 m height and time averaged wind profile (lower panel). The black line: measurements; Dashed gray: control; Solid gray: new WRF.

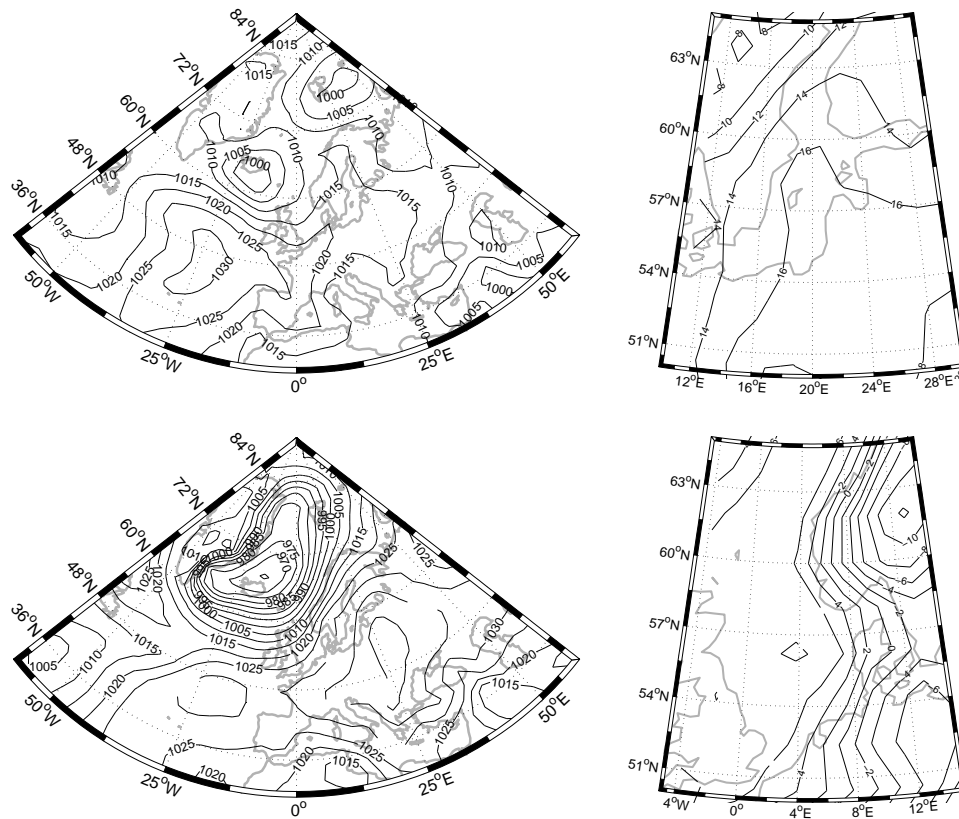


Figure 5.10: SLP (left) and T2M (right) representing synoptic situation for the unstable cases at Östergarnsholm - August 3rd 2005 at 00 UTC (top) and FINO - February 2nd at 00 UTC (bottom). The plots are obtained from NCEP/NCAR reanalysis.

advects the warm air from the West over a colder sea. The temperature difference between the near surface air and SST is around 3°C at the start of the simulations.

Fig. 5.9 compares the measurements and simulations for both the control and the new parameterization for the stable condition at FINO. The stability of the surface layer has a slight diurnal cycle. It is only slightly stable during the day and more stable during the night, especially on the night from 17. to 18. March. The diurnal cycle may be due to the advected continental air over measurement platform. The surface stability is relatively well simulated by both the new and control version. The friction velocity seems to be slightly overestimated by both versions, though inaccuracies in the measurements can not be excluded. The measured friction velocity is estimated from the 40 m level which is expected to be lower than the real surface value (e.g. Gryning et al., 2007). The wind speed is around 17 m s^{-1} at the beginning of the period and decreases to 13 m s^{-1} in the night from the 16. to 17. March. The wind speed is well simulated by the control as well as the new simulation results. The wind shear between the control and the new parameterization did not change significantly. The control parameterization is well able to reproduce the wind shear between the upper two measurement levels (80 m and 60 m), while at the lower two (60 m and 40 m) levels, it is slightly too low. With the new parameterization, the wind difference between the lower two measurement levels is slightly increased, thus it is closer to the measurements, while between

the upper two levels remains almost unchanged. It is apparent from the time averaged vertical profile of the wind speed, that the new parameterization mainly influences the wind shear in the lower part of the boundary layer (from ground to around 40 m). Therefore the change in the parameterization does not have a considerable influence on the wind shear at FINO measurement heights.

Unstable case at Östergarnsholm

It was harder to find a time persistent case for the unstable surface layer at both Östergarnsholm as well as FINO. The case from August 3. 2005 at 21 UTC to August 4. 2005 at 15 UTC was chosen as a representative for unstable conditions at Östergarnsholm. The synoptic situation was characterized by the approximately zonal sea level pressure gradient with the high pressure system over the South-Western and Western Europe and Atlantic with maxima North of Azores, and low pressure over Iceland (upper left panel on Fig. 5.10). Baltic Sea was under the high pressure system, westerly near-surface wind transported colder air from Atlantic over the Baltic Sea.

The comparison of measurements at Östergarnsholm with simulation results is shown on Fig. 5.11. The near surface layer at Östergarnsholm is close to neutral at the beginning and at the end of the case and more unstable from the mid-day to the evening. The winds are weak throughout the whole period and are between 4.5 m s^{-1} and 7 m s^{-1} measured at 5th Östergarnsholm level. The simulated atmosphere from both the new and control simulations is too unstable compared to the measurements ($1/L$ from both simulations is lower than measured) which is mainly due to the overestimation of surface heat flux by WRF simulations (not shown). In the second part of the period, the wind speed is slightly underestimated by both versions. The wind shear between the 5th and 3rd as well as 5th and 4th measuring level from the control results is highly overestimated which is improved by the results of the new simulation. The shape of the time averaged wind profile from the new parameterization results agrees significantly better to the measurements than the results from the control parameterization, although the wind speed is underestimated in both cases.

Unstable case at FINO

For the unstable case at FINO, the period from Feb. 8 2005 at 13 UTC to Feb. 9 2005 at 06 UTC was selected. The synoptic situation is shown on the lower panel of Fig. 5.10. The low pressure system resides over Northern Atlantic (sea level pressure minimum is located above Iceland) and the high pressure system extends from Azores to central Europe. In the beginning of the case, the near surface wind over the North Sea was weak easterly, and turning toward West with height (around 4000 m the winds were westerly). During the simulation period, the westerly wind reaches the surface and stabilizes the unstable surface layer by advecting warmer surface air. At the beginning of the period the surface layer at FINO was highly unstable and the wind speed was below 4 m s^{-1} (at 80 m height). At the evening of Feb. 8th the wind speed increased and the atmosphere stabilized. In the simulations of both the control and new parameterization surface instability is overestimated compared to the measurements, which is result of the higher heat flux from the surface as compared to the measurements (not shown). The wind shears between both 60 m and 40 m as well as between 80 m and 60 m from control simulation are too low compared to the measurements and are slightly improved in new version. The time averaged vertical profiles of the wind

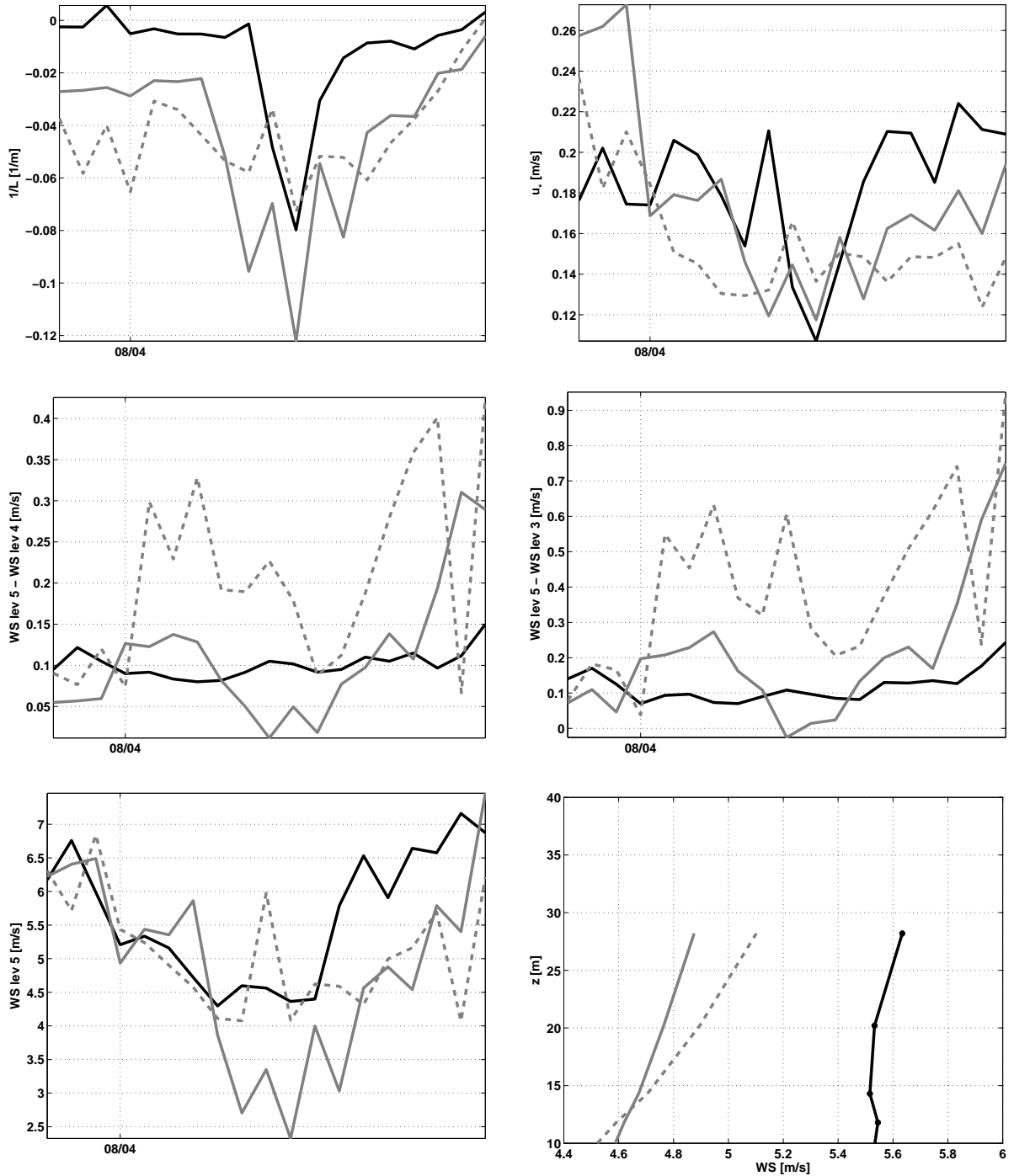


Figure 5.11: Same as 5.8, only for unstable case in Östergarnsholm (Aug. 3. 2005 at 21 UTC to Aug. 4. at 15 UTC).

5.5. REAL SIMULATIONS

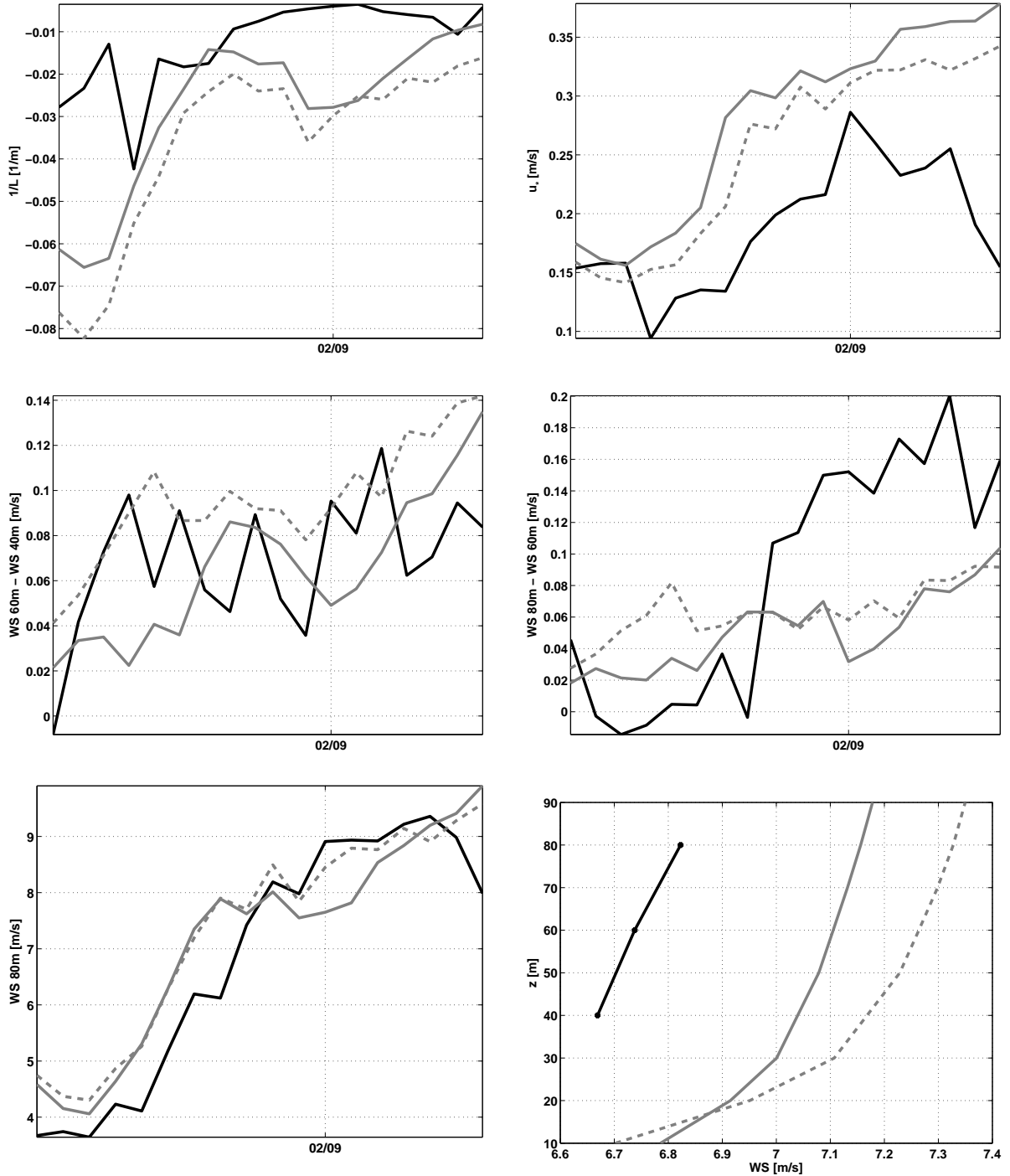


Figure 5.12: Same as 5.9, only for unstable case in FINO (Feb. 8. 2005 at 13 UTC to Feb. 9. at 06 UTC).

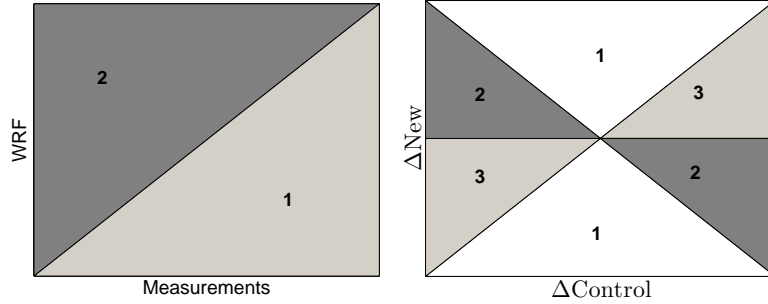


Figure 5.13: Schematic plot of the graphs used to compare the WRF simulations with measurements. Left hand side: two dimensional histograms of the WRF simulation against measurements. Right hand side: two dimensional histograms of the difference between control WRF and measurements (x -axis) and difference between new WRF and measurements (y -axis). For explanation look in the text.

Measurement	Level [m]	orig.	new
FINO	40	2.1	2.1
FINO	60	2.3	2.3
FINO	80	2.3	2.4
Östergarnsholm	14.3	1.7	1.6
Östergarnsholm	20.2	1.7	1.6
Östergarnsholm	28.8	1.7	1.7

Table 5.2: Root mean square error ($rmse$) [$m s^{-1}$] between wind speed measurements (FINO and Östergarnsholm) and WRF simulation data (control and new parameterization).

speed indicate that the important difference between the new and control parameterization is in the lower 30 m, whereas in the upper levels the wind profiles do not differ considerably.

5.5.2 Statistics

The analysis of the case studies shown in the previous subsection indicates the expected improvement of the new vs. the control parameterization. The wind speed itself is only slightly dependent on the parameterization used. The wind shear between the new and the control parameterization differs the most close to the surface (at Östergarnsholm measuring heights of below 30 m) while the difference higher in the atmosphere (at FINO measuring heights between 40 m and 80 m) is smaller.

The effect of applying the new parameterization in WRF is investigated for the time period of the available measurement data (i.e. 7 months for Östergarnsholm and 12 months for FINO), where the WRF simulated results are compared to the measurement data. The data are plotted first as a two dimensional probability density plots ($\Delta P/P$ for each grid point in the plot, where P is the variable under consideration), as a function of measurements (x -axis) and simulations (y -axis) as shown on the left hand side of the Fig. 5.13. Data lying on the upper-left corner of the plot (region number 2 in left hand side Fig. 5.13) represents the

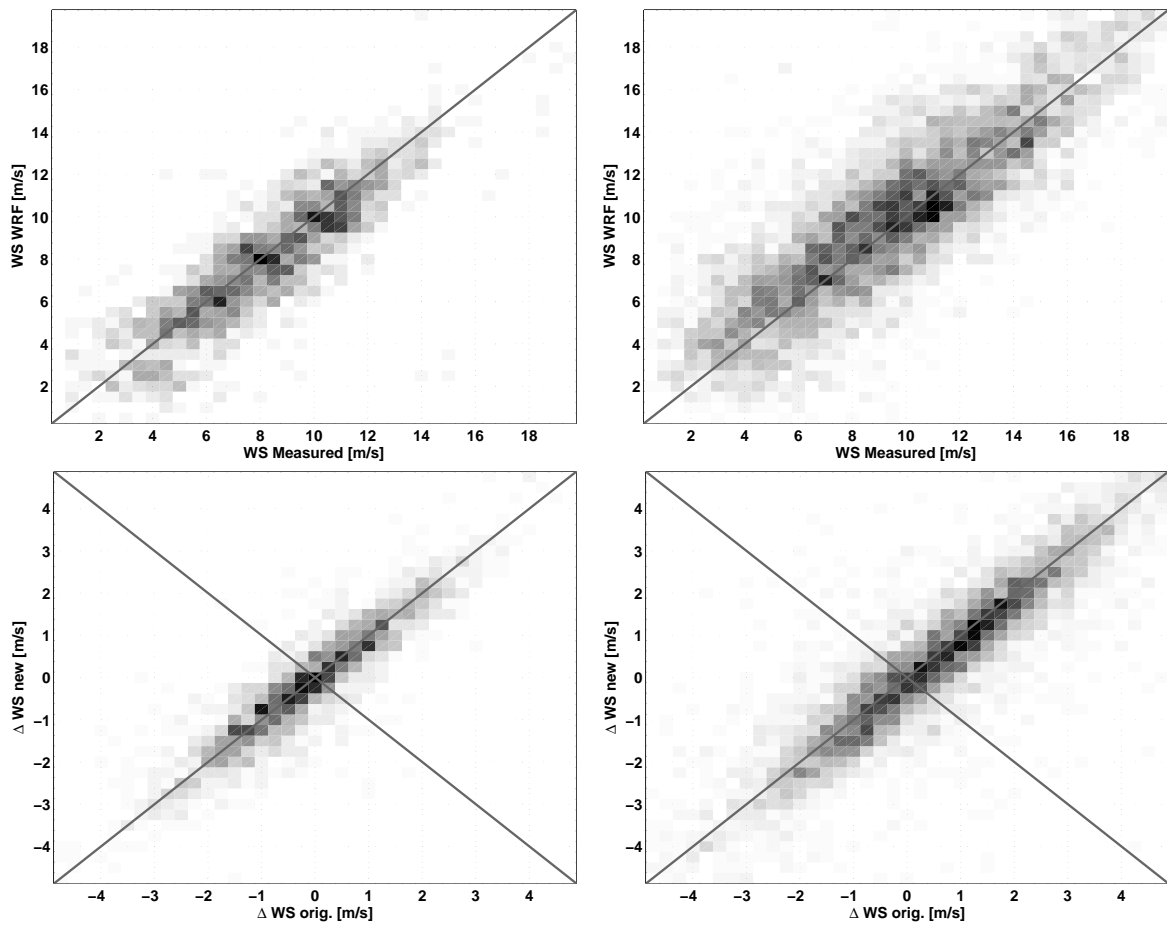


Figure 5.14: Comparison of measured and simulated wind speeds. Left hand side figures for WRF and FINO at level of 80 m and right hand side for Östergarnsholm and FINO at level 5 (28.8 m). In the upper two figures, measurements are compared to simulations from the control WRF, in the lower two the difference between the control WRF results and measurements (x -axis) and between new WRF and measurements (y -axis) is shown.

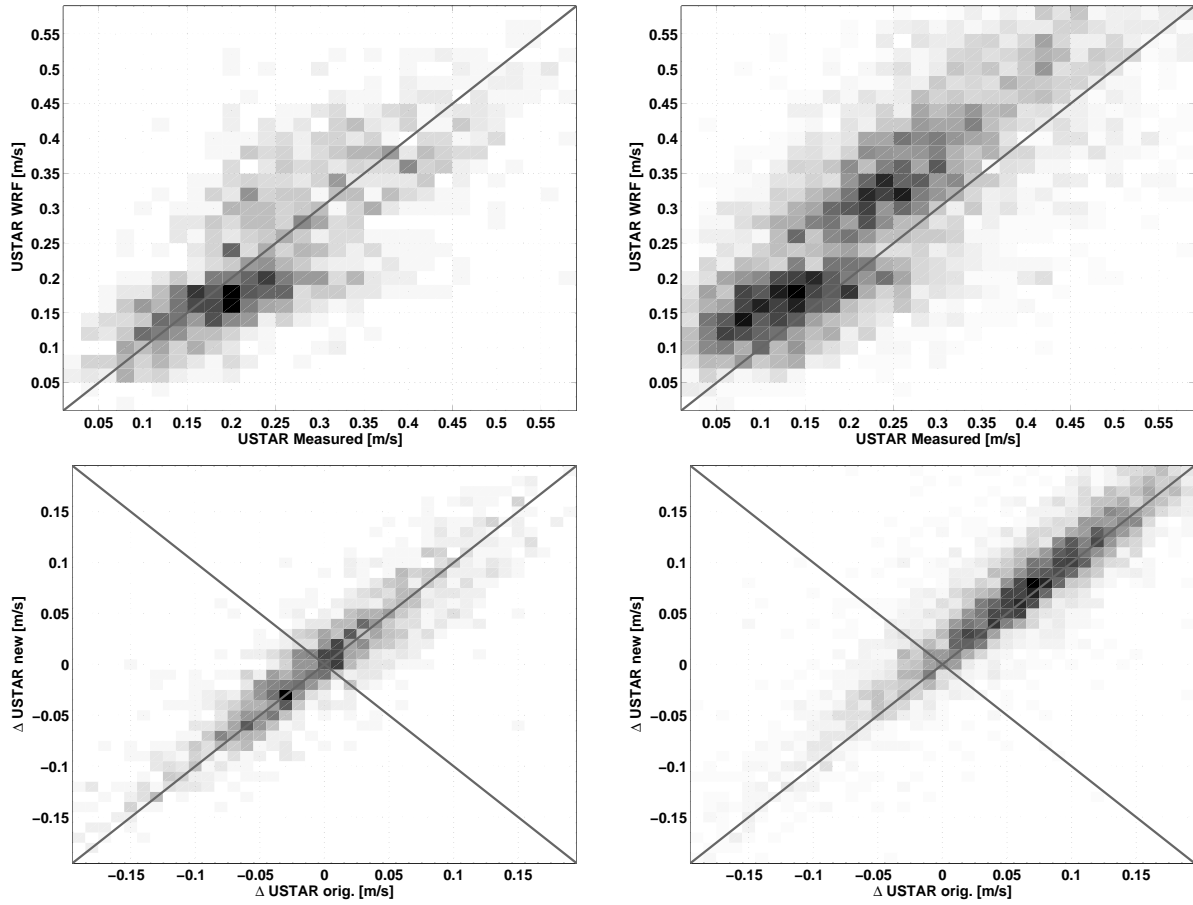


Figure 5.15: Same as Fig. 5.14, only for u_* .

cases where the simulated values were higher than measured, while the data that lay on the lower right corner represent cases where the simulation values were lower than measurements. To compare the improvement respectively worsening of the new parameterization compared to the control one, the two dimensional *pdf* of the difference between the results from the control simulations and measurements (on x -axis) and difference between the results from the new simulations and measurements (on y -axis) are plotted as shown on the right hand side of Fig. 5.13, where Δ represent the difference between simulation results and measurements. For the data, that lay in the section 1 on the right hand side of the Fig. 5.13, results from the control parameterization agree better to the measurements than results from the new one. For the data that lay in sections 2 and 3, the results from the new parameterization agrees better to the measurements. The data in section 2 represent the data where the sign of the difference between measurements and new parameterization results changed compared to the difference between control results and measurements (i.e. the correction of the new parameterization is too strong).

The wind speeds are almost equally well simulated by new or the control version of WRF at both measurement towers. At both measuring platforms, the root mean square error of the simulated wind speed (*rmse*) for the control and new parameterization differ less than 0.1 m s^{-1} (Tab. 5.2). Fig. 5.14 compares the measured and simulated wind speeds at the

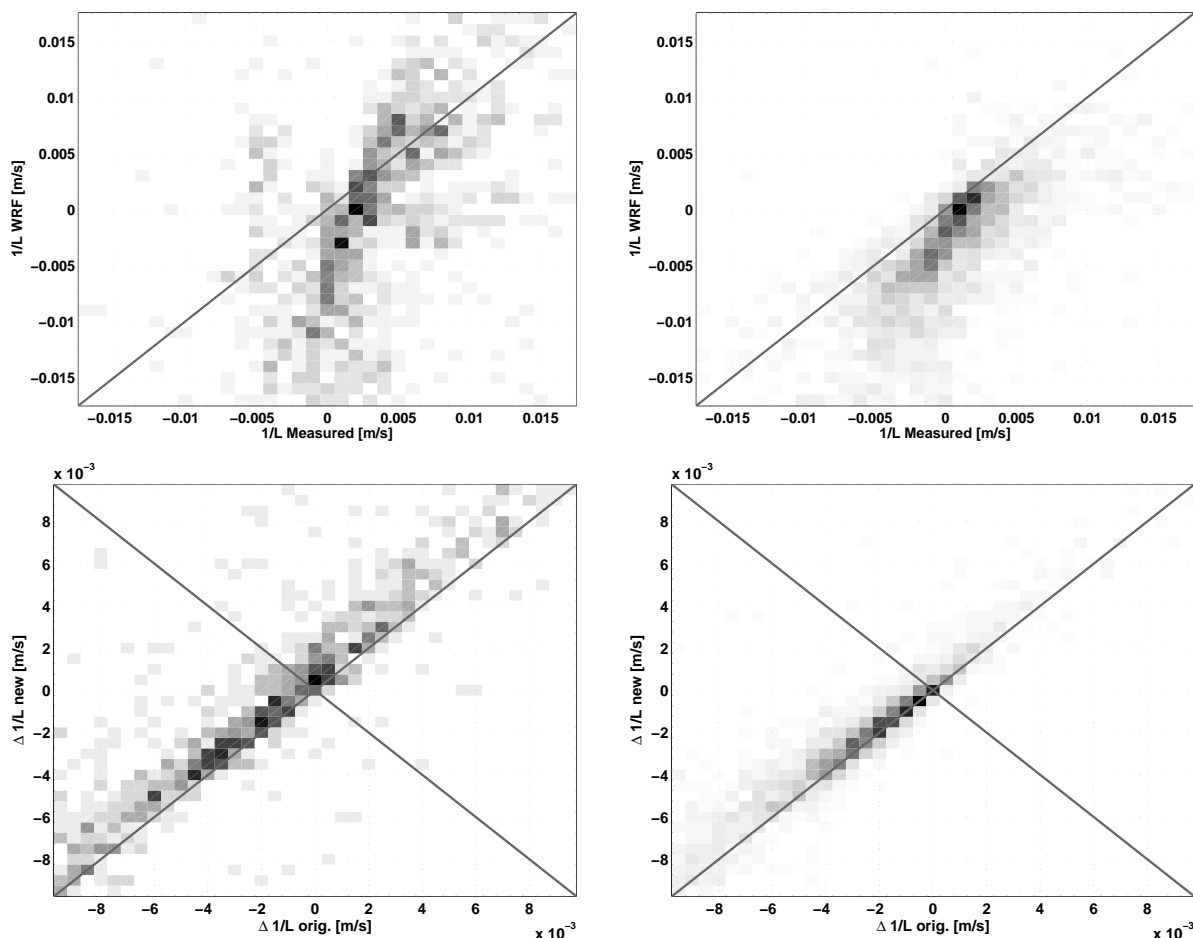


Figure 5.16: Same as Fig. 5.14, only for $1/L$.

upper measuring levels, where it is again confirmed that changing the parameterization from the control to the new did not improve the mean horizontal wind speeds. It can also be seen from Fig. 5.14 that the high and low wind speeds are equally well simulated by WRF.

As shown in previous subsection, the new parameterization is more accurate compared to the control one in reproducing the wind shears close to the surface. Since lower boundary conditions, characterized by surface friction velocity (u_*) and inverse of surface Obukhov length ($1/L$), are important in defining structure of the lower part of the boundary layer, they are compared first. The boundary layer profiles crucially depend on the surface forcing, where improvement of the parameterization is essentially a function of $1/L$. The surface forcing parameters (u_* and $1/L$) are partly determined by the surface layer parameterization and partly by the coupling of the atmosphere with the ocean (through the parameterization of the diffusion layer) and Charnock relationship as well as the assimilated SST. The comparison of the measured u_* from WRF and measurements is shown on Fig. 5.15. For the Östergarnsholm measuring period, the u_* from control version of WRF agree well with the measurements, although the scattering between the observation and WRF simulation is considerable. The scattering can be partly related to the inadequate estimation of the friction velocity by the Charnock relationship. At FINO, the simulated u_* is on average higher than measured. The

	<i>Stable</i>	<i>Unstable</i>	<i>Neutral</i>	<i>All</i>
FINO between height of 80 m and 40 m				
orig.	3.07	1.17	1.50	1.84
new	3.06	1.07	1.47	1.79
FINO between height of 80 m and 60 m				
orig.	3.91	3.20	6.51	5.00
new	3.87	3.15	6.52	4.98
Östergarnsholm between levels 5 and 3				
orig.	2.89	2.44	2.16	2.43
new	2.58	1.81	1.97	2.13
Östergarnsholm between levels 5 and 4				
orig.	3.54	2.29	2.32	2.71
new	2.87	1.76	1.94	2.21

Table 5.3: Root mean square error (*rmse*) of wind shear [$1/100 \text{ s}^{-1}$] from WRF for stable ($1/L > 0.005 \text{ m}^{-1}$), unstable ($1/L < -0.005 \text{ m}^{-1}$), neutral ($0.005 \text{ m}^{-1} < 1/L < 0.005 \text{ m}^{-1}$) and all.

reason may be that u_* from FINO which is obtained from 40 m level does not represent the surface conditions properly. It is expected and observed that the u_* is decreasing with height (e.g. Gryning et al., 2007). At both measuring platforms, the WRF results with the new parameterization did not considerably change the friction velocity u_* . The result is not surprising since in the SCM simulations it was shown that the surface turbulent fluxes (also u_*) do not considerably differ between the control and the new parameterization. The $1/L$ obtained from the control simulations agree relatively well with measured $1/L$ at both platforms in the stable range ($L > 0$), although there is slight consistent underestimation of the stability (i.e. the measured $1/L$ is consistently smaller than observed) (Fig. 5.16). In the unstable range ($L < 0$), the WRF results show consistently more unstable atmosphere (measured L is smaller than simulated). We confirmed that the stability dependent deviation is a result of the inadequate representation of the heat flux (not shown), where in the stable range the simulated heat flux is systematically too high and in the unstable range it is systematically too low. Changing the parameterization did not alter the heat flux and thus also not the simulated $1/L$ considerably. The deviation of the heat flux is not necessarily a problem of the PBL parameterization, since it is strongly determined by the temperature difference between the bottom of the atmosphere and the SST as well as with the parameterization of the diffusive layer. If the heat flux, or Obukhov length deviates too much from the observations, the new parameterization may not yield better results since the correction depends mainly on the Obukhov length.

The comparison of the measured and simulated wind shear is shown in Tab. 5.3 (dependent on stability) and on the Fig. 5.17. The improvement of the new parameterization at FINO is only marginal in all stability cases. Based on the case studies this is expected result. It was shown that the wind shear between the new and control parameterization does not differ considerably at FINO measuring levels (between 40 m to 80 m). At Östergarnsholm, the improvement of the wind shear in the new parameterization is observed for all stability cases. In the stable cases (roughly, the areas of high wind shear in Fig. 5.17), the wind shear from

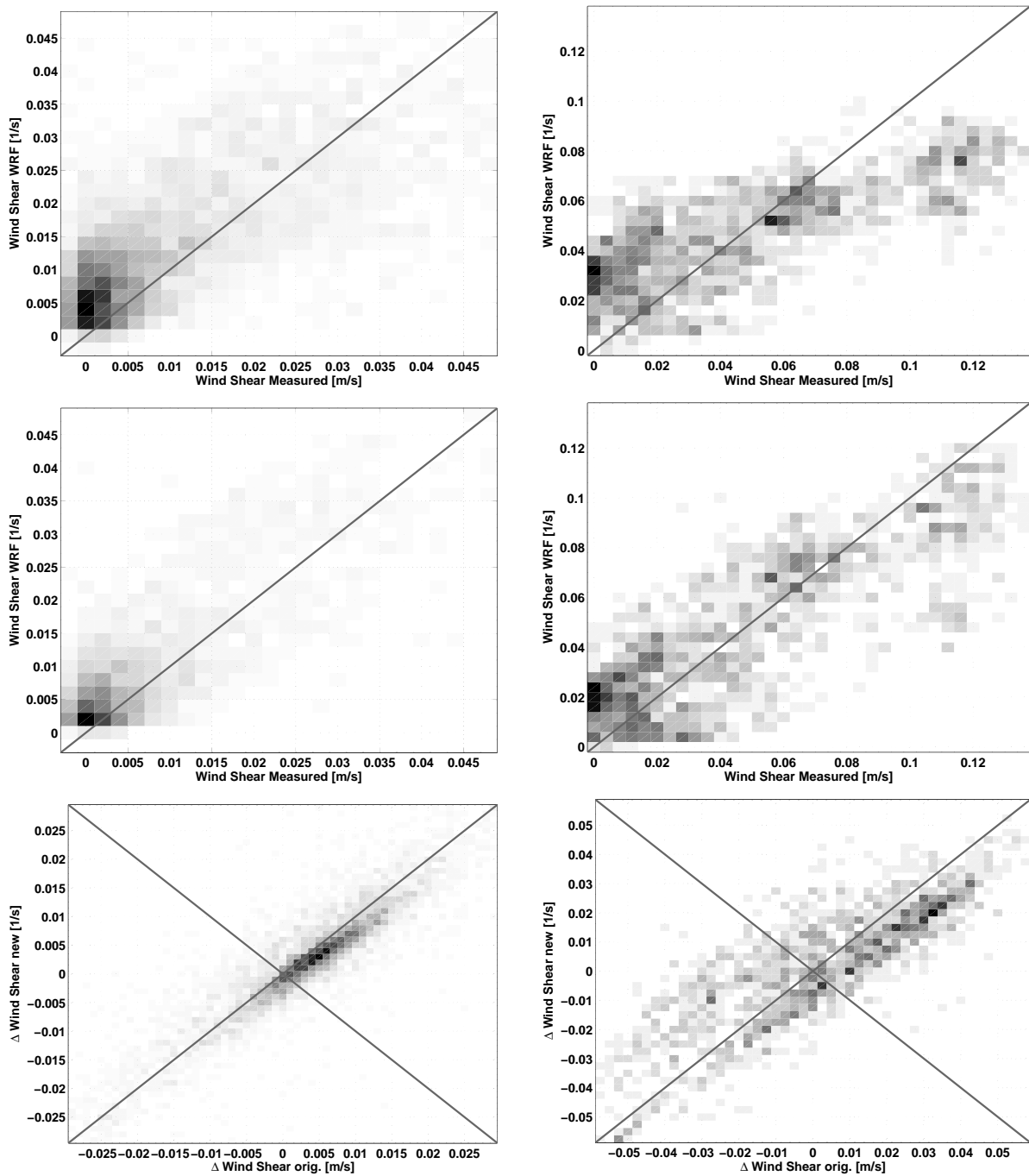


Figure 5.17: Comparison of measured and simulated wind shears ($\Delta WS/\Delta z$). Left hand side figures for WRF between level of 80 m and 40 m, right hand for Östergarnsholm between level 5 and 4. In the upper two figures, measurements are compared to simulations from the control WRF, in the middle measurements are compared to the new WRF and in the lower the difference between the control WRF results and measurements (x -axis) and between new WRF and measurements (y -axis) is shown.

the control parameterization is too small which considerably improved in the results of the new parameterizations. In the unstable cases (the areas of the low wind shear in Fig. 5.17), the control parameterization yields too high wind shears which are decreased in the results of the new parameterization. The improvement is also seen by smaller *rmse* of the wind speed difference between measuring levels from the new parameterization compared to the control one. Similar improvements of the new scheme were obtained (not shown) when the simulated wind shears were compared for the periods when the simulated u_* and $1/L$ differ for less than 15% of their standard deviation from the measured. This confirms that the improvement of the description of the boundary layer wind does not come from the (wrong) specification of the surface conditions but from the better representation of the boundary layer turbulence by the new scheme.

5.6 Discussion and conclusions

Mellor-Yamada-Janjić (MYJ) surface (level 2) and boundary (level 2.5) layer parameterization implemented in the WRF model was improved in order to obtain better representation of the wind conditions in approximately lower hundred meters of Marine Planetary Boundary Layer (MPBL). From available surface/boundary layer schemes in WRF, MJY scheme was chosen as the most promising since it was shown that the *TKÉ* based schemes have, in general, a better description of the boundary layer physics and are able to reproduce the vertical profiles of wind and potential temperature better than the other two available first order (*K*-theory) schemes (e.g. Alapaty et al., 1997). However, the simulated wind shear from the control simulation (from original WRF model) shows consistent deviations with respect to the tower measurements in the North Sea and Baltic Sea. In case of the stable (unstable) surface layer⁴, the simulated wind shear was consistently lower (higher) than the observed. The differences between the simulation results and observations were more pronounced closer to the surface (in measurements at Östergarnsholm in the Baltic Sea where the height of measurements was up to 30 m) than higher in the boundary layer (in measurements at FINO where the height of measurements was between 40 m and 80 m).

The inadequate parameterization of the surface and lower boundary layer was identified as the most probable cause for the deviation between the measured and simulated wind shear. In order to improve the simulated wind shear, the MYJ surface and boundary layer parameterization was modified by changing the Master Length Scale (MLS) which is a parameter controlling the turbulent diffusion and dissipation, pressure-strain and pressure-temperature covariances. Both the closure assumptions and subsequently the definition of MLS are the weaknesses of the scheme. Many definitions of the MLS exist some of them are cited in the introduction of this paper. In the control MYJ scheme, the Prandtl mixing length scale is used as the MLS in the surface layer and the combination of the Prandtl mixing length and the length based on the bulk turbulent property of the boundary layer is used as the MLS in the proper boundary layer (from the first model level to the top of the boundary layer) (Mellor and Yamada, 1982). The new surface layer MLS is stability dependent and mimics the enhancement (suppression) of the mixing efficiency in the unstable (stable) surface layer. In the proper boundary layer, the new MLS is the combination of the stability adjusted Prandtl mixing length, the length based on the bulk turbulent property of the boundary layer and the length limiting the MLS due to the non-local surface forcing in the statically stable boundary

⁴Surface stability was characterized with the inverse Obukhov length ($1/L$).

layer. Based on the high resolution wind measurements at FINO, we estimated that the MLS is dependent on the stability. Although a lot of assumptions were made to estimate the MLS from FINO measurements, the estimated length scale well agrees with the one from Nakanishi (2001).

The wind speed itself is not much dependent on the parameterization used with the exception of only a few meters above the ground. There are other sources that cause inaccuracies of the modelled wind speed, such as the poorly resolved mesoscale field used as initial and lateral boundary conditions for WRF model. The improvement of the mesoscale field description may be achieved by the assimilation of the observational data such as from the nearby measurement stations (e.g. Ruggiero et al., 1996), or assimilating the satellite measurements for example from the surface winds (Atlas et al., 2001). However the parameterization affects the near-surface wind shear. With the help of the idealized single column (SCM) simulations, it was shown that in the case of the stable (unstable) surface layer the vertical turbulent exchange coefficients in the new parameterization near the surface are lower (higher) compared to the control one. Lower (higher) near surface exchange coefficients are partially compensated by higher (lower) wind shears and potential temperature vertical gradients, which results in only slight difference of the near surface turbulent fluxes between the control and the new parameterization. The new parameterization yield considerably different wind shears from the control one in the first few tens of meters while higher in the boundary layer the difference is smaller. Compared to the observational data, the wind shear from the new parameterization shows considerably closer agreement with the measurements close to the ground (up to around 30 m, at Östergarnsholm). Higher in the boundary layer (between 40 m and 80 m, at FINO), the improvements are less evident. However, at the FINO measurement levels, the wind shear is usually smaller and thus the measured wind shear is more prone to the measurement errors than closer to the ground.

The change of the surface and boundary layer presented here was relatively simple in terms of adjusting the WRF code. The introduction of the higher order MJY scheme (e.g. Nakanishi, 2001) in the boundary layer by including new terms would be able to represent the boundary layer physics in more accurate details and thus possibly predict the wind profiles better. To change the surface layer scheme more than by just redefining integrated stability functions fundamental adjustments of the code would be required. On the other hand even simpler adjustments of the original MJY scheme by changing the values of the parameters B_1 and S_q controlling the rate of the diffusion and dissipation of the TKE in (Eq. 5.27) as well as α in the definition of the MLS (Eq. 5.2) was not successful. We were not able to obtain the stability dependent corrections of the wind shear since by improving the wind shear in the case of the stable (unstable) layer, the wind shear in unstable (stable) was worsened.

It was observed that the new parameterization, as well as the control one is very sensitive to the correct specification of the lower boundary condition for the surface layer. The new parameterization is even more sensitive to the surface stability than the original since it is explicitly used in the definition of MLS. The adjustment of the boundary layer parameterization was tested in the MPBL since the lower boundary condition is relatively homogeneous compared to the land case where even small undulations of the terrain and vegetation heterogeneity complicates the land-atmosphere interaction. However in case of the MPBL the dynamical interaction between the sea and the atmosphere must be taken into an account, which mainly influence the momentum transfer between sea and atmosphere. In the current version of WRF, the momentum forcing from the sea to the atmosphere is described by relatively rough Charnock relationship. There is evidence that coupling the wave model to the

atmospheric model is required to describe the dynamical coupling of the atmosphere to the ocean which also improves the low level winds (Desjardins et al., 2000). The heat forcing is controlled by the accurate specification of the SST and the diffusion layer parameterization. It was found that in the Baltic Sea the relatively highly spatially resolved SST was needed in order that the surface heat forcing was properly described.

Acknowledgements

The work shown here was supported by the EU program Marie-Curie, Early Stage Researcher Program Modobs (MRTN-CT-2005-019369) and OWEA project supported by German federal Ministry for Environment, Nature conservation and Nuclear Safety. The tower measurement data was provided by the University of Uppsala and German Wind Energy Institute, the SST in the Baltic Sea by German Federal Maritime and Hydrographic Agency and the FNL data by US National Centers for Environmental Prediction. We are also grateful to the developers of WRF for providing the model for public use. We thank A. Rutgersson for the useful comments on the manuscript and preparing the Östergarnsholm observational data set used in this study.

5.A MYJ equations in WRF model

The equations of the MYJ level 2.5 model which is used as a boundary layer parameterization and MYJ level 2 model used for the surface layer parameterization are given. More details can be found in Mellor and Yamada (1974, 1982) and Janjić (2002). The boundary layer parameterization estimates turbulent exchange coefficients for momentum (K_M) and heat (K_H):

$$\overline{u'_i w'} = -K_M \frac{\partial u_i}{\partial z} \text{ where } i = 1, 2 \quad (5.19)$$

$$\overline{w' \theta'} = -K_H \frac{\partial \theta}{\partial z} \quad (5.20)$$

The nondimensional variables are defined: wind shear (G_M), vertical potential temperature gradient (G_H), diffusion coefficients for momentum and heat (S_M and S_H , respectively):

$$G_M = \frac{l^2}{q^2} \left[\left(\frac{\partial U}{\partial z} \right)^2 + \left(\frac{\partial V}{\partial z} \right)^2 \right] \quad (5.21)$$

$$G_H = \frac{l^2}{q^2} \beta g \frac{\partial \Theta}{\partial z} \quad (5.22)$$

$$S_M = \frac{\overline{w' u'_i}}{l q \frac{\partial U_i}{\partial z}} \quad (5.23)$$

$$S_H = -\frac{\overline{w' \theta'}}{l q \frac{\partial \theta}{\partial z}} \quad (5.24)$$

5.A. MYJ EQUATIONS IN WRF MODEL

where l is the Master Length Scale and q^2 Turbulent Kinetic Energy (TKE $q^2 = \frac{1}{2}\overline{u_i'^2}$)⁵. The MYJ level 2.5 model can be written with two algebraic equations relating the nondimensional wind shear and vertical potential temperature and prognostic equation for TKE :

$$S_M(6A_1A_2G_M) + S_H(1 - 3A_2B_2G_H - 12A_1A_2G_H) = A_2 \quad (5.25)$$

$$S_M(1 - 6A_1^2G_M - 9A_1A_2G_H) - S_H(12A_1^2G_H + 9A_1A_2G_H) = A_1(1 - 3C_1) \quad (5.26)$$

$$\frac{\partial q^2}{\partial t} + U_i \frac{\partial q^2}{\partial x_i} = \frac{\partial}{\partial z} \left(lqS_q \frac{\partial q^2}{\partial z} \right) = -\overline{w'u'} \frac{\partial U}{\partial z} - \overline{w'v'} \frac{\partial V}{\partial z} + \beta g \overline{\theta'w'} - \frac{q^3}{B_1 l} \quad (5.27)$$

The values of parameters A_1 , A_2 , B_1 , B_2 , C_1 and S_q are given in Janjić (2002). Turbulent exchange coefficients (K_M and K_H) and consequently the turbulent fluxes can be calculated from the Eqs. 5.25 - 5.27, using the definitions of nondimensional vertical gradients. The MYJ, level 2.5 scheme is known to be numerically unstable in case of the rapidly growing or rapidly decaying turbulence due to the assumptions of near-isotropy of the turbulent fluxes (e.g. Helfand and Labraga, 1988). Janjić (2002) solved the instability problem by imposing upper limit to the MLS, which is the function of the local TKE .

MYJ level 2 model is obtained by assuming local equilibrium between production and dissipation of TKE . With this assumption the prognostic equation for the TKE simplifies to the algebraic equation. The flux Richardson number (R_f) which represent the surface stability is defined as:

$$R_f = \frac{\frac{g}{\Theta} \overline{\theta'w'}}{\overline{u_i'u_j'} \frac{\partial U_i}{\partial x_j}} \quad (5.28)$$

The nondimensional diffusion coefficients for momentum and heat are expressed as:

$$S_M = 3A_1 \frac{\gamma_1 - C_1 - (6A_1 + 3A_2)\Gamma/B_1}{\gamma_1 - \gamma_2\Gamma + 3A_1\Gamma/B_1} (\gamma_1 - \gamma_2\Gamma) \quad (5.29)$$

$$S_H = 3A_2(\gamma_1 - \gamma_2\Gamma) \quad (5.30)$$

Where new stability function (Γ) and constants are:

$$\Gamma = \frac{R_f}{1 - R_f} \quad (5.31)$$

$$\gamma_1 = \frac{1}{3} - \frac{2A_1}{B_1} \quad (5.32)$$

$$\gamma_1 = \frac{B_2 + 6A_1}{B_1} \quad (5.33)$$

In the WRF model, the surface layer is written based on the Monin-Obukhov (MO) similarity theory. Łobocki (1993) showed that MY level 2 can be expressed in terms of the MO

⁵Dashes represent anomalies from Reynolds averaged values and other variables have their usual meaning.

similarity theory with the proper surface stability functions. In WRF instead of the surface stability functions from MYJ level 2 model, Paulson integrated stability functions are used (Chen et al., 1997) in the unstable surface layer (Chen et al., 1997) and stability functions from Holtslag and de Bruin (1988) in the stable.

Over the sea the boundary condition for the momentum, heat and moisture at the lower surface layer is related to the surface values through the parameterization of the thin diffusive layer (Liu et al., 1979; Janjić, 1994). The diffusive layer exists only when the friction velocity is small enough, i.e. the sea is smooth. The Sea Surface Temperature (SST) is prescribed as the boundary condition and is kept constant through the simulation period. The roughness length is calculated using the Charnock relationship (Janjić, 1994) from the friction velocity.

Bibliography

- Alapaty, K., J. E. Pleim, S. Raman, D. S. Niyogi, and D. W. Byun, 1997: Simulation of atmospheric boundary layer processes using local- and nonlocal-closure schemes. *J. Appl. Meteorol.*, **36**, 214–233.
- Atlas, R., et al., 2001: The effects of marine winds from scatterometer data on weather analysis and forecasting. *Bull. Am. Meteorol. Soc.*, **82** (9), 1965–1990.
- Blackadar, A. K., 1962: The vertical distribution of wind and turbulent exchange in a neutral atmosphere. *J. Geoph. Res.*, **67**, 3095–3102.
- Canuto, V. M., Y. Cheng, and A. Howard, 2001: New third-order moments for the convective boundary layer. *J. Atmos. Sci.*, **58**, 1169–1172.
- Chen, F., Z. Janjić, and K. Mitchell, 1997: Impact of atmospheric surface-layer parameterizations in the new land-surface scheme of the NCEP mesoscale ETA model. *Boundary-Layer Meteorol.*, **85**, 391–421.
- Cheng, Y., V. M. Canuto, and A. M. Howard, 2002: An improved model for the turbulent PBL. *J. Atmos. Sci.*, **59**, 1550–1565.
- Davidson, P. A., 2006: *Turbulence An Introduction for Scientists and Engineers*. Oxford University Press.
- Desjardins, S., J. Mailhot, and R. Lalbeharry, 2000: Examination of the impact of a coupled atmospheric and ocean wave system. Part i: Atmospheric aspects. *J. Phys. Oceanogr.*, **30**, 385–401.
- Gryning, S.-E., E. Batchvarova, B. Brümmer, H. Jørgensen, and S. Larsen, 2007: On the extension of the wind profile over homogeneous terrain beyond the surface boundary layer. *Boundary-Layer Meteorol.*, **124**, 251–268.
- Helfand, H. M. and J. C. Labraga, 1988: Design of a nonsingular level 2.5 second-order closure model for the prediction of atmospheric turbulence. *J. Atmos. Sci.*, **45** (2), 113–132.
- Holtslag, A. A. M. and H. A. R. de Bruin, 1988: Applied modeling of the nighttime surface energy balance over land. *J. Appl. Meteorol.*, **27**, 689–704.
- Hong, S.-Y. and H.-L. Pan, 1996: Nonlocal boundary layer vertical diffusion in a Medium-Range Forecast model. *Mon. Weather Rev.*, **124**, 2322–2339.
- Janjić, Z., 1994: The step mountain ETA coordinate model: Further development of the convection, viscous sublayer and turbulence closure scheme. *Mon. Weather Rev.*, **122**, 927–945.
- Janjić, Z., 2002: Nonsingular implementation of the Mellor-Yamada level 2.5 scheme in the NCEP meso model. *NCEP Office Note*, **No. 437**.
- Lenderink, G. and A. A. M. Holtslag, 2004: An updated length-scale formulation for turbulent mixing in clear and cloudy boundary layers. *Q. J. R. Meteorol. Soc.*, **130**, 3405–3427.

BIBLIOGRAPHY

- Liu, W. T., K. B. Katsaros, and J. A. Businger, 1979: Bulk parameterization of air-sea exchanges of heat and water vapor including the molecular constraints at the interface. *J. Atmos. Sci.*, **36**, 1722–1734.
- Lobocki, L., 1992: Mellor-Yamada simplified second-order closure models: analysis and application of the generalized von Karman local similarity hypothesis. *Boundary-Layer Meteorol.*, **59**, 83–109.
- Lobocki, L., 1993: A procedure for the derivation of surface-layer bulk relationship from simplified second-order closure models. *J. Appl. Meteorol.*, **32**, 126–138.
- Mellor, G. L., 1973: Analytic prediction of the properties of stratified planetary surface layers. *J. Atmos. Sci.*, **30**, 1061–1069.
- Mellor, G. L. and T. Yamada, 1974: A hierarchy of turbulence closure models for planetary boundary layers. *J. Atmos. Sci.*, **31**, 1791–1806.
- Mellor, G. L. and T. Yamada, 1982: Development of a turbulence closure model for geophysical fluid problems. *Rev. Geophys. Space Phys.*, **20**, 851–875.
- Moeng, C. and J. C. Wyngaard, 1989: Evaluation of turbulent transport and dissipation closures in second-order modeling. *J. Atmos. Sci.*, **46** (14), 2311–2330.
- Nakanishi, M., 2001: Improvement of the Mellor–Yamada turbulence closure model based on large-eddy simulation data. *Boundary-Layer Meteorol.*, **99**, 349–378.
- Neumann, T., K. Nolopp, and K. Herklotz, 2004: First operating experience with the FINO1 research platform in the North Sea. *DEWI Magazine*, **24**.
- Richardson, M. I., A. D. Toigo, and C. E. Newman, 2005: Non-conformal projection, global and planetary versions of wrf. *6th WRF / 15th MM5 Users' Workshop*, URL www.mmm.ucar.edu/wrf/users/workshops/WS2005/abstracts/Session7/1-Richardson.pdf.
- Ruggiero, F. H., K. D. Sashegyi, R. V. Madala, and S. Raman, 1996: The use of the surface observations in four-dimensional data assimilation using a mesoscale model. *Mon. Weather Rev.*, **124**, 1018–1033.
- Rutgersson, A., A.-S. Smedman, and Högström, 2001a: Use of a conventional stability during swell. *J. Geoph. Res.*, **27** (134), 117–134.
- Rutgersson, A., A.-S. Smedman, and A. Omstedt, 2001b: Measured and simulated latent and sensible heat fluxes at two marine sites in the baltic sea. *Boundary-Layer Meteorol.*, **99**, 53–84.
- Sjöblom, A. and A.-S. Smedman, 2003: Vertical structure in the marine atmospheric boundary layer and its application for the inertial dissipation method. *Boundary-Layer Meteorol.*, **109**, 1–25.
- Skamarock, W. C., J. B. Klemp, J. Dudhia, D. O. Gill, D. M. Barker, W. Wang, and J. G. Powers, 2005: A description of the advanced research wrf version 2. Tech. rep., NCEP/NCAR. URL http://www.mmm.ucar.edu/wrf/users/docs/arw_v2.pdf.

- Smedman, A.-S., U. Högström, H. Bergström, A. Rutgersson, K. Kahma, and H. Pettersson, 1999: A case study of air-sea interaction during swell conditions. *J. Geoph. Res.*, **25** (104), 25 833–25 851.
- Stull, R. B., 1988: *An Introduction to BLM*. Kluwer Academic Publishers.
- Therry, G. and P. Lacarrère, 2002: An improved model for the turbulent PBL. *J. Atmos. Sci.*, **59**, 1550–1565.
- Umlauf, L. and H. Burchard, 2003: A generic length-scale for geophysical turbulence models. *J. Mar. Res.*, **61**, 235–265.
- Vickers, D. and L. Mahrt, 1997: Quality control and flux sampling for tower and aircraft data. *J. Atmos. Oceanic Technol.*, **14**, 512–526.
- Vickers, D. and L. Mahrt, 2003: The cospectral gap and turbulent flux calculations. *J. Atmos. Oceanic Technol.*, **20**, 660–672.
- Wilczak, J. M., S. P. Oncley, and S. A. Stage, 2001: Sonic anemometer tilt correction algorithms. *Boundary-Layer Meteorol.*, **99**, 127–150.
- Zilitinkijevich, S., I. Esau, and A. Baklanov, 2007: Further comments on the equilibrium height of neutral and stable planetary boundary layers. *Q. J. R. Meteorol. Soc.*, **133**, 265 – 271.

BIBLIOGRAPHY

6

Summary and General Conclusions

Wind energy is a relatively new industrial sector providing clean and renewable electricity. The north-western Germany is a region with abundant wind energy resources. Therefore, an increase of utilization of wind energy in Germany has been almost exponential over the last decade. Renewable energies, including wind help to decrease demand of energy from fossil fuels and thus help to combat the global climate change. Above all, technological development within the wind energy sector contributes to technological progress also providing new jobs in a new wind industry sector while reducing dependency on fossil fuels. It is expected that in the next decades, most suitable onshore locations for wind energy in Germany will be exhausted. Therefore, a tremendous growth of offshore wind energy (in North Sea and Baltic Sea) is foreseen. Modern wind turbines convert the kinetic energy of the wind to the electricity. The knowledge of the near-surface wind conditions is crucial for planning and operating wind farms. In addition, extreme wind conditions are important for risk assessment. In this work, we tackled some questions related to i) estimation of wind resources mainly over North Sea on different time scales (Ch. 3), ii) possible change of wind resources over the Northern Atlantic and Europe in the future climate (Ch. 4) and, iii) numerically modelling of the near surface wind speeds (Ch. 5).

The wind resource estimation (i.e. the mean Near Surface Wind Speed (WS) and its variability) of the specific wind farm location must be performed in the early stage of its planning in order to predict the produced wind power and thus the feasibility of wind farm. Estimating wind resources over the North Sea is complicated since only a few and relatively short time series of WS measurements exist. Therefore, one has to depend on the simulations by the numerical models such as the atmospheric reanalysis datasets. In the first part of the thesis (Ch. 3), we compared how well WS is represented in the different reanalysis datasets. It was clearly shown that the mean WS crucially depends on the details of the reanalysis model, specifically on the parameterization of the boundary layer and other surface processes. For example, the mean WS at 10 meters height (WS10) over the German Bight from two similar reanalysis models (NCEP and NCEP2) differ around 2 m s^{-1} (at mean WS10 of $\sim 6 \text{ m s}^{-1}$ - 10 m s^{-1}) (Fig. 3.1), where the main difference between those two models is the parameterization of a boundary layer. On the other hand, the time-variability of the WS10 among different reanalysis datasets agree well. Above all, the variability of WS10 over the Northern Europe is not crucially dependent on the model resolution (except at the coastline), since WS10 is spatially well correlated. The high spatial correlation of WS10 is not optimal for large scale wind energy utilization, since all wind turbines in a North-European region would have a same tendency of a produced power leading to high fluctuations of total produced wind power. This might be different when considering the wind variability on the whole European scale. The reason for high spatial correlation of WS10 variability over the North

CHAPTER 6. SUMMARY AND GENERAL CONCLUSIONS

Europe is that the WS10 variability is well defined by the large scale circulation patterns, which can be characterized from the Sea Level Pressure (SLP). Therefore, understanding the variability of the relevant circulation patterns is a suitable basis for understanding the variability of WS10. We found that most of the WS10 variability over the Northern Europe can be described by three circulation patterns defined as a SLP difference between i) the South-Western Europe and Iceland, ii) Scandinavia and Iceland and, iii) Scandinavia and North Atlantic (Sec. 3.3.2). Similarly, the extreme WS10 over German Bight have been related to different circulation patterns (Sec. 3.3.3). The extreme WS10 was found to be related to only one extreme circulation pattern, which is described by the anomalously low SLP over Scandinavia. However, the time series of the circulation pattern and the extreme WS10 were significantly different in terms of the trend and long term variability in the latest few decades. Namely, the interannual to decadal variability of the extreme circulation pattern was surprisingly low compared to the extreme WS10. This result indicates that the extreme WS10 over German Bight from the reanalysis is not reliable. Above all, the result helps to clarify the controversy of the extreme WS trend in the recent literature (more details can be found in Sec. 3.3.3 and Sec. 3.4). Some researchers based on the measured WS, argued that they found a significant trend of extreme WS over last decades, while others estimated the trend from the SLP patterns and argued that the trend of the extreme WS was not present.

Although a possible change of the near-surface wind climate can have a prominent impact on produced wind power, the influence of the climate change on wind resources has not yet been fully investigated. Therefore, in the second part of this thesis (Ch. 4) the climate change of the WS over the North Atlantic and Europe was estimated. Earth climate can be simulated with a Global Circulation Models (GCMs), which describe the dynamics and the physics of the atmosphere and couple it to ocean, land and ice. The development and simulations of the climate with GCMs is extremely expensive. Therefore, only few climate centres worldwide can afford to do it. Intergovernmental Panel on Climate Change (IPCC) is an international body which encourages the climate research and evaluates the impact of the climate change on the society, based mainly on the results of the ensemble of GCMs. The results of the GCM simulations used for the last (fourth) IPCC report are freely available for the research community, but unfortunately WS is not one of the accessible parameters. In this work, we estimated the climate change of the WS based on the climate change of the relevant SLP based large scale patterns. Our approach was to find the relevant WS patterns and relate them to the SLP circulation patterns in the past climate (based on reanalysis data used as a replacement for the measurements). To estimate the climate change of WS, we compare the change of time series of SLP patterns as simulated by an ensemble of GCM simulations of the past to future climate and relate the change of time series of SLP patterns to the change in the magnitude of WS. For the past climate, we used GCM results forced by the observed concentrations of greenhouse gasses and for the future climate the results are based on the IPCC A2 greenhouse gas scenario. IPCC A2 scenario represents a more divided world with a slower technological change and is one of the high IPCC emission scenarios. Different WS and SLP patterns than the ones found in Ch. 3 were searched for the following reason. The patterns in Ch. 3 were optimized to explain the highest possible variance of WS data in order to describe most of the WS variability. Now that we are searching for the highest change in the WS, the new WS modes are optimized to explain the largest part of the WS trend which on the multidecadal time scales leads to climate change of WS. The whole analysis was performed for each season of the year independently, since WS climate over the Europe and North Atlantic is expected to be seasonally depended mainly due to the movement of the

polar front northward (southward) in the warm (cold) part of the year. Our results showed that in every season, only one WS pattern was enough to explain the significant part of WS trend and this pattern is related to SLP pattern similar to North Atlantic Oscillation (NAO). This result is not surprising, it is well documented that NAO explains the highest part of the SLP trend in the past climate. The results from Ch. 3 indicate that the NAO like pattern explains the largest part of the WS variance, but this analysis shows that the NAO like pattern is enough to explain the significant trend of WS. Before deriving the climate change of WS, we compared the time series of the relevant SLP patterns from GCMs in the past data with the time series of the patterns obtained from the analysis of more than a century long measurements of SLP. Time series of SLP patterns from measurements and GCMs are considerably different in their variability. The time series from measured data show an important inter-annual variability and thus significant correlation from year-to-year, while the time series from the GCM patterns are random on the year-to-year basis. It has been documented in the literature that time series of NAO simulated by GCMs do not properly represent the measured long term variability of NAO. The reasons for this seem to be not yet clear (look in Sec. 4.6 for details) and are currently under investigation. Nevertheless, we estimated the change of the WS in the future climate. The most dramatic change is found in the winter season, where the expected increase of the WS over most of the Atlantic was observed. In other seasons, the change toward a decrease in WS over the north-western part of Europe and increase over the north-western Atlantic is expected. However the magnitude of those changes is lower compared to the change in winter and also not consistent among the models. The main limitation of this study, as well as any study that statistically estimates the climate change is, that the change in WS patterns observed to be significant in the past climate are considered, while the possible new WS patterns or change of the location of WS patterns from the past to the future are not accounted for. However, the study shows the the coherency of majority of the GCMs in explaining the large scale forcing responsible for climate change of WS. Results of this study could also be used to select a few representative GCM simulation results in order to describe most of the large scale variability relevant for WS forcing and refine them by dynamically downscaling.

As already discussed, the near surface wind speed simulated by numerical models is crucially dependent on the details of the model. In the atmospheric marine boundary layer, one crucial part of the model is parameterization of turbulence in Planetary Boundary Layer (PBL). In Ch. 5 we investigated how well WRF mesoscale model is suited for requirements of wind power forecasting and wind resource estimation. The PBL parameterization was carefully chosen from the available schemes in order to simulate the physics of boundary layer turbulence as well as possible. We used Mellor-Yamada-Janjić (MYJ) scheme, which is based on the prognostic equation for the Turbulent Kinetic Energy (TKE) and the turbulent mixing coefficients are a function of TKE. Hindcast simulations of the atmospheric conditions over North Sea and Baltic Sea were performed with WRF model and the results were compared to the measurements platform at i) FINO in North Sea which measures the atmospheric condition from 40 m above mean sea level to around 100 m and represents the lower part of the boundary layer; ii) Östergarnsholm in Baltic Sea which measures the atmospheric conditions below 40 m and represents roughly the surface layer. Both measuring platforms are located so that they represent open sea (marine boundary layer) conditions. WRF simulated WS agrees well with the measurements at both measuring platforms, indicating that the WRF model is suitable for the predictions or resource assessment of wind power. However, we found a bias of simulated vertical wind shear. In case of stable surface layer, the simulated vertical

wind shear was too low and in case of unstable surface layer the vertical wind shear was too high. The difference between the measurements and the simulations was most obvious at the lower heights (at Östergarnsholm). Parameterization of PBL was identified as the most probable reason for a wind shear bias. We have investigated several possibilities of adjusting the boundary layer scheme to better simulate the wind shear especially in the lower part of the boundary layer. We found that the optimal adjustment was changing the equation for master length scale which is part of MYJ scheme and controls the diffusion and dissipation of the turbulent fluxes as well as serves as a closure assumption for the pressure-strain covariance. Among others, the master length scale was made dependent on surface stability. We found an evidence in the literature as well as from the FINO measurements, that the master length scale should be stability dependent. With the adjusted parameterization, the simulated wind shear close to the surface was significantly improved. The difference between the wind shear from the original and the improved parameterization was shown to be highest close to the surface (up to around 60 m) where also the simulations poorly matched the measurements, while higher in the boundary layer the differences was less obvious.

The wind shear simulated with WRF very close to the surface (up to ~ 20 m) over the marine boundary layer can be problematic, especially in the areas of swell conditions (long waves propagating away from the area of formation), where the wave forcing on the atmosphere plays an important role. WRF cannot simulate swell forcing on the atmosphere, since it couples the atmosphere with the ocean through the simple Charnock relation, which assumes the local equilibrium between the wind and waves. In case of the propagating ocean waves and thus non-equilibrium state (swell), the ocean can feed the atmosphere with the momentum and thus influence the wind shear close to the surface. To simulate the coupling of the atmosphere to the ocean, ocean wave model would have to be run and coupled to the atmospheric model. Some improvements in the boundary layer parameterization might be achieved by accounting for intermittence in the stable boundary layer. One approach is to use the current parameterization in a stochastic way. With the stochastic parameterization, the intermittency of the turbulence as well as wind gusts can be simulated. In the convective boundary layer, numerical models parameterize turbulence with a convective parameterization and PBL parameterization separately. It has been suggested in literature that joining two parameterizations could improve the simulated structure of the convective boundary layer.

Curriculum Vitae

PERSONAL DATA

Name: Kay Sušelj
Place and date of birth: Ljubljana, December 30, 1977
Nationality: Slovene

EDUCATION

2006- Ph.D. in Physics, Carl von Ossietzky University Oldenburg
2002-2006 M.Sc. in Meteorology, University of Ljubljana
1996-2001 B.Sc. in Meteorology, University in Ljubljana

WORKING EXPERIENCE

May 2006- present Ph.D. student ForWind-Center for Wind Energy Research/Carl von Ossietzky University Oldenburg.
November 2001- Environmental Agency of the Republic of Slovenia (EARS)
May 2006
July 1999- August 1999 German Weather service (Deutsche Wetterdienst, DWD) in Braunschweig

SUMMER SCHOOLS AND OTHER COURSES (recent)

September 2007 *Summer School on Climate Modelling* organized by Max-Planck Institute (Hamburg, Germany)
May 2007 *ModObs Summer School on Air-Sea Interactions* (Castro, Italy)
September 2006 *Summer School on Boundary Layer* organized by University of Helsinki (Helsinki, Finland)
August 2006 *WRF tutorial* organized by NCEP (Colorado, USA)

KNOWLEDGE OF FOREIGN LANGUAGES

- Slovene (mother tongue)
- English (good)
- German (good)
- Croatian (spoken)

COMPUTER SKILLS

- Matlab
- Linux (with writing scripts)
- Fortran

PUBLICATIONS

Proceedings on conferences (recent)

- K. Sušelj and A. Sood: Adjusting Mellor-Yamada-Janjić boundary layer parametrization for offshore surface conditions. Abstract on EGU conference 2008
- K. Sušelj, A. Sood and D. Heinemann: North Sea surface winds in the past and future climates. Abstract on EGU conference 2008
- K. Sušelj, A. Sood and B. Canadillas: The planetary boundary layer over North Sea: measurements and mesoscale simulations. Abstract on EGU conference 2007
- K. Sušelj, V. Layec, A. Sood and L. von Bremen: Past climate and extreme events over North Sea. Proceedings of German Wind Energy Conference (DEWEK) 2006
- K. Sušelj and K. Bergant: Mediterranean oscillation index and its influence on the climate in Slovenia (in Slovene). Research from geodesy and geophysics in Slovenia, January 2006
- K. Sušelj, M.-N. Tsimplis and K. Bergant: Atmospheric forcing on Sea Surface Height variability in the Mediterranean Sea. Book of Abstracts, Workshop on Sea Level Variations, October 2005
- K. Sušelj and V. Malačič: Sea Surface Height Variability of Mediterranean Sea Related to Sea Level Pressure. Book of Abstracts, Workshop on Sea Level Variations, October 2005
- M. Kobold and K. Sušelj: Uncertainty of precipitation as an input to hydrological models (in Slovene). Research from geodesy and geophysics in Slovenia, January 2005

Articles in peer-reviewed journals

- K. Sušelj and A. Sood: Improving Mellor-Yamada-Janjić parameterization for lower Marine Planetary Boundary Layer. *Boundary Layer Meteorology* (under review, pending revisions)
- K. Sušelj, A. Sood and D. Heinemann: North Sea near-surface wind climate and its relation to the large scale circulation patterns. *Theoretical and Applied Climatology* (under review, pending revisions)
- K. Sušelj, D. Heinemann, A. Sood 2009: North Sea Near-Surface Wind in the Past and Future Climates. *Proceedings of European Wind Energy Conference 2009, Marseille*
- K. Sušelj, M. Tsimplis and K. Bergant, 2008: Is the Mediterranean Sea Level Variability Predictable? *Physics and Chemistry of the Earth, Vol. 33*, pp. 225-238
- M. Kobold and K. Sušelj, 2005: Precipitation Forecasts and Their Uncertainties as Input into Hydrological models. *Hydrology and Earth System Science, Vol. 9*, pp. 322-332

Erklärung

Ich erkläre hiermit, dass ich die vorliegende Arbeit selbstständig verfasst habe und nur die angegebenen Hilfsmittel benutzt habe.

Kay Sušelj